IN SITU TEM STUDY ON THE MECHANICAL BEHAVIOR OF NANOWIRES

by

Junhang Luo

B.S. in Materials Science and Engineering, Zhejiang University, 2003

M.S. in Materials Physics and Chemistry, Zhejiang University, 2005

Submitted to the Graduate Faculty of

the Swanson School of Engineering in partial fulfillment

of the requirements for the degree of

Doctor of Philosophy

University of Pittsburgh

2010

UNIVERSITY OF PITTSBURGH

SWANSON SCHOOL OF ENGINEERING

This dissertation was presented

by

Junhang Luo

It was defended on

December 14, 2009

and approved by

William S. Slaughter, Associate Professor, Department of Mechanical Engineering and Materials Science

Sung Kwon Cho, Assistant Professor, Department of Mechanical Engineering and Materials Science

M. Ravi Shankar, Assistant Professor, Department of Industrial Engineering

Dissertation Director: Scott X. Mao, Professor, Department of Mechanical Engineering and Materials Science

ERRATUM

The author would like to make known that there was an earlier version of this dissertation that was released, and that this version supersedes this previous version. Only the version containing this erratum page should be considered the official, final copy of the dissertation.

IN SITU TEM STUDY ON THE MECHANICAL BEHAVIOR OF NANOWIRES

Junhang Luo, PhD

University of Pittsburgh, 2010

One-dimensional nanomaterials have qualitatively different mechanical behavior comparing with their bulk form owing to their small length scale and huge surface area[1]. To predict the mechanical properties and deformation behaviors of material in nanometer length scale and disclose the deformation mechanisms of them, plenty of computational simulations have been conducted. However, due to the sample mounting difficulty and their quite small volume, it is very tough to perform high-quality mechanical testing and validate the predictions from computational simulations.

Using the unique Nanofactory probing systems, in-situ mechanical tests combined with observations by transmission electron microscopy (TEM) with atomic resolution have been performed successfully on one-dimensional nanomaterials such as silver (Ag) nanowries, silica (SiO_2) nanowires, nanoscale $Al_{90}Fe_5Ce_5$ metallic glass and sodium chloride (NaCl) nanowires. 19.3 % strain was achieved in the bicystalline Ag nanowires. Stacking faults formed on the (111) plane and interestingly, the stacking fault (local hexagonal close-packed (hcp) structure) was not induced by partial dislocations movement, but by the Frank loops formation and expansion.

SiO_2 glass at room temperature is usually brittle due to fracture instability. However, showered by electron beam, silica nanowires with big diameters (>100 nm) can flow superplastically more than 670%. But once beam is blanked more than 2 minutes, the mechanical response can recover back to brittle failure if silica nanowire's diameter is large than 20 nm. However, unrecovered beam damage will trigger the brittle to ductile transition if silica nanowire's diameter is less than 20 nm.

$Al_{90}Fe_5Ce_5$ metallic glass with size less than 20 nm can be super plastic deformed with elongation ~200%. Necking occurred without shear bands in the nanoscale sample with an area reduction nearly 100%. Surprisingly, it is first time to see atomic chain formation in metallic glasses. Fast diffusion of surface atom and no chance to form shear band is thought to attributed to such extraordinary ductility.

The mechanical test on common salt shows very interesting results. NaCl nanowires can be formed by touching sharp probe with NaCl surface in the transmission electron microscope and deform superplastically. The nanowires can be stretched to 280% and be very flexible under compression (can be bent over 90°) under the electron beam irradiation. During the elongation process, there were no dislocations observed due to the fast diffusion.

TABLE OF CONTENTS

LIST OF TABLES

LIST OF FIGURES

ACKNOWLEDGMENTS

I would first give my sincerely thanks to my advisor, Dr. Scott X. Mao, for his consistent support, guidance, encouragement, and patience during my Ph.D. study; to Dr. Jianyu Huang, my mentor in CINT, for his kindy help and teaching on the in-situ TEM works and caring for my living.

I also wish to thank my committee members, Dr. William S. Slaughter, Dr. Sung Kwon Cho and Dr. M. Ravi Shankar for their reviewing, insightful comments and time on evaluating my research. Thanks Dr. Mingjian Hua and He Zheng for their assistance and helpful discussions on my research. I am also thankful to Dr. Goldman for checking and revising the language fluency of the dissertation.

It will not become possible for all the work if without the support from Center of Integrated Nanotechnology (CINT), Sandia National Laboratories. I am grateful to the staff members there, Mike Moran, Doug Peter, David Lang, Heather Brown and Mike Starr for their generous facilitating this research. Thanks to my friends Tom Harris, Taekyung Kim, Tania Henry, Nan Li and Yang Lu there for their kindly help.

My thanks will also go to my wonderful friends and colleagues at the School of Engineering, University of Pittsburgh, especially to Jingpeng Wang, Yu Wang, Ventzi Karaivanov, Dr. Long Li, Mr. Albert Stewart and Mrs. Glinda Harvery. Without them, my graduate studies would not have been colorful and enjoyable.

Finally, from my heart, I would be especially grateful to my dear wife, Jiazhao Cai, for her love, encouragement and unwavering support all through these years. The love of my wife and family is always the power for me to advance.

1.0 INTRODUCTION

Nanowires behavior quite different comparing with their bulk form in electrical, mechanical, magnetic, optical and catalytic properties owing to their small length scale and huge surface area[1-7]. These remarkable properties make nanowires qualified for different applications such as nano-electronics[8,9], micro/nano electro-mechanical systems (MEMS/NEMS) [10,11] and sensors[12,13]. It has made a lot of different kinds of nanowires recently because of their wide applications[14]. As we know, when the sample size drops into the nanometer range, the surface area compare to volume will become significant, and the physical properties of a material will largely effected by the surface atoms. The fundamental understanding on the materials properties especially mechanical properties will be quite critical for utilizing nanosturctures. Recently, numerous theoretical and experimental studies have been performed on different nanowires to relate their structures and mechanical properties. Novel phenomena have been observed in nanowires including lattice reorientation and phase transformation driven by surface stress [15-17], single atomic chains formation during tensile testing[18,19], shape memory and pseudoelastic behavior[20-22], and deformation induced amorphization[23,24].

Nanowires shorter than 10 nm can be formed by a sharp tip touching the material surface and then slowly retracting[25]. This method is what called mechanically controllable break-junctions techniques and normally will generate single crystalline

nanowires[25]. Three characteristics are presented in the deformation behaviors of these nanowires: Tensile yield strengths different with compression yield strength, plastic deformed with the quantized steps and ideal atomic disjointing approaching fracture[26]. However, as nanowires size turns bigger than 10 nanometers, it turns very difficult for accurately connecting such small scale structures and performing the force measurement[25]. That is why the reported testing results on the mechanical properties of the nanomaterials scatter so drastically[27-29].

Compare to experiments, atomistic simulations are much easy to carry out, so it is extensively used to investigate nanowires' deformation mechanism. Recently, a lot of groups performed atomistic simulations to study the mechanical properties and deformation mechanism of nanowires[30-33]. Using classical molecular dynamics (MD) simulations, two slip mechanisms were demonstrated by Sorensen et al. for nano materials[34,35]: one is the dislocation gliding and the other is atoms planes homogeneous shearing[34]. As the sample size smaller than a few nm, the homogeneous slip will be dominant in deformation mechanism to take over the dislocation mediated slip deformation mechanism[34]. Hyde et al.'s results revealed that the defects such as twin boundaries and surface steps have strong effect on the yield stress of Au nanowires[25]. The role of twin boundaries is that it can help materials hardening since it can act as barriers to resist the dislocation propagation[25]. The deformation process of nanowires under different conditions (shearing, elongation, twisting, and elongation combined twisting condition) with different velocities was studied by Kang et al[36]. When a Cu nanowire have first yield under pure tensile condition, it will elastic deformed following yielding again and such stages will repeat several times[36]. Under elongation combined twisting condition, it will be deformed more easily than the one just under elongation or twisting[36]. The torque and the tension force was

found to have an inversely proportional relation[36]. High strain-rates deformation induced the crystalline to amorphous phase transformation was found by Ikeda et al.[24] in Ni and NiCu nanowires[37]. Such phenomena was also discovered by Branicio and Rino in Ni nanowires [23].

Although much important knowledge was obtained from these theoretical works, however, we can only regard MD simulations as a method to motivate and qualitative direct the real experiment, but not use it as a way to confirm whether a mechanism is really exist or not[38]. The results from the MD simulations still need the experiments to validate the accuracy. As revealed by many indirect experiments, strong size effect is shown on the nanowires' mechanical properties. However, owe to the challenge of mounting the nanowires on testing device, there still absent direct experiments showing the evolution of structure as well the mechanical response of nanowires, and thus delay the practical industrical application of nanowries. It has been proven that In-situ TEM is a prevailing tool to disclose the fundamental physical mechanism because of its advantages like real time observation, dynamics and atomic resolution. And it was used on material research for long time. However, in-situ TEM experiments on discovering the deformation behavior and mechanical properties of nanowires are still lacking until now. There is still a missing gap between the experimental data of real mechanical test and the predications from simulations. There remain two questions not answered yet: 1) what really happened during the nanowires deformation process2) why caused such phenomena?

Recently, by using a unique Nanofactory TEM-STM platform, the microstructure of individual carbon nanotubes with atomic resolution simultaneously with its electrical and mechanical properties has been successful characterized by

Huang et al.[39-41]. The in-situ TEM observation revealed that kink motion is the dominant deformation mechanism for superplastic carbon nanotubes in high temperature. Such powerful Nanofactory probing systems can fascinate us to get the atomic information simultaneously with the mechanical tests on individual nanowire. Using Nanofactory TEM-STM/AFM/Indenter platforms, we performed in-situ mechanical testing on different nanowires. The goal of our research is to discover the relation between the microstructure of nanostructured materials and the corresponding mechanical property.

The following is the organization of this thesis. The theoretical background of size effect will be introduced in Chapter 2. Novel phenomena of deformed nanwoires and recent advances in mechanical testing of nanowires will also be reviewed in detail.

In Chapter 3, the experimental procedure includes materials preparation methods, experimental equipment, device calibration and sample preparation procedures.

In Chapter 4, the mechanical behavior of silver nanowires has been investigated by in-situ HRTEM mechanical experiments. Stacking faults were formed during the tensile test of silver nanowires. By careful analysis, we found these stacking faults are not induced by partial dislocations movement, but by the Frank loops formation and expansion.

The mechanical behavior of brittle materials in nanoscale is reported in Chapter 5, Chapter 6 and 7. Silica glass, metallic glass and common salt are chosen as covalent bond, metallic bond and ionic bond materials in our research. Surprisingly, tensile tests on SiO_2 glass nanowire, nanoscale $Al_{90}Fe_5Ce_5$ metallic glass and NaCl

nanowires show they are not brittle any more but plastic when the size goes to the nanometer scale.

Finally, Chapter 8 will give the summary and conclusions of this thesis.

2.0 BACKGROUND AND LITERATURE RIVIEW

2.1 SIZE SCALE EFFECTS IN PLASTICITY

In classical mechanics, it is well know there is no size effect on the plasticity of bulk materials. The deformation behavior of bulk materials is controlled by dislocation gliding, which will affect the strength, hardening mechanisms and fracture et al. However, as the materials size decreasing to micron or nanometer scale, the size scale effect turns obvious in plasticity.

2.1.1 Plasticity in Micron Scale

The wide investigations on the size effect on small volumes with micron size scale are initiated by the 1940s work on Cu whiskers by Fisher and Hollomon[42,43] and the classic experiments of Brenner[44]. Fisher and Brenner measured stress vs. strain relationship used the Cu whiskers with diameter from 1 to 25μm[43]. They found that as decreasing the whisker diameter ed will increase the yield strength dramatically, and the maximum strength of the whiskers is approaching to the theoretical strength[43]. Before deformation, these whiskers are almost perfect and only few dislocations existed owing to the quite small diameters of them[43]. Therefore it is quite difficulty for first dislocation nucleation, which may why caused the yield stress so high[42,43]. After yielding, there has much more mobile dislocations inside the crystal, so the flow stress of the whisker after first yielding will be very low because of the massive

dislocations movement, which will be much easier to be operated compared to dislocation nucleation[43]. Thus, it will have a significant drop in stress after yielding. To calculate the stress for a dislocation segment to bow out, Blanckenhagen et al. gave out the following formula[45]

$$\sigma \approx (A\mu B/2\pi)\omega^{-1}\ln(\beta\omega/b) \tag{2.1}$$

As shown in the above expression, the yield stress and sample size *l* has the inverse relation, which is consistent with experimental observations[43].

To compare with whisker deformation and get new insight on the plasticity in micron scale, Uchic and Nix et al.[46,47] recently developed a micro-compression pillar testing for measurement of yield and flow stress in small scaled materials[43]. Observed by Nix et al., the yield strength significantly increased as the specimen size decreased and the plastic flow can go on under the stress even up to several GPa for 300 nm diameter pillars. Not like whiskers, although they have relatively high amount dislocations before deformation, these nano pillars still display high strength and they showed significantly different stress–strain curve comparing with that of whiskers[48]. Multiple elastic load pick-ups occurred after a large plastic strain in these Au pillars but no big drop in flow stress like what happened in whiskers[48].

To explain the multiple elastic load pick-ups of the micro pillars, a dislocation starvation model has been proposed[49,50].. As we know, the image force, *F*, for a screw dislocation in a cylinder of infinite length is[51]

$$F = \frac{\mu b^2}{2\pi}\frac{\xi}{R^2-\xi^2} \tag{2.2}$$

where ξ represent the distance of the dislocation measured from the cylinder center 51. The imaging force is trying to let the dislocation slip out of the cylinder. Based on formula (2.2), the image force on the dislocation will become more significant as the cylinder diameter decreased. If the sample size is below some critical size, the mobile dislocations can be prematurely extinguished at the close free surfaces by the imaging force. In such condition, the dislocations multiplication through double cross slip or similar processes will not work; the dislocations will have to prematurely extinguish at the free surfaces closest to them. Eventually, the dislocation starvation state will reach. After the dislocation annihilated on the free surface, the mobile dislocation density turn to zero, so it needs the stress raised significantly again to nucleating fresh dislocation until it is over the image force of this dislocation embryo near surface[51].

The dislocation starvation evolution process scenario is presented in the MD simulation by Eshelby et al[52]. Minor et al[53] validated such dislocation starvation model by in situ compression tests on single-crystal Ni pillar[52]. In their report, mechanical loading can activate and move the dislocations existed in the crystal and cause them annihilation at the free surface the Ni pillar, which can turn the pillar sample to free of defect[52,53]. Their observation revealed the dislocations will extinguish at the nanopillars surface and cause the sate of mobile dislocation density zero, which is consistent with the dislocation starvation model proposed by the earlier experiments and simulations[52].

2.1.2 Plasticity in Nanometer Scale

2.1.2.1 Curvature effect on the yield asymmetry

Since the curvature, *k*, is equal to the reciprocal of the radius, r:

$$k = \frac{1}{r} \tag{2.3}$$

if the sample size decreases into nanometer range, the curvature will increase rapidly and thus curvature effect will become significant. For a cylinder with radius r, the formula $P = f/r$ can be used to estimate the Laplace pressure[54,55], here f is surface stress. For example, the calculated Laplace pressure can be as high as 2.8 GPa for a gold cylinder with diameter of 1 nm[54,55]. This large pressure has significant influence on the mechanical properties of small scaled samples[54]. For example, the Young's modulus was found increased in gold nanowire and yielding of the sample is not symmetry in tension with that in compression has revealed by Marszalek et al.[54,56]. Using atomic force microscopy, they performed tensile and compression tests on the 1.1 nm diameter gold wires. They found for such small nanostructure, the tensile yield stress is not close to the compressive yield stress but much larger[57]. It is also found that the wires plastic deformed with the quantized steps (0.176 nm for elongation and 0.152 nm for compression) [54]. It is related with a series of fcc to hcp transformation then transfer back fcc phase[54].

The yield asymmetry mechanism of gold nanowires has been studied by Diao et al.[57]. It is found there is obvious larger yield stress in tension than compression for very small <100> nanowires[57]. However, for <111> nanowires, there is no such yield asymmetry[57]. It is well known that the dislocation nucleation is determined that the

interior resolved shear stress (RSS)[57]. Since external forces caused the effective critical RSS, Ty, but the critical RSS, $\hat{\tau}_y$, is effected by both the surface stresses and external forces, ($\hat{\tau}_y - Ty$) can used to present the effect from the surface stresses[57], After detailed comparing $\hat{\tau}_y$ and *Ty*, they found the effect of surface stress in compressive yielding will turn much more significant with decreasing nanowire diameter[57]. Once the nanowire diameter is no more than 2.45 nm, even its own surface stress can yield the nanowire[57]. For tensile yielding, the external forces need to be above the surface stress induced RSS[57]. And as nanowires size decreasing, it turn more difficult for the external forces to overcome the RSS since the magnitude of RSS turns much larger[57]. Analyzing the uniaxial Schmidt factors, it is found that the leading partial slip under compression for <100> nanowires has larger uniaxial Schmidt factor than that under tension, so the compression yielding is much easier than tension yielding for <100>[57]. Different acting slip systems in yielding and the competition between surface stresses caused the tensile and compressive yield asymmetry for <100> nanowires[57]. For the <111> nanowires, the leading partial under tension has larger Schmidt factor than that under compression, but there is contributions from the surface stress on the compressive yielding[57]. These two factors are competing and will compensated by each other, which results the tensile yield stress of the <111> nanowire close to the compressive yield stress[57].

2.1.2.2 Surface effect on reorientation or phase transformation

Besides the curvature effect, surface effect will also become significant as sample size goes down to a few nanometers. Considering a cubic with side length of d, its volume and surface area are d^3 and $6d^2$ respectively, so the surface to volume ratio can

be estimated as 6/d. As the size of the sample goes down, the ratio can be extremely high. Consequently, the number of surface atoms will be comparable to that of volume atoms, making a considerable surface effect on material mechanical or physical behavior[58]. As illustrated in a figure of Ji's Ph.D. dissertatio[58], where a surface atom is colored by gray and a bulk atom colored by green. The coordination number for bulk atom and the surface atom was found to be 6 and 4 respectively[58]. The different coordination number can lead to the different electron charge distribution and therefore different atomic bonding condition between surface and bulk atoms[58], consequently resulting in the self-contraction on surface[15,59] and large surface stress can be generated[58].

Crystal reorientation or phase transformation can be initiated by the surface stress induced self-contraction in nanowire. For example, the surface stresses induced body-centred-tetragonal (bct) structure from fcc structure in Au nanowires has been demonstrated by Diao et al.[15,16,60]. The phase transformation caused by surface stress is dependent with several factors including the orientation of crystal at beginning, wire size, the shape of cross-sectional at beginning, temperature and boundary conditions[15,16,60]. It was found that intrinsic surface stresses can trigger such phase transformation in very small size <100> gold nanowire less than the critical size, which is ~2 nm[15,16,60]. It is predicted that the bulk bct phase is in a local energy minimum by theoretical approach, but is elastic instable by tight binding and first principle calculations[15,16,60]. This instable phase can only be stabilized in nanoscaled material because large internal stresses on it caused by high surface stress[15,16,60]. For structural reorientation case, a high surface stress made an fcc nanowire with <100> direction reorient to a <110> direction by progressive slip on adjacent planes in a

<112> system, which changes these planes stacking from ABCABC to ACBACB [21,22,60-63]. This phenomena can also be explained by similar mechanisms[60].

A detailed study on surface-stress-induced phase transformations and structural reorientation has been carried out by Haftel and Gall on different fcc metal nanowires including Au, Ag, Cu, Ni and Pt nanowires[64]. It is indicated that only when the nanowire diameter below a critical diameter, d_{crit}, which is normally around 1 nm to 2 nm, the lattice reorientation or phase transformation can automatically start[64]. Once the diameter is small enough, the compressive surface stress will relax <001> nanowires spontaneously to other orientation nanowries[64]. For Ag, Cu, Ni <001> nanowrie, it will change to <110> orientation; but for Au, Pt <001> nanowrie, it will change to a bct <001> orientation[64]. They evaluated the stability of bct, and found the bct phase of Pt only stable under shear distortions in both bulk or nanowires form[64]. However, the bct phase is unstable to shear in bulk Au, but it is stabilized in nanowire structure because of the surface contribution to the elastic constant for shear[64]. For Ag, the fcc to bct phase transformation is not likely to happen due to the weak surface effect[64]. For Ni and Cu, the shear instability is too large to be conquered in the bulk although there are large surface and edge effects, so it is not possible for these nanowires transform from fcc to bct[64]. It is found the reorientation from <001> to <110> only exist in Ni, Ag and Cu[64].

2.1.2.3 Surface effect on Young's modulus

The surface atoms is not in equilibrium positions as the bulk atoms and they have very different interatomic distance from that in interior, Thus it results quite different surfaces elastic properties from those of an idealized bulk material[65]. The ratio

between surface area and volume will increase dramatically with the sample size shrinking, and so the surface elasticity turn considerable[58]. For example, the Young's modulus with size of silicon relationship can shown as the following fomula[66]

$$E = E(core) + \frac{1}{A}\sum S^{(i)}\omega_i \tag{2.4}$$

where ω_i represents the sample size. From the formula, the Young's modulus is combined with two components: one is from core and another is from the contribution from the surface[66]. The predicted size depended elastic properties have been confirmed by experiments on silicon nanowires with sizes < 20 nm[67-69]. Such size-dependence has also be revealed in metallic nanowires by experimental observations[70,71].

2.1.3 Surface Dislocation Nucleation and Deformation Map[72]

In bulk materials, the classical deformation mechanism is that the dislocations increases through double cross slip or multiplication processes by Frank-Read sources[72,73]. As sample size decrease to nanoscale, dislocations initiated by stress have less chance to meet each other or multiplicated. These dislocations will easily escape from free surfaces making a dislocation starvation state. Another possibility is no dislocation pre-existed in the initial nanoscaled sample[54], thus in such case the plastic deformation is greatly influenced by surface dislocation nucleation[72].

The defect nucleation can be effected by surface morphology. Zhu et al[72] carry out the estimation on the 90˚ sharp corner and the middle of side surface, which are two very common nucleation sites. They calculated the activation energy for the two sites and found the dislocation nucleation is much easy from comer (0.1 eV for corner

nucleation but 0.64 eV for side surface nucleation)[72]. Using MD simulations, they clearly demonstrate that the corner is favor site for dislocation nucleation[72]. The stress for surface dislocation nucleation from a perfect nanowire can be expressed by the following equation[72]

$$\sigma = \frac{Q^*}{\hat{\Omega}} - \frac{k_B T}{\hat{\Omega}} \ln \frac{k_B T N v_0}{E \dot{\varepsilon} \hat{\Omega}} \tag{2.5}$$

It indicate from equation (2.5) that the stress for surface dislocation nucleation is somehow influenced by the sample size[74,75] since N is directly affected by the sample geometry[72]. In micropillars, it shows the yield strength and the size hold the Hall-Petch relationship with a negative slope of -0.6 to -0.7[72,76,77], The scaling behavior in pillars is thought to be caused by dislocation interactions and multiplications[77] since the amount of the mobile dislocation can be very high in such large volume[72]. As sample size decreased to some critical size in nanometer scale, the dislocation starvation will start, and surface dislocation nucleation will dominate the plastic yielding[72]. The critical size is expected around tens of nanometers. Surface dislocation nucleation transited from dynamic cooperative dislocation activities has been shown in some recent experiments on quite small nanostructures[50,72,76].

2.2 NOVEL PHENOMENA OF DEFORMED NANOWIRES REVEALED BY ATOMISTIC SIMULATIONS

Due to the quick progress of nanotechnology and wide applications on nanowries, it is quite critical to deeply recognize their deformation behaviors and mechanical properties[78]. Abundant MD simulations had been performed on metallic nanowires.

Recently, it is demonstrated that a <110> nanowires can have pseudoelastic behavior or even shape memory[20-22,61,62,79-82]. Such nanoscale phenomenon indicates that metal nanowires can be used as materials can be self healed and may be uesed on nano devices in the future[58]. To better employ these shape memory nanowires for future application, it needs comprehensive understanding the mechanisms which controlled their deformation and mechanical properties. Based on this purpose, numerous MD studies were performed on the shape memory nanowires[62]. Liang et al.[20,22,62] showed shape memory effects (SME) can exist in some fcc metallic nanowire with size below 5nm including Au Cu ,Ni because they have high twinnablility[62]. However, since the twinnablility of Al is low, the SME is not possible to exist in this metallic nanowire[62].

Mehrez et al.[83] did MD simulations on copper nanowires and found that after first yielding, the nanowires will elastic deform again until next yielding and such stages repeat several times under uniaxial elongation[83]. Approaching fracture, the migration of atoms will form atomic chain at the neck area[83]. The atoms in the necking area tend to rearrange in closed-packed structures due to the extreme strain[83]. The atomic chains have also been demonstrated can be formed in nickel[84-86] and gold[30,87-89] by MD simulations. A detailed study on how possible the single-atomic chains can be formed was conducted by Bahn and Jacobsen in metals including Au, Ag, Cu, Ni, Pd and Pt[90]. Their results show that the atomic chain is easiest formed in Au and Pt. It is indicated by density functional theory calculations that the metals should have strong atom bonding in low coordinated systems to form atomic chains[90].

Another interesting phenomenon revealed by MD is that high strain rates deformation induced amorphousation in Ni and NiCu nanowires [23,24]. At low strain rate like $\dot{\varepsilon} = 0.5\%\ ps^{-1}$, Ikeda et al. and Branicio et al. found coherent shear bands

for example twins were produced in the crystal and finally necking before failure[23,24]. However at high strain rate like $\dot{\varepsilon} = 5\%\ ps^{-1}$, coherent shear bands or twins will not be formed but crystalline to amorphous transformation appeared in the specimens. Similar deformation behaviors were observed in tensile copper nanowires. Liang and Zhou did the investigation on the size effect and strain rate effect on nanowires deformation[91]. They found that specimen size changing will trigger a transition of deformation mechanism. For nanowires with large size, the plastic deformation was dominated by multiple cross-slips. But as the nanowire size decreased to below nm, the dominating mechanism will change to slipping along alternating (111) planes[91]. It also reported there is strong effect from strain rate on the transition of the deformation mechanism. Three different deformation mechanisms will show up with different strain rates: If strain rate is low, deformation is dominated by the lots of slipping along some favorable slip planes which are well-defined. As the strain rate goes to mediate range, deformation will be dominated by cross-slip. And if strain rate is extreme high, deformation will be dominated by amorphization[91].

2.3 MECHANICAL TESTING OF NANOWIRES

MD simulations has revealed many new phenomena on nanowires deformation behavior such as surface stress-induced lattice reorientation and phase transformation[15-17], formation of single atomic chains in the necking area[18,19], pseudoelastic behavior and shape memory effect[20-22], and deformation induced amorphization[23,24]. Nanowires have received widespread interest because of their unique behaviors and outstanding physical properties including electrical, mechanical, thermal and optical. These outstanding properties ensured the nanowire wildly

applications in nanotechnology[10,11, 92,93]. Due to the high surface stresses, strong size effects is shown on the deformation behavior and mechanism of nanowire[32,91,94,95], which means that we can not only apply the bulk mechanical properties to that of nanostructures[96]. So for better employing the nanowires on practical application, it is very necessary to quantify the mechanical properties directly from these small volumes[96].

However, because of their small size and difficult in precisely operating them, it is really a challenge to mechanical test nanowires. Testing devices need to be miniaturized and have the capability to apply force for quantitatively measuring the mechanical properties of nanowires. It also needs subnanometer resolution to detect the local deformation. AFM，SEM and TEM have been extensively used for characterizing the nanostructures and deformations in nanoscale because they have nanometer resolution. So far, there are two advanced experimental techniques in mechanical characterization: one is AFM based tests, and another is in-situ electron microscopy based tests[97].

2.3.1 Bending Test

Three-point bending test and lateral force microscopy (LFM) are two main types of bending tests developed by AFM testing techniques. Individual nanowires are normally suspended on a hole or trench in the three-point bending test, The nanowre can be clamped by several methods[98] such as directly using the self-adhesion force of the wire on the substrate[99], depositing some metal to wielding the nanowire and substrate by electron beam (EBID process)[7,100] or using epoxy glue[101]. In three-point bending test on single nanowire[98], the suspended nanowire will be deformed by an

AFM cantilever tip in the middle. Based on the three-point beam bending theory[102], the elastic constant E can be evaluated using the following equation[96]

$$E = \frac{FL^3}{192dI} \tag{2.6}$$

Nanoscale three-point bending tests has been successfully carried out by Ni et al. on single crystalline GaN nanowires and amorphous SiO_2 nanowires[100,103]. The calculated elastic modulus for single crystalline GaN nanowires is 43.9 ± 2.2 GPa, and 76.6±7.2 GPa for amorphous SiO2 nanowires[100,103]. It was found the size don't have significant influence on the elastic modulus for both nanowires. And these two kinds of nanowires usually brittle failure and didn't exhibit the obvious plastic deformation in bending. The elastic modulus of the Ag nanowires were also successfully investigated[104] by nanoscale three-point bending tests. The calculated elastic modules for Ag nanowires with diameter ranging from 45.6 to 60.4 nm are ranged from 15.4 to 24.6 GPa[104].

Wong et al.[105] was first researchers to use the LFM method to get the elastic modulus of nanostruces such as multiwalled carbon nanotubes and SiC nanorods[96]. Used such method, Song et al.[106] did the measurement on ZnO nanowires which vertically aligned on substrate by AFM scanning in contact mode. The normal force will have to be kept constant between sample surface and the AFM tip in the contact mode[96], thus the tip will automatically adjust its height to keep the local contacting force constant during scaning[106]. Recording the tip's height changing, the surface morphology can be determined[106]. The image of position topography and the lateral

force will give the direct information of the bending distance and the bending force [106]. The Young's modulus can be determined using the following formula[96]:

$$E = \frac{KL^3}{3I} \tag{2.7}$$

The obtained Young's modulus are 29 $\pm$ 8 GPa for 45 nm ZnO nanowires[106]. The advantages of this technique is that it will not devastating or maneuvering the sample, and it can carry out systematically scanning on all the nanowires in the scanning area[106].

Using similar method, Wu et al. and Heidelberg et al.[7,27] did fully measurement on the mechanical properties of nanowires including yield strength, elastic modulus, ductility and fracture behavior[96]. The nanowires are suspended over a trench and mechanically clamped on a SiO_2 substrate[7]. They did lateral force AFM on two metallic nanowires: fivefold twinned Ag nanowires[107] and Au nanowires[7], and found the sample size doesn't have strong influence on the Young's modulus for both nanowires[7]. For Ag nanowires, the average modulus is 102 ± 23 GPa, much higher than reported bulk silver value 83 GPa[7]. However, the average modulus of Au nanowires is 70 ± 11 GPa, which is no much different with reported values 78 GPa for bulk gold[7]. It is verified that the yield strength for Au nanowires is strongly dependent with the nanowire diameter. The yield strength of Au nanowire is increased as size decreasing and the largest strengths measured can reach almost 100 times of bulk Au yield strength[7]. The dislocation is still operatied in the Au nanowires with such small diameters of 40 nm since the stress-strain curve of Au nanowire still has the strain-hardening characteristics [7]. In contrast, the fivefold twinned Ag nanowires have no considerable plasticity but super elastic deformed until brittle fracture[107]. However,

the Ag nanowires can turn more ductile after thermal annealing, which eliminates some twinned boundaries[107]. This implies that tailoring the nanowires microstructure can control their mechanical properties.

2.3.2 Tensile Test

In tensile tests, a single nanowire will be clamped over the gap of a straining stage[96]. The nanowire will be pulled continuously until failure as the two ends of the stage depart away[96]. During the testing, the applied force and the elongation of the nanowire can be recorded. And then it can be used to determin the nanowire's mechanical properties including elastic modulus, ductility and strength[96].

Ding et al[108] successfully using EBID method clamped an individual boron (B) nanowire between two AFM tips and stretched it in a SEM. The applied tensile force was increased until the nanowire broken[108]. Analyzing the SEM images, the deflection of the cantilevers as well the elongation of the nanowire can be achieved[108]. Based on solid mechanics, the tensile force and tensile strain can be calculated[108]. The Young's modulus as well fracture strength can be acquired by analyzing the stress-strain curve. They tested nine B nanowires and got the averaging Young's modulus ~320 GPa and the fracture strength 2 to 8 GPa, which is no much different with the values got from resonance test results[108].

An in-situ method in TEM was introduced by Han et al. recently on bending test or tensile test of nanowires in TEM[69,109-111]. In this method, first they will use special way to induce designed cracks of the celloidin/ carbon film on a Cu grid[69]. Then the nanowires were dispensed at random on the TEM grid and infrequently some will suspended on the designed cracks of the film[69]. After good nanowire found trenched

on these cracks, the electron beam will be controlled to irradiate the crack and cause the film shrinking and thus stretching the nanowires axially[69]. This method can be applied to any kinds of TEM and no special TEM attachments are needed[109]. The other advantage is that it can tilt the nanowire to quite large degree, which can ensure the individual nanowires to ideal orientation for observation during the testing[109]. Using such method, single-crystalline Si nanowires was stretched at room-temperature and large strain plasticity was discoverd[69]. The plasticity of Si nanowire is much higher than bulk Si plasticity[69]. A lot of dislocations emerged in the Si nanowire at the beginning, and then they disordered the crystalline structures and induced the amorphous structure formation in the long necking area before the nanowire broken[69]. Further, a extensor with two thermal bimetallic strips designed by Han's group and they used this homemade tensile stage axial strained individual silicon carbide (SiC) nanowires in SEM[112]. The thermal bimetallic strips was made of one material with large thermal expansion coefficient and one with low thermal expansion coefficient, both of which were mounted on a heating stage with the opposite position[112]. By heating up the stage, the bimetallic strips will be bent and the nanowire suspended between them will be stretched[112]. Using this homemade tensile device, they discovered low temperature super plasticity with elongation more than 200% in the beta-SiC [111] nanowires of single crystal structure[112]. In the SiC nanowires, there has 3C segments microstructure and it was suggested the observed superplasticity are related to such special structure where the dislocation nucleated, propagated and finally induced the amorphization of the local area[112]. In contrast, the segments with the highly defected structural only elastic deformed because of no slip systems working in such segments for dislocation movement[112].

To do the tensile testing on nanowires with high resolution stress and strain, Zhu and Espinosa et al developed a nanomechanical test system[97,109,113,114]. The in-situ testing device includes a force sensor with nano-Newton force measurement capability. It also equipped an actuator activated by thermal, which can measure the displacement[109]. Using this special in-situ straining device in SEM or TEM, it can perform the real time observation on the deformation and failure process with simultaneously force measurement[115]. The tensile testing on ZnO nanowires and Pd nanowires has been successfully conducted using this device[113,114]. The Young's modulus as well the fracture strength can be achieved by analyzing the achieved stress-strain curves[109]. Zhu and Espinosa et al obtained the Young's modulus as 30 GPa for a ZnO nanowire and 99.4±6.6 GPa for a Pd nanowire[109]. For the fracture strength of ZnO nanowire, it was measured as 3.5 GPa[109]. For the fracture strength of the Pd nanowire it was measured as 1.5 GPa[109]. These results are comparable to the values reported by other groups using different methods[97]. For both nanowire, they didn't find any plasticity but pure elasticity and the strength is much higher than that of bulk forms[97]. Their results indicate the strength of nanowire can be increased dramatically and approach to the theoretical strength as the size decreased[97].

2.3.3 Resonance Test

Poncharal et al.[116] were first ones to use the resonance method to do the measurement on the Young's modulus of carbon nanotubes in TEM. Some other researchers also applied similar method under an optical microscope[117] or in a scanning electron microscope (SEM)[108,109,118-120]. In this method, an electron-static excitation source is accurately moved to very close to the individual nanowire by a stage driven by pizeo[108,109]. Then between the tip and the nanowire, it will apply an AC voltage under

a DC bias or no bias to test the nanostructure[109]. Mechanical resonance will be stimulated when the frequency of the AC voltage tuned until it is equivalent to the nanowire's natural resonance frequency[109]. The mechanical resonance of a cantilevered nanowire can be excited by applying periodic force induced by mechanical device or an electrical field[109]. In mechanical excitation case, mechanical vibration of piezoelectric bender was induced by an applied AC voltage and drove the mechanical resonance of the attached nanowire[109]. In electrical excitation case, an AC voltage will be applied between the TEM grid and the AFM cantilever and the frequency of the AC voltage will be tuned[109].

For example, it has used this method to measure the Young's modulus of ZnO[120]. The Young's modulus was found increasing significantly to the value considerably higher than the bulk ZnO value as sample size decreasing below 120 nm,[121]. The experiments carried by Yu et al.[120] has tried to determine what condition will cause the forced resonance or parametric resonance but the result is not very clear[118]. Then Chen et al did further study and discovered that the applied force direction strongly determined whether the parametric resonance can occur[121]. An axially force will be induced if the nanowire and the countering tip is in a straight line, and the resonance will be dominated by parametric excitation[121]. However, if the applied force and the nanowire axis formed the transverse relation, the resonance will be dominated by forced excitation[121].

2.4 MOTIVATION AND OBJECTIVE

"Seeing is believing" is a worldwide accepted old saying. From the results of the MD simulations, many novel phenomena induced by deformation have been proposed in nanowires. As reviewed in the section on mechanical testing of nanowires, most experiments just measured the size effect on the mechanical properties of nanowires for example Young's modulus, but did not show the structure evolution of these nanowires. The mechanical properties of nanowire will also greatly affected by other factors such as structural configuration, defects, strain rate and temperature. What really happened inside the nanowires during deformation is still not very clear. The existing measurement techniques have some drawbacks. For example, nanoindentation[122] and force spectroscopy[56] can do force measurement with displacement but cannot capture the specimen deformation process. Optical microscopy[117] and AFM[7,100,107] can capture the deformation and failure in local area, but the resolution is not high enough for studying the mechanical properties of nanowires. The techniques developed by Han et al[69,110,111] can capture the deformation process with high resolution but no force output, and it requires frequent switching the electron beam between taking images and heating the celloidin/carbon thin film. When beam is used to heat the film, the local deformation events of nanowire have no chance to be observed. There still have a gap between the microstructure and the corresponding mechanical properties of nanowires. Absence of the direct experiments showing the structure evolution with the deformation of nanowires obstructs us to supplementary understands the deformation mechanism of these small volumes. It is very important for us to validate the MD simulation results by observation the process of the formation of initial defect, propagation, and

ultimately induced failure. To accomplish this objective, it is very essential to perform the quantitative in-situ study[115] on the deformation behavior and mechanical properties of these small volumes with high resolution observation.

It is also well know even a small surface flaw can trigger the catastrophic failure of nanowires, thus affect obtaining accurate information on the deformation mechanism of such small volumes. Therefore, good sample, i.e., one that is with a really smooth surface, free of contamination is essential for the quantitative experiments.

The present study will use state of the art experimental tools to accomplish the specific objective of in-situ observing the deformation and fracture mechanisms on really smooth surface nanowires.

3.0 EXPERIMENTAL PROCEDURES

3.1 MATERIALS AND METHODS

In this thesis, nanowires with different bonding were used to study the mechanical behavior of materials in a nanometer scale. Silver, silica, and sodium chloride as traditional metallic bond, covalent bond and ionic bond materials are chosen in our research. Al90Fe5Ce5 metallic glass is also one interest for us. The following will describe the detailed preparation method of these materials and specimens for mechanical test in TEM.

3.1.1 Silver Nanowires

The silver nanowires are supplied from Murphy's group[123]. It was synthesized in water by directly nanoparticle growth in the absence of a surfactant or polymer[123]. The average diameter of these nanowires is 35 ± 6 nm and the lengths varying from 66 nm to 12 microns[123]. These wires are satisfactory for our tensile testing since first, the small diameters enhancing the electron beam go through the nanowire and thus good lattice image can be more easily captured in HRTEM. Second, the broad length distribution will let us have more choice to pick out the suitable nanowire.

The nanowires are suspended on a 250 μm gold rod for tensile test in TEM (Figure 3.1a). To support the nanowires, first, a sharp wedge is made at one end of the

gold rod by using tweezers with cutting jaws (Figure 3.1b). Then a CircuitWork Conductive Epoxy is used to mechanical bond the silver nanowires. The CircuitWork Conductive Epoxy is a two part, silver epoxy. Part A is epoxy and part B is the hardener. We need to mix equal amounts of Part A and Part B by weight or volume. After mixing thoroughly for 2 minutes and the silver paint becomes ropy, we use a steel needle to stick a little silver paint at the tip and smear it along the wedge of the gold rod. When the paste turns almost dry, we use an aspirating needle to suck 1 ml silver nanowires solution and drop the droplet from the top of the wedge. As hoped, some silver nanowires will stick on the gold wedge by the silver paint and will be suspended for our mechanical test in TEM (Figure 3.1d).

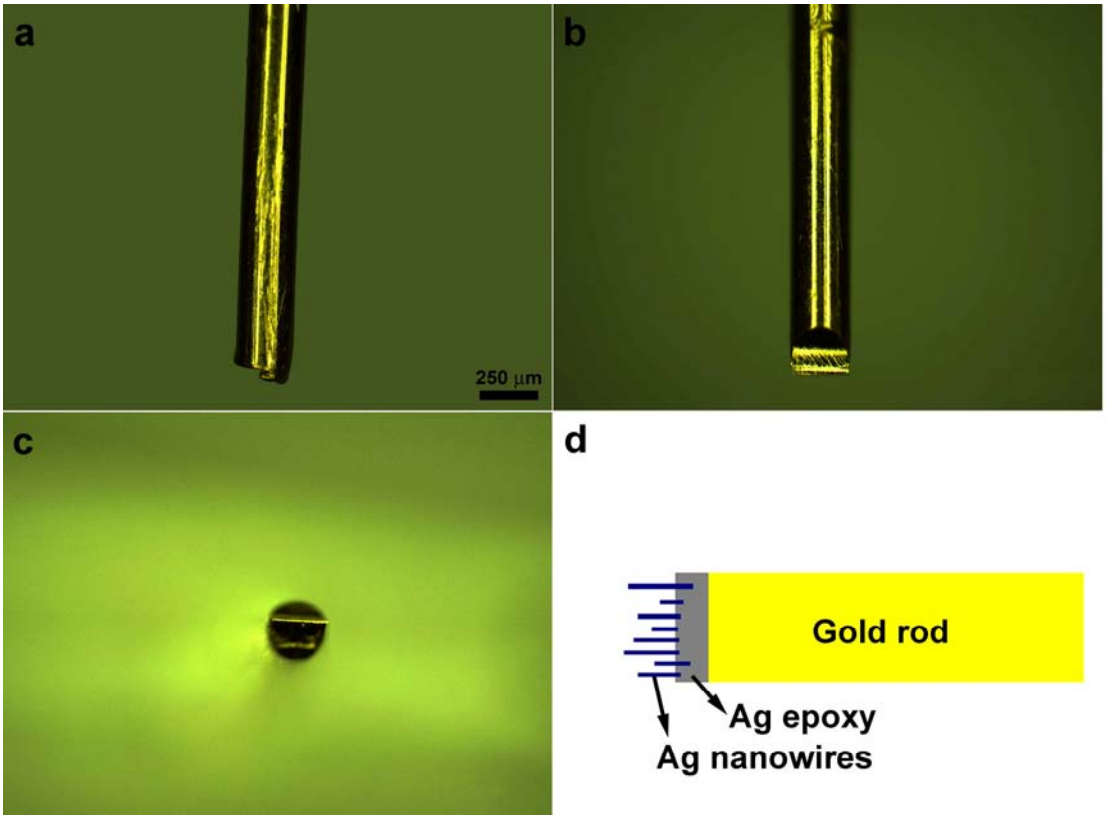

Figure 3.1: (a) A 250 μm diameter gold rod. (b) A sharp wedge made at one end of the god rod. (c) Top view of the sharp wedge. (d) Schematic of the Ag nanowires sticking on the gold rod.

3.1.2 Silica Nanowires

3.1.2.1 Drawing of micrometer wire by self-modulated taper-drawing process

The SiO_2 are supplied from Tong's group[124]. All tensile samples were prepared in a two-step process: self-modulated taper-drawing and fibre-drawing under TEM. Highly-uniform SiO_2 nanowires with diameters range from 40 to 150 nm were fabricated using a self-modulated taper-drawing process[124]. Figure 3.2 is the schematic diagram illustrating such method. The as-prepared SiO_2 nanowires have uniform diameters and lengths over a hundred millimeter. Figure 3.3a is a scanning electron microscopy (SEM) image of a SiO_2 nanowire.

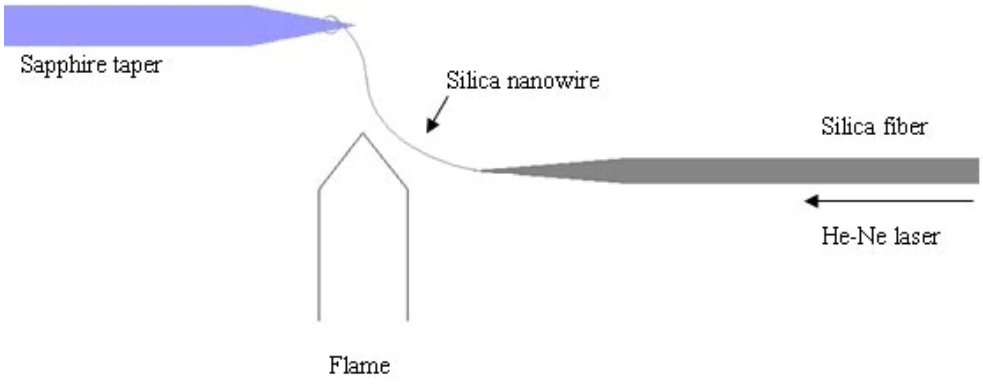

Figure 3.2: A schematic diagram illustrating a self-modulated taper-drawing process of ultrathin silica nanowires[124].

3.1.2.2 Fabrication of a dog-bone sample from a nanowire in a TEM

We prepared dog-bone tensile samples in a FEI Tecnai F30 TEM. The operation voltage is 300 KV and the resolution of the high resolution TEM (HRTEM) is about 0.2 nm. For making a dog-bone sample, we started with a nanowire with a few hundred nanometers in length. A manipulator was applied to control a STM tip with

silver paint to pick up 5 microns to 20 microns long section from a long silica nanowire under an optical microscope. Then the section was inserted into the sample adapter side of a TEM-STM holder, and another STM tip with bulk silica was fixed in the movement part of the same platform. All operations in the TEM were performed carefully in a low dose mode (5×10^{-4} A/cm^2 to 2.5×10^{-3} A/cm^2) to minimize beam exposure of the sample. The procedure is as follows. After the STM tip with bulk silica touched the suspended end of the micron long wire, we focused the e-beam (1 A/cm^2) to the contacting area to sinter them together, while the center of the nanowire was not exposed to the beam. Then the focused beam was moved away to a blank area and expanded to a very low intensity (~5×10^{-4} A/cm^2 to 2.5×10^{-3} A/cm^2) for observation. The next step was to use image shift to move the desired cutting point to the center of the fluorescence screen. Usually we cut off a 200 nm to 500 nm wire segment, which was loaded into a TEM-AFM platform and approached to the AFM tip with some silica for welding. After the short nanowire touched the silica on the AFM tip, we focused the beam to weld them together. Once the nanowire was connected between the STM tip and the AFM tip, the dog-bone samples were prepared under TEM by straining the nanowire with electron beam illumination (~2.5×10^{-3} A/cm^2). Figure 3.3b shows an as-prepared dog-bone sample with a diameter of 28.2 nm. Fig. 3.3c is the HRTEM image of the white-framed region of Figure 3.3b. And Fig. 3.3d is the HRTEM image of the broken part of the dog-bone sample. The two HRTEM images clearly show that no crystallization occurs in the sample before and after fracture. The composition was detected by the electron energy dispersive spectra (EDS). High angle annular dark field (HAADF) images were employed to figure out what the shape it is for the cross-section. Figure 3.3e is an HAADF image of the broken part of a 28.2 nm diameter dog-bone sample. We did

the EDS at position 1 and the line scanning at position 2. The EDS spectrum Figure 3.3f shows that it consists of only silicon and oxygen, and a quantitative analysis reveals that the ratio of O to Si is close to 1.96. The ratio of oxygen being a little less than the stoichiometric ratio is within the EDS error range. Figure 3.3g and Figure 3.3h are line scanning results. Judged from the EDS intensity profiles, the dog-bone sample has a circular cross section.

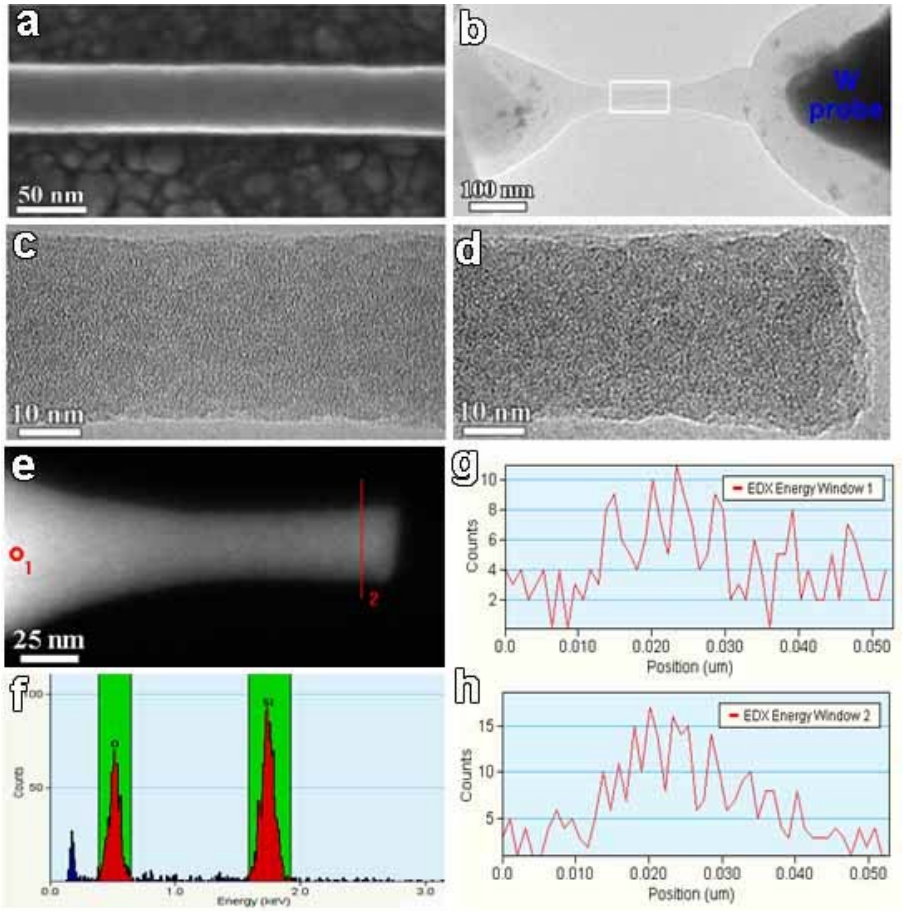

Figure 3.3: Structure and composition characterizations of the drawn dog-bone silica nano ligaments. (a) A SEM image of a 49.6 nm diameter nanowire. (b) A TEM image of a 28.2 nm diameter dog-bone sample. (c) was taken from the region of (b) marked by white frame. (d) An HRTEM image of the broken part at the AFM tip side. (e) An HAADF image of the broken part. (f) EDS analysis at position 1 of (e). (g) and (h) are the EDX intensity profiles along a line marked by a "2" in e by selecting the EDS energy window of oxygen and silicon, respectively.

3.1.3 $Al_{90}Fe_5Ce_5$ Metallic Glass

$Al_{90}Fe_5Ce_5$ ribbons were prepared by the melt-spinning a bulk on a fast spinning roller under a partial Ar atmosphere. The ribbons of $Al_{90}Fe_5Ce_5$ metallic glass used in our research are 1.5 mm in width and 25 μm in thickness. Recently, focused ion beam (FIB) technique was widely applied in preparing samples especially nanoscale samples. However, FIB is considered to influence the material structure to some extent, particularly for the sample in nanoscale[125-127]. Therefore, strictly speaking, the results based on FIB are not the real properties of materials[128,129]. To exclude any damages induced artifact by ion-beam, here we used the twin-jet polishing method to replace FIB technique for preparing TEM samples. Amorphous $Al_{90}Fe_5Ce_5$ thin foils for in situ tensile-loading experiments were polished by twin-jet method in a methanol and nitric acid (3:1) mixture solution at 243K. After electric-chemical polishing, several nanohills was found at the TEM sample edge(Fig. 3.4a,b). There was no contamination found in the prepared sample (Fig. 3.4c).

3.1.4 NaCl

NaCl crystals with size 10×10×10mm were purchased from TED PELLA, INC. Small pieces of NaCl crystals were cleved along a (100) plane of a NaCl single crystal using a razor blade and stuck to a Au rod with diameter of 250 μm by the CircuitWork Conductive Epoxy. After the epoxy dried, the specimen was put into the sample adapter side of the nanofactory TEM-STM holder for in-situ testing.

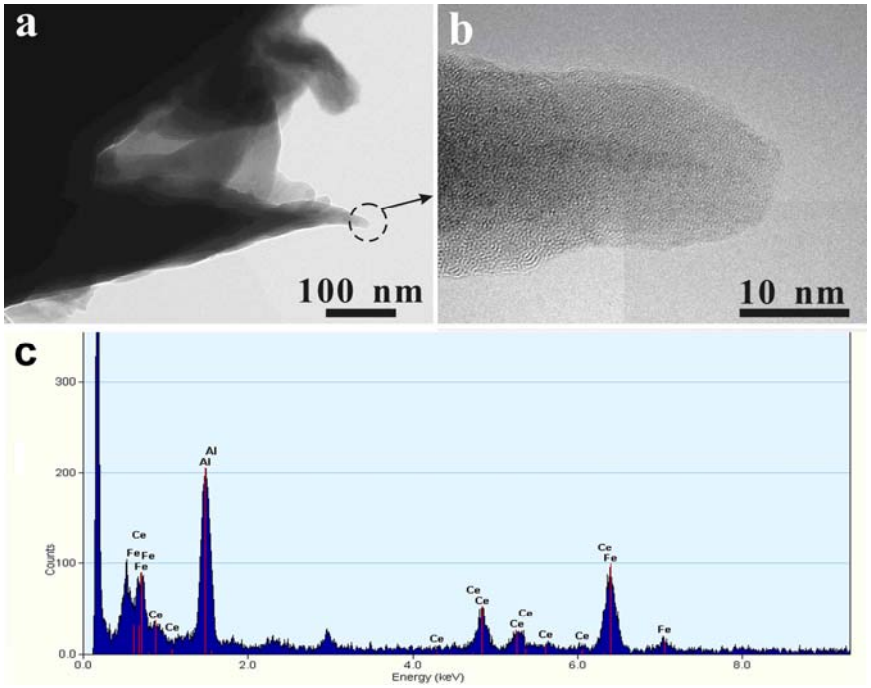

Figure 3.4: Twin-jet polished sample (a) TEM image of the nanohill at a twin-jet polished $Al_{90}Fe_5Ce_5$ sample edge. (b) $Al_{90}Fe_5Ce_5$ nanohill HRTEM image showing fully amorphous structure. (c) EDS analysis of the nanohill.

3.2 EXPERIMENTAL EQUIPMENT AND METHODS

3.2.1 Nanofactory Holders

In our research, three Nanofactory Holders were used to investigate the mechanical behavior of nanowires. They are TEM-STM platform, TEM-AFM platform, TEM-Indenter platform. Figure 3.5 is the schematic of a TEM-STM platform. There are two parts in the head of the holder. The left part is a movement controlling part and the right part is the sample holder. The movement is driven by a Piezo tube with a sapphire ball on the top. By the six metal legs, a copper octopus like hat with a STM probe can clamp on the sapphire ball. The sample is usually stuck on a 250 μm gold rod, which can be fastened in the metal pole. By controlling the Piezo tube, the STM

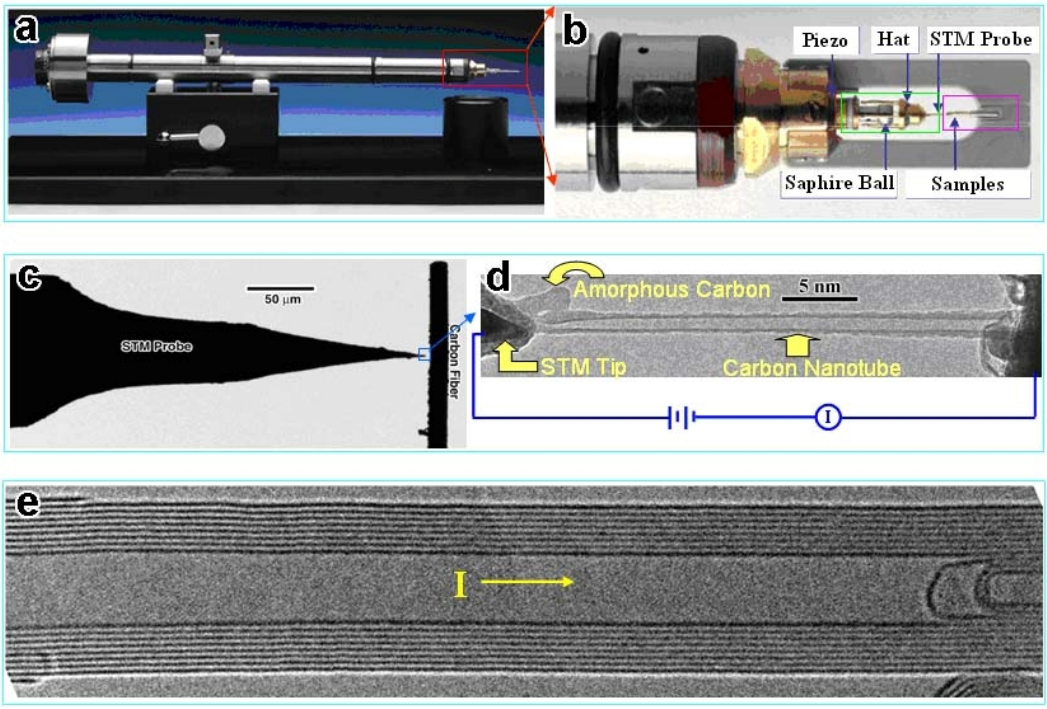

Figure 3.5: Schematic of a Nanofactory TEM-STM platform (*courtesy of Jianyu Huang*). (a) Side view of a TEM-STM holder. (b) The details of the head of the holder, which is taken from the red frame region of (a). (c) A low magnification TEM image shows a STM probe touching with a carbon nanotube on a carbon fiber. (d) HRTEM image shows how the STM tip contact with a carbon nanotube, which is taken from the blue frame region of (c). (e) Electric test of the carbon nanotube.

probe can move along the mutual-orthogonal axes X, Y and Z in TEM. Figure 3.5c shows a STM probe touching with a carbon nanotube on a carbon fiber. Once a STM probe touched the sample, we can use different method to weld the sample with the STM probe. As shown in Figure 3.5d, a carbon nanotube is welded with the STM tip by amorphous carbon. After welding, we can do mechanical test on sample by pulling, drawing and shearing. Also, we can do the electric test on samples by adding bias (Figure 3.5e).

TEM-AFM platform is a very powerful tool. It can record the force and displacement when we do the mechanical test on individual nanowires. Figure 3.6 is

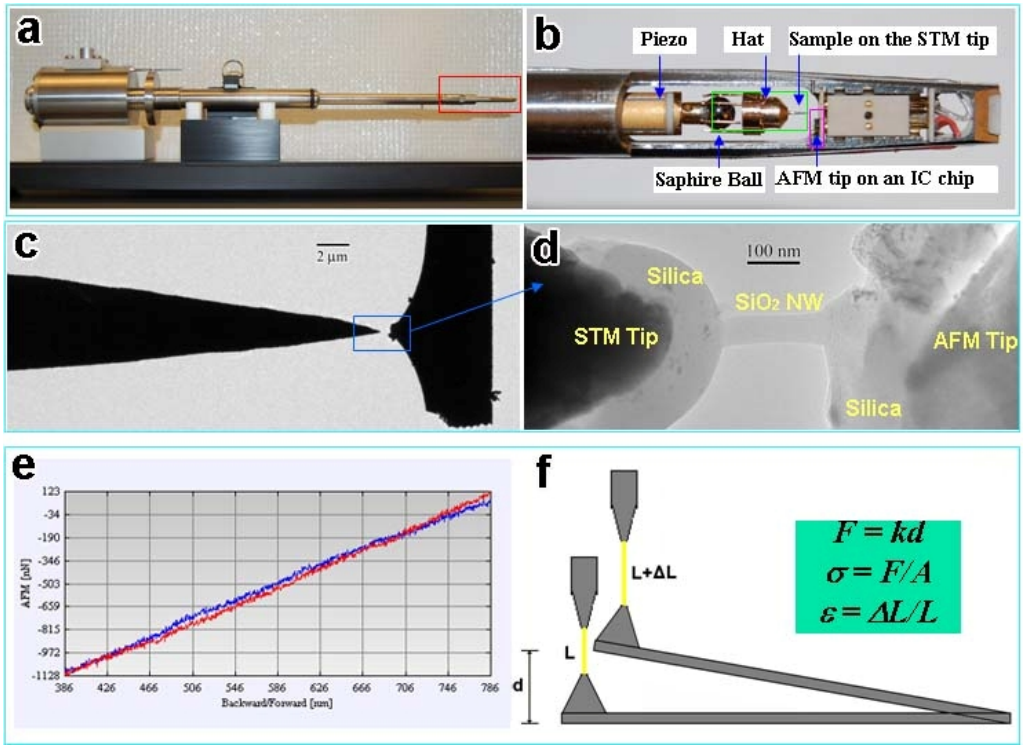

Figure 3.6: Schematic of a Nanofactory TEM-AFM platform. (a) Side view of a TEM-AFM holder. (b) The details of the head of the holder, which is taken from the red frame region of (a). (c) A low magnification TEM image shows a silica nanowire connected between a STM tip and an AFM tip. (d) High magnification TEM image shows how the silica nanowire is welded between the STM tip and the AFM tip. (e) A force-displacement curve of a SiO_2 nanowire. (f) Schematic showing the force and displacement can also be achieved from the TEM images.

the schematic of a Nanofactory TEM-AFM platform. There is a little difference with TEM-STM platform, the sample is installed in the copper hat at the left part, not right part, which is replaced by an AFM cantilever on an integrate circuit chip. Sensors mounting on cantilever and read-out of piezoresistive type are integrated on the chip[130]. By the relationship with force and voltage change, the force applied on the cantilever can be direct read out. The force output range from -3000 nN to 3000 nN. For TEM-SPM platform, we control the piezo to move the STM probe to touch the sample. But for TEM-AFM, we control the piezo to move the sample to touch the

AFM. Figure 3.6d shows a silica nanowire attached on a STM tip touching a SiC AFM tip. Once a sample touched the AFM tip, we can weld it with the AFM tip and do tensile, compression and bending test. Force can be direct output by the sensor. Figure 3.6e is a force-displacement curve of a SiO_2 nanowire showing the elastic deformation. The stress and strain can be derived from the force-displacement curve by classic solid mechanics. The force and displacement can also be achieved from the TEM images, as shown in Figure 3.6f. By recording the force and displacement with the real-time videos or TEM images, we can directly relate the structure evolution with the mechanical response of individual nanowires.

A TEM-Indenter platform is used to do the nanoindentation test and compression testing on nanopillars or nanowires. Figure 3.7 is the schematic of a Nanofactory TEM-Indenter platform. Same as the TEM-AFM platform, the sample is stuck on a 250 μm diameter gold wire and installed in the copper hat at left part and moved by controlling the piezo tube. The right part is replaced with a diamond indenter, which is integrated on a integrate circuit chip, as shown in Figure 3.7b. The force range is much larger then that of the TEM-AFM platform. The maximum force output is from -2000 μN to 2000 μN. The diamond indenters supplied by Nanofactory have a Berkovich or Cone geometry with a radius of curvature of a few microns, which is not easy to just interact with individual nanopillar or nanowire without touching other nanopillars or nanowires. To enable more accurate positioning, a flat diamond indenter with diameter of 500 nm was fabricated by focused ion beam (FIB). Figure 3.7c shows the FIBed indenter moved close to a diamond nanopillar. The max load or max depth for a compression test can be set in the software Nanofactory Instrument 3 (NF3). Once the indenter reaches the max load or max depth, it stops advancing and retracts back to the original position, and a loading-unloading testing

is completed. The distance vs. time and force vs. time curves of a nanopillar sample will automatically be recorded by NF3, as shown in Fig.3.7d and 3.7e.

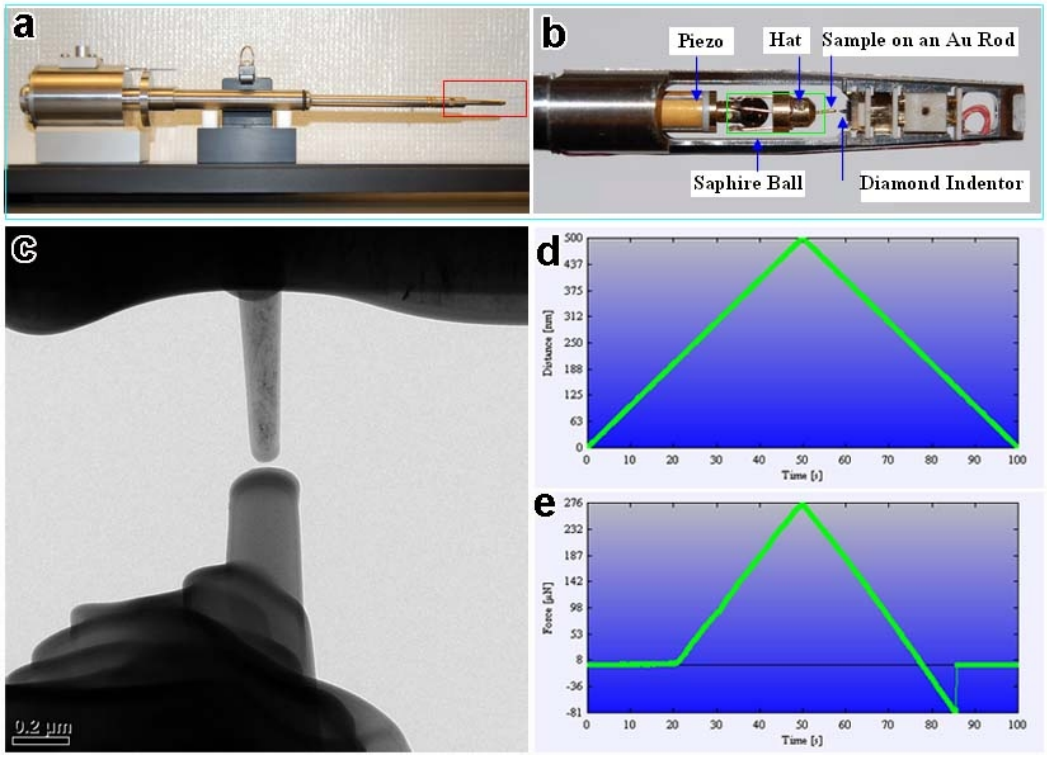

Figure 3.7: Schematic of a Nanofactory TEM-Indenter platform. (a) Side view of a TEM-Indenter holder. (b) The holder head details, which is taken from the red frame region of (a). (c) A low magnification TEM image shows a diamond indenter approaching a diamond pillar sample. (d) and (e) are the distance vs. time and force vs. time curves of a nanopillar sample.

3.2.2 Device Calibration

The NFC3 is used to control the movement of piezo and record the output such as force with displacement or current with bias. Figure 3.8 is the interface of NFC3. Figure 3.9 is the interface of the Movement Controller, which can coarse control and fine control the movement of STM probe or sample along three directions:

back-forward, up-down and left-right. The fine movement has a resolution of 0.001 nm. Before the mechanical testing, we should do the following calibration.

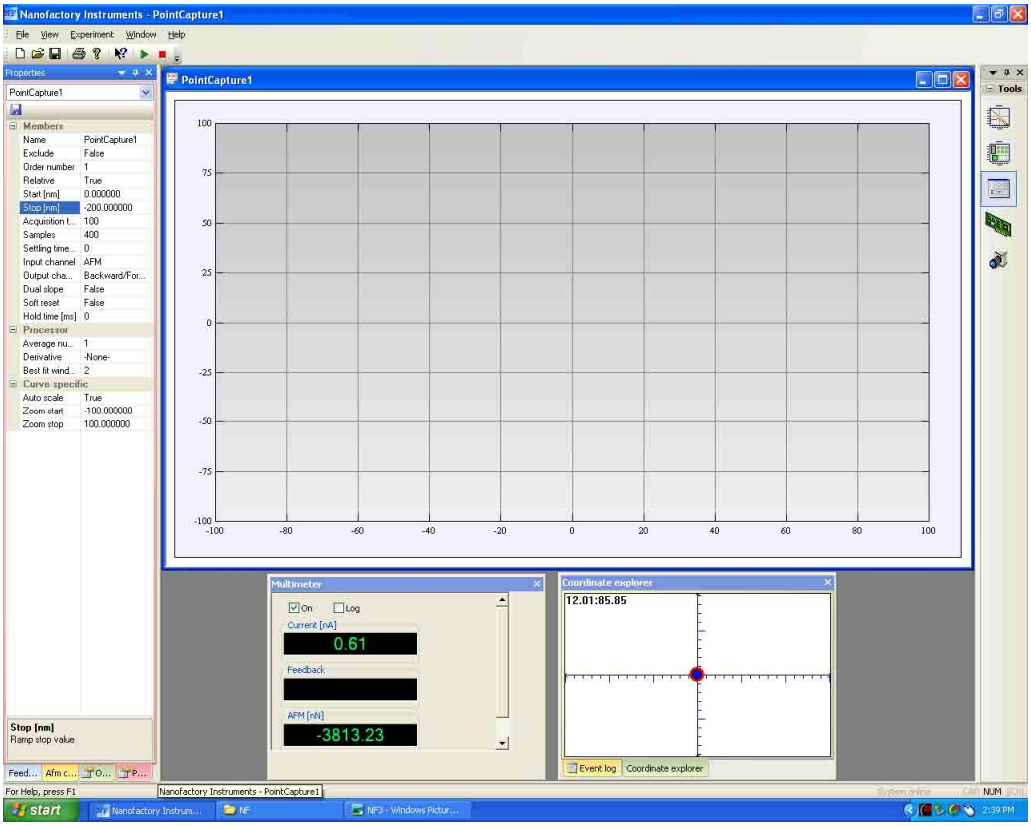

Figure 3.8: Interface of the software NFC3.

First we should do the calibration on the fine movement in the Movement Controller with the STM probe movement in TEM. Since our research will focus on tensile test to observe the mechanical behavior of nanowire, we just do calibration in the back-forward direction. The STM probe movement is controlled by the movement of the Piezo tube, which is driven by the voltage. We should set the sensitivity of back-forward, up-download and left-right, which are under the menu of electronic hardware, as shown in Fig. 3.10. The 6 nm/V in B/F sensitivity at Figure 3.10 means every 6 nm change in the fine movement in the movement controller can output 1V to

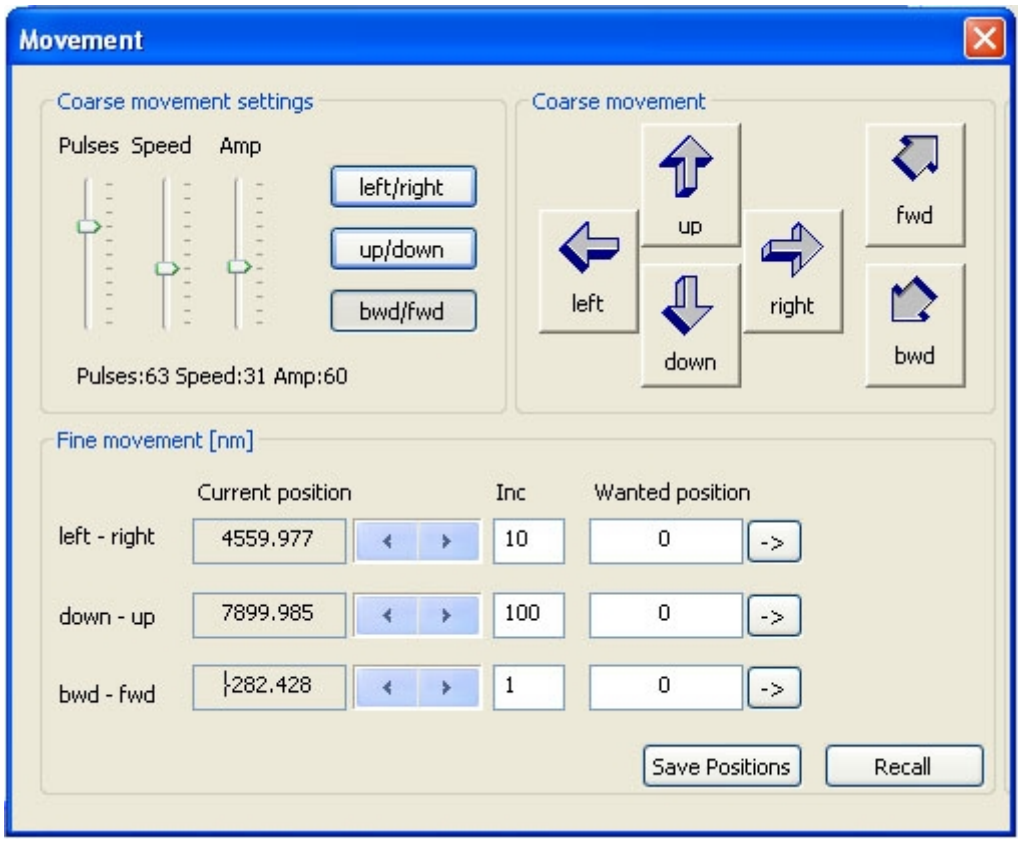

Figure 3.9: Interface of the Movement Controller.

piezo tube and drive it move in B/F direction. So if the value turns big, the actually movement of piezo for every 1 nm change in the fine movement in the movement controller will turn small. Here, we use 200 nm in fine movement to correct the value for B/F sensitivity. Figure 3.11a and Figure 3.11b are the TEM images of actually STM probe positions at the beginning and end for the 200 nm fine movement in the movement controller. By analyzing the TEM images, the actually STM probe movement is 186 nm. The B/F sensitivity should be set 5.6 calculated by

$$\frac{B/F\ Senstivity}{6} = \frac{186\ nm}{200\ nm},$$

.

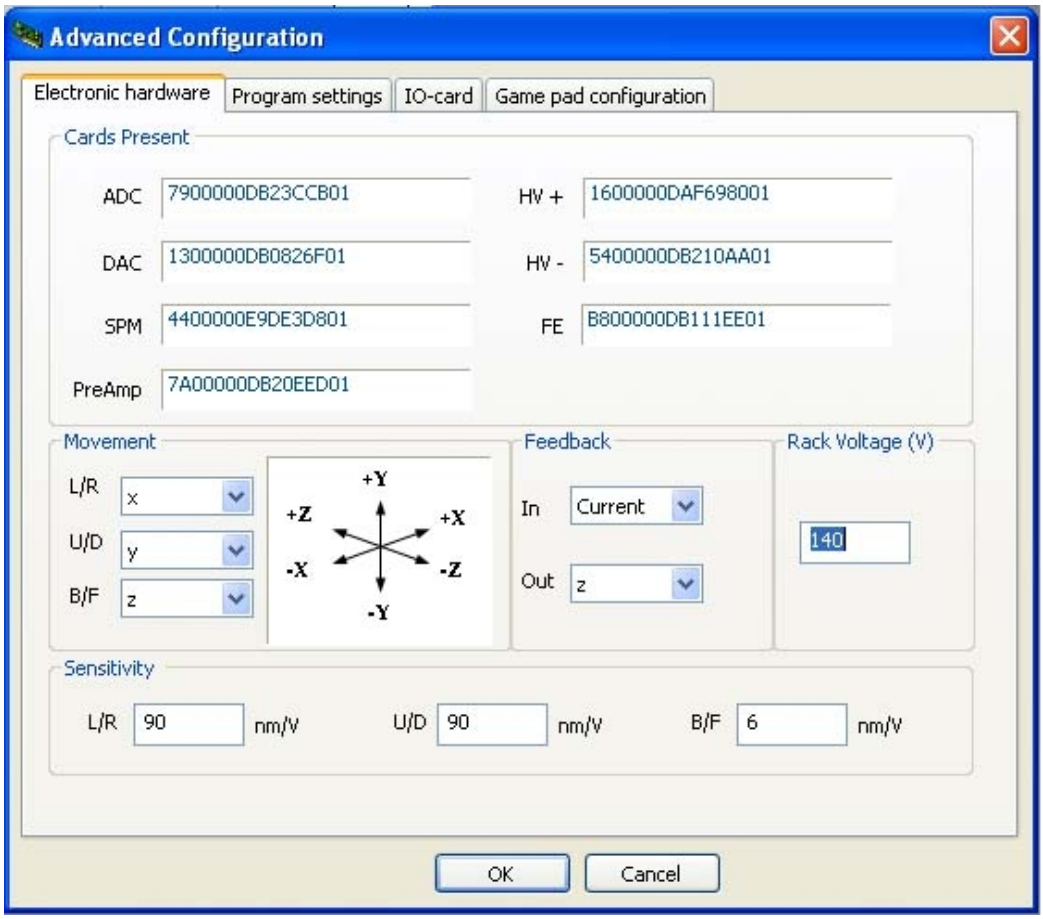

Figure 3.10: Electronic hardware setting under Advanced Configuration.

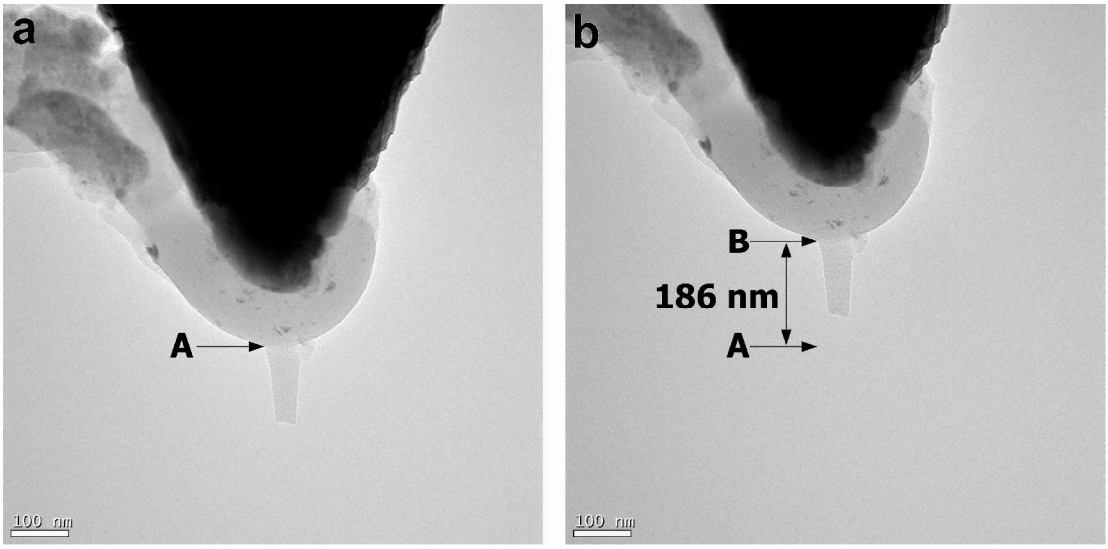

Figure 3.11: TEM images of actually STM probe positions (a) at the beginning and (b) end for the 200 nm fine movement in the movement controller.

Second, we should carry out the calibration procedure on the electrical sensitivity constant (*C*-value) of the AFM tips, which is used to sense the resistance change as the AFM tip deflected and convert the voltage change to the force applied. Typically every AFM sensor has individual force constant (*k*-value) and it has been supplied by Nanofactory™ Instrument AB Company. Table 3.1 summarized the k values of the AFM sensors used in our research.

The following method can be used for evaluation the spring constant:

$$\Delta D = FL^3/(3EI) \tag{3.1}$$

where E=160 GPa and the cross-section I is given by I= $bh^3/12$. Hook's theory gives the spring constant: $k = F/\Delta D$. Finally

$$k = Ebh^3/(4L^3) \tag{3.2}$$

where h, b, L represent the cantilever thickness, width and length. According to the equation 3.2, we can calculate out the k-value for each AFM sensor if we know the dimensions of the cantilever.

The C constant has to be defined using calibration in TEM. As we can recall the AFM calibration uses the electric constant C to convert the voltage change ΔV to the applied force F according to the formula:

$$F = k\Delta V/C \tag{3.3}$$

where k is the AFM cantilever's spring constant. To do the calibration of the electric constant C, we should first go to Program settings under Advanced

Table 3.1: Specification of the AFM sensor

BOX POS.	SENSOR	L/W/T (μm)	K VALUE
A1	W3D5#12	300/70/3.5	4.4
A3	W3D5#16	300/70/3.5	4.4
A5	W3D5#40	300/50/3.5	4.4
A7	W3D5#30	300/50/3.5	3.2
A9	W3D5#36	300/50/3.5	3.2
D1	W4D3#12	300/70/3.6	4.8
D3	W4D3#12	300/70/3.6	4.8
D5	W4D3#12	300/70/3.6	4.8
D7	W4D3#12	300/50/2.7	1.5
D9	W4D3#12	300/50/2.7	1.5

Column 1: Sensor position in box.

Column 2: Sensor specific name.

Column 3: Dimensions of the cantilever (Length/Width/Thickness).

configuration and set k=1 and C=1, as shown in Figure 3.12. Then we use a hard surface (here we use a tungsten probe since it is very rigid) to push the AFM cantilever by 200-300 nm. After loading, the NF3 will generate a force-displacement curve. Since here we set k=1 and C=1, so from formula (3.3), F=ΔV. The F-D curve we got is just the voltage-displacement curve. The one to one relation between the force and voltage gives:

$$C = \Delta F / \Delta l = \Delta V / \Delta l \quad \text{(mV/nm)} \tag{3.4}$$

where F and l represent the force and the distance. From the slope of the voltage-displacement curve, we can get the electrical constant C for the TEM-AFM platform. We carried out four calibration tests to get the C constant. Figure 3.13 is the force-displacement curves of the four calibration tests on C constant and table 3.2 summarized the C values of each test. We got $\overline{C}$=13.4 mV/nm for our device. Then we need to go to Program settings under Advanced configuration and set the real values of k=4.8 N/m (the AFM sensor we used is D1 in Table 3.1) and C=13.4 mV/nm. At this point our calibrations are completed and now the AFM sensor will measure the correct force in nN resolution.

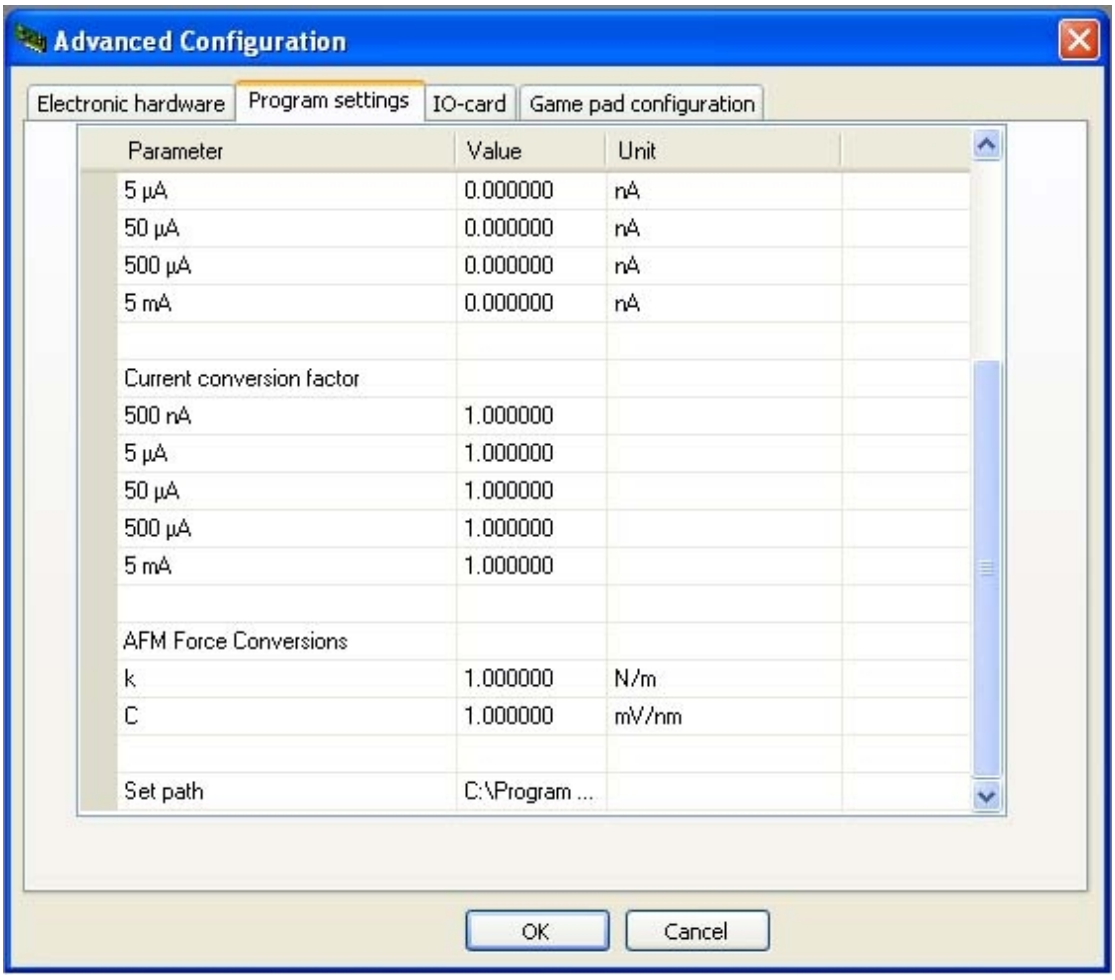

Figure 3.12: Program setting under Advanced Configuration.

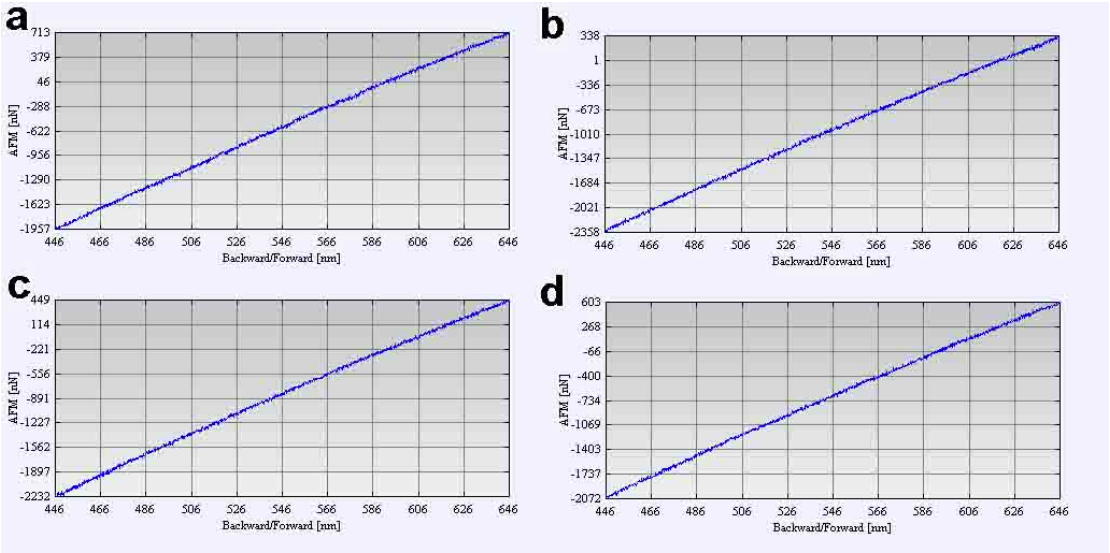

Figure 3.13: Force-displacement curves of the four calibration tests on C-value.

Table 3.2: Summary of measured electric constant C values from four calibration tests

TESTING NUMBER	DISTANCE (nm)	FORCE (nN)	C VALUE (mV/nm)
T1	200	2670	13.35
T2	200	2696	13.48
T3	200	2681	13.41
T4	200	2675	13.38

4.0 IN-SITU TEM OBSERVATION ON THE MECHANICAL BEHAVIOR OF SILVER NANOWIRES

4.1 INTRODUCTION

Nanowires are widely used as building blocks for nano devices and integrated systems, which is considered to impact various areas of nanotechnology. Due to their small length and huge surface area, nanowires show unique mechanical properties comparing with their bulk counterpart[1].

As the sample size become smaller, the ratio of free surface area comparing to the volume will turn quite large in nanowires. Generally, the free surface will act as the source for both dislocation nucleation and sink. The competition between the dislocation splitting distance, r, and the nanowire diameter, d, will control the dislocation activities. For nanowire with diameter larger than r, slip deformation will dominate the deformation because full dislocations can nucleate from the surface and propagate through the nanowire. However, if the nanowire diameter is close to or lesser than r, only partial dislocations can be nucleated and the dislocation activities will transit to partial slip from conventional full dislocation slip. The nanowire will be strain harden because the dislocation propagation restrained by stacking faults. If the nanowire size shrink further, dislocations will glide out of the nanowire before multiplication, thus "dislocation starvation" will happen[49,50]. This raises the question of how a nanowire deforms, with dislocations or without dislocations.

Here we will perform in-situ study on the mechanical behavior of silver. Deformation induced lots of stacking faults inside a small diameter silver nanowire. By analyzing the atomic-scale structural evolution, we found these staking faults are not dislocation induced but by the Frank loop formation and expansion.

4.2 EXPERIMENTAL APPROACH

Tensile-loading experiments were carried inside FEI Tencai F30 TEM with a nanofactory TEM-STM platform, which allows mechanical loading on the nanowires simultaneously with the TEM imaging to show the deformation behavior. The force loading on a nanowire is applied by the piezo tube on the movement controlling part of the holder, as shown in Figure 3.7b. Since the tensile samples are prepared by dropping 1 ml silver nanowries solution on the wedge of a 250 μm gold rod (the detailed sample preparation procedure can be found in Chapter 3.1.1), many nanowires will lie on the wedge. By checking the sample along the wedge in TEM, we can find some nanowires suspended in air, as shown in Figure 4.1a. If the suspended nanowire is too short, it will be very difficult for the STM probe to touch them. But if the nanowire is too long, it will be very difficult to take the image of the whole nanowire under high magnification and find the deformation area during tensile testing. Once we find a good nanowire, we can approach the tungsten (W) probe with a tungsten carbonyl film, slowly, to the suspending end of the nanowire (Figure 4.1b). By fine movement of the probe along the up/down direction, the height of the tungsten carbonyl film can be adjusted until it touches the nanowire (Figure 4.1c). Then we will use a high density electron beam to focus on them to make them bond (Figure 4.1d). After the silver nanowire side contacts the STM probe, it will be

loaded by the piezo manipulator at a speed 0.01 nm/s to 1 nm/s until fracture. Figure 4.1e shows the experimental setup.

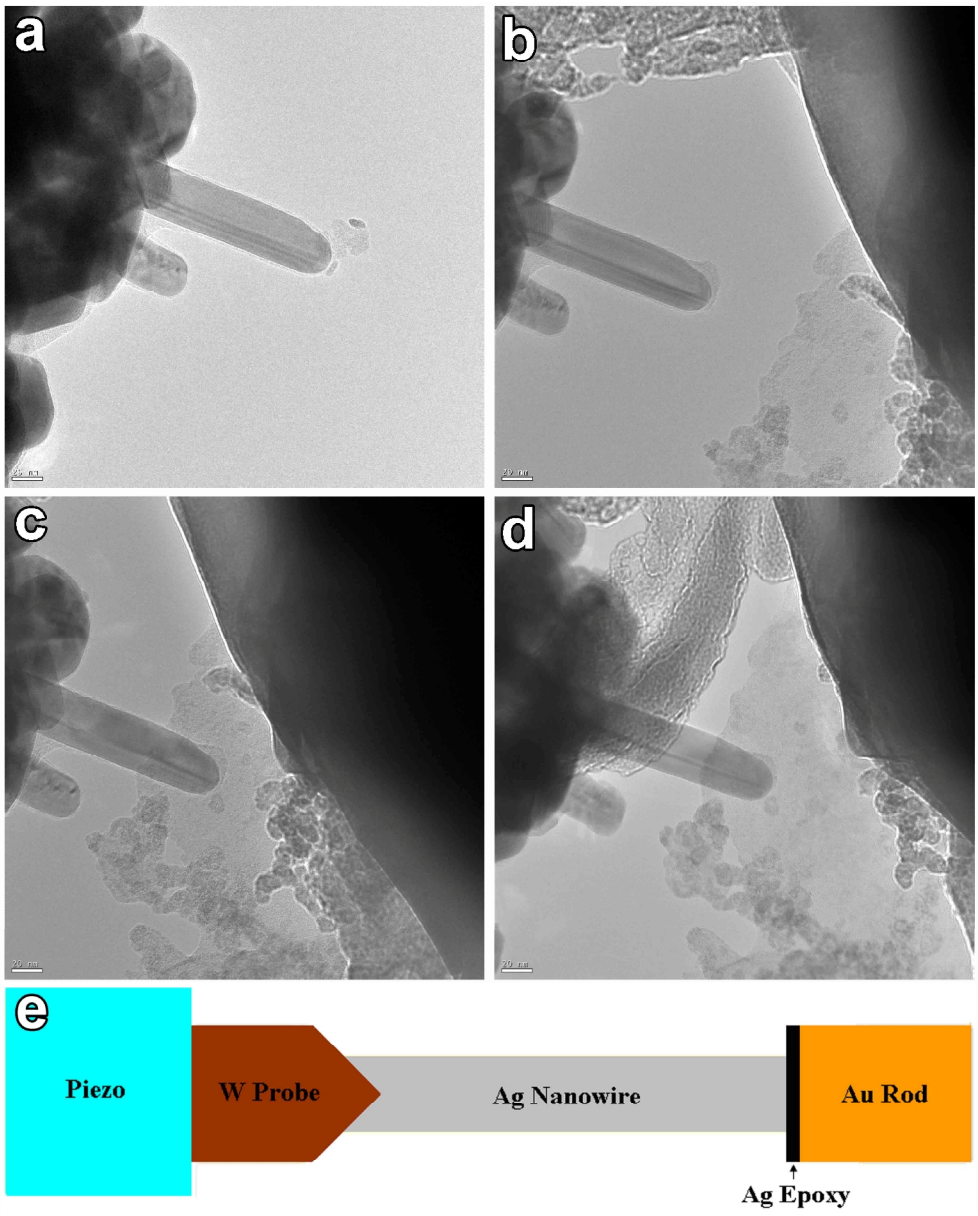

Figure 4.1: Mounted silver nanowire inside TEM. (a) A suspended silver nanowire. (b) Approaching a W probe with a tungsten carbonyl film to this suspended nanowire. (c) The nanowire contacted with the film. (d) The nanowire and the film are welded together. (e) Experimental setup. A silver nanowire is side-contacted by a tungsten STM probe, which is further attached to a piezomanipulator. Another end of the silver nanowire is glued to a gold wire by silver epoxy.

4.3 EXPERIMENTAL RESULTS

4.3.1 Microstructure of the Silver Nanowires

There are three kinds of microstructures in our silver nanowires sample: one is fcc structure, one is hcp structure and another is bycrystalline structure (Fig.4.2). From the fast Fourier transformed (FFT) images in Figure 4.2b and Figure 4.2d, a (111) twin exists in the fcc silver nanowire and a $(\bar{1}01\bar{1})$ twin exist in the hcp silver nanowire. The bycrystalline nanowire is composed of two phases: the low part is fcc and the upper part is hcp (Fig. 4.2e). The inserts in Figure 4.2e are the corresponding FFT of the black frame region and the white frame region, respectively. From the FFT patterns, it clearly shows the two different structures. Figure 4.2f is the corresponding diffraction pattern of the whole bycrystalline nanowire. It is easy to find that the pattern is combined with the two FFT patterns in the inserts in Figure 4.2e. By analyzing the FFT patterns, we found the hcp phase in our silver nanowire is not the traditional 2H structure with stacking sequence of ABABABABABAB, but a 4H structure with stacking sequence of ABCBABCBABCB. This new hcp structure in silver was first detected in mineral deposits by Russian scientist Novgorodova[131], and later, this unusual structure was also found in silver nanoparticles[132] and epitaxially grown Ag films[133]. Recently, Liu et al.[134] reported that this 4H structure can also exist in silver nanowire (4H-AgNW). These 4H-AgNW can coexist with a fcc Ag nanowire in electrochemically deposited Ag nanowires.

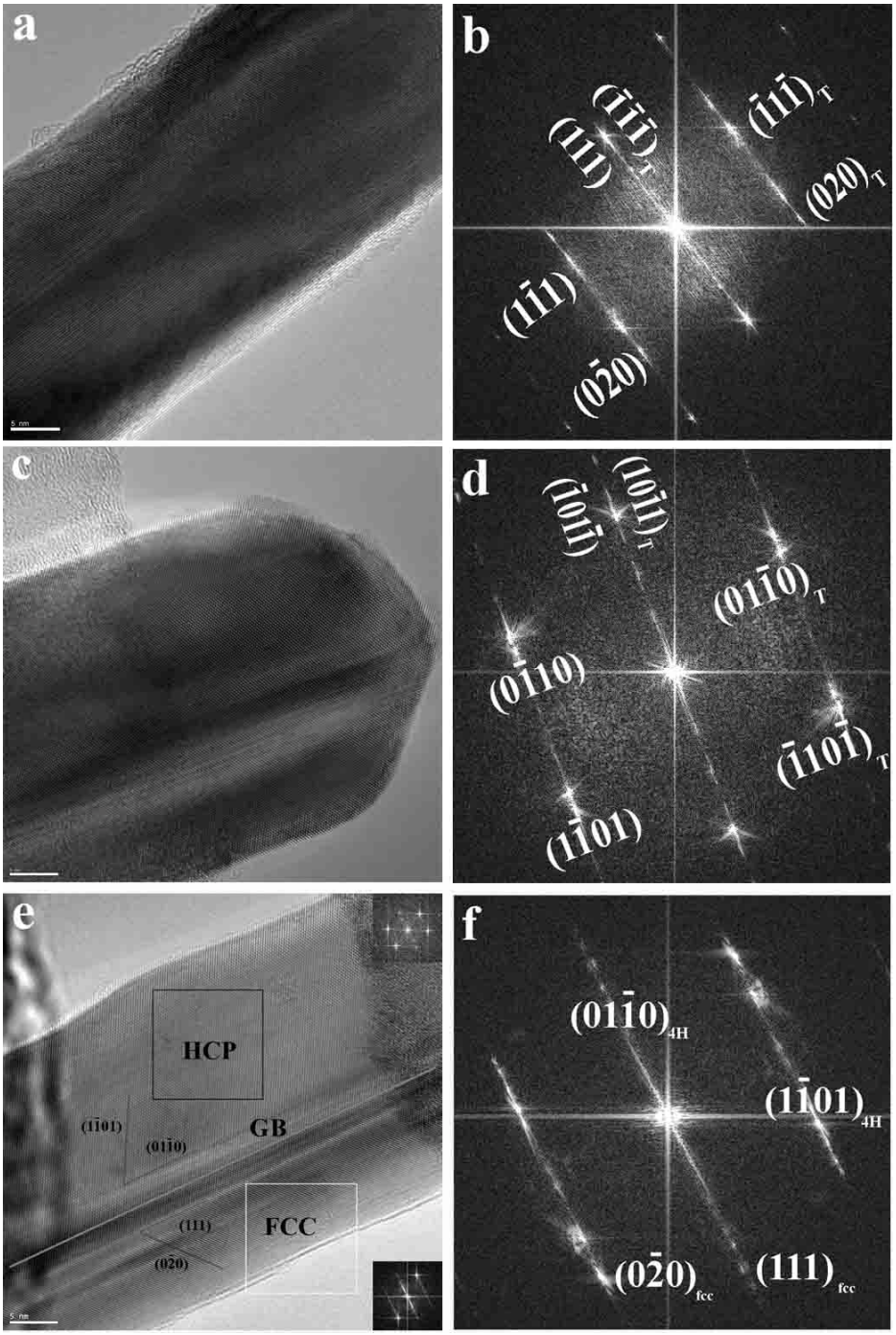

Figure 4.2: Microstructure of the silver nanowires. (a) HRTEM image of an fcc nanowire with twinning. (b) FFT of Figure a. The zone axis is $[10\bar{1}]$, twin boundary is (111) plane. (c) HRTEM image of an hcp nanowire with twinning. (d) FFT of Figure c. The zone axis is $[\bar{2}113]$, twin boundary is $(\bar{1}01\bar{1})$ plane. (e) HRTEM image of a bycrystalline nanowire. The inserts are the corresponding FFT of the area framed with the black box and white box. (f) FFT of Figure e. The zone axis is $[10\bar{1}]_{FCC}$ $//[2\bar{1}\bar{1}\bar{3}]_{4H}$.

4.3.2 Experimental Observations

Once the sample was mounted, the NW was gradually pulled using the fine movement of the piezo tube until failure. We performed real time observations on the deformation process of a silver nanonwire in TEM with atomic resolution. The structure evolution of the nanowire with mechanical loading was recorded. The HRTEM micrographs shown in Figure 4.3 are still frames extracted from an in-situ tensile test video. These atomic resolution images show clearly the evolution of structure of the nanowire. At the straining beginning stage, the silver nanowire diameter is 33.2 nm, as shown in Fig 4.3a. Then, we use very low speed (about ~ 0.1 nm/s) to pull this nanowire. The estimated strain rate was about ~ 6.5 $\times 10^{-4}$ s^{-1}. At first, the nanowire was homogenously deformed and elongated uniformly along the wire axis upon pulling (Figure 4.3b). At 270 s, the center of the nanowire start local necking (white arrow in Fig. 4.3c indicates the start position of necking) and nanowire diameter shrink to 30.4 nm. Since the deformation is homogenous before necking, we can assume the volume of the nanowire keeps constant before necking, as indicated in Figure 4.1,

$$V_0 = V_t \tag{4.1}$$

Where V_0: the original volume of the nanowire, V_t: the volume of the nanowire at time t. From equation 4.1, we can get

$$\pi d_0^2 l_0 = \pi d_t^2 l_t \tag{4.2}$$

where d_0 is nanowire original diameter and l_0 is the nanowire original length, d_t and l_t are nanowire diameter and length the at time t. Engineering strain can be calculate by the following equation:

$$\varepsilon = \frac{\Delta l}{l_0} = \frac{l_t - l_0}{l_0} = \frac{l_t}{l_0} - 1 \tag{4.3}$$

Using equation 4-3, we can estimate that the engineering strain is

$$\varepsilon = \frac{l_t}{l_0} - 1 = \frac{d_0^2}{d_t^2} - 1 = \frac{33.2^2}{30.4^2} - 1 = 19.3\,\% .$$

This is an extra large strain for silver since the maximum elastic and plastic strain for silver in bulk form or whisker was as large as 4% and 2.5%[135,136].

After the necking initiated, the silver nanowire will deform locally at the necking area. Since the tensile direction is not parallel with the wire axis, it will add some shear on the nanowire. The diameter of the nanowire in the necking area will further decrease as the pulling is continued. The stress concentrated at the necking area will increase. Once the stress is over the threshold, dislocation will nucleate from the surface step, slide to the grain boundary, and multiplicate. Figure 4.3d shows the dislocation even can cross slip. The dislocation density increased further and accumulated in the necking area. As a result, a dislocation wall formed perpendicular to the grain boundary of the fcc and hcp phase. Further pulling will change the dislocation wall to a grain boundary and separate the silver nanowire into two parts. The white arrow in Figure 4.3d indicates a notch formed on the upper side. The notch is start point for the detaching two parts, which will separate along the formed grain boundary. At the final stage of the detaching process, a small nanobridge of 5 nm will

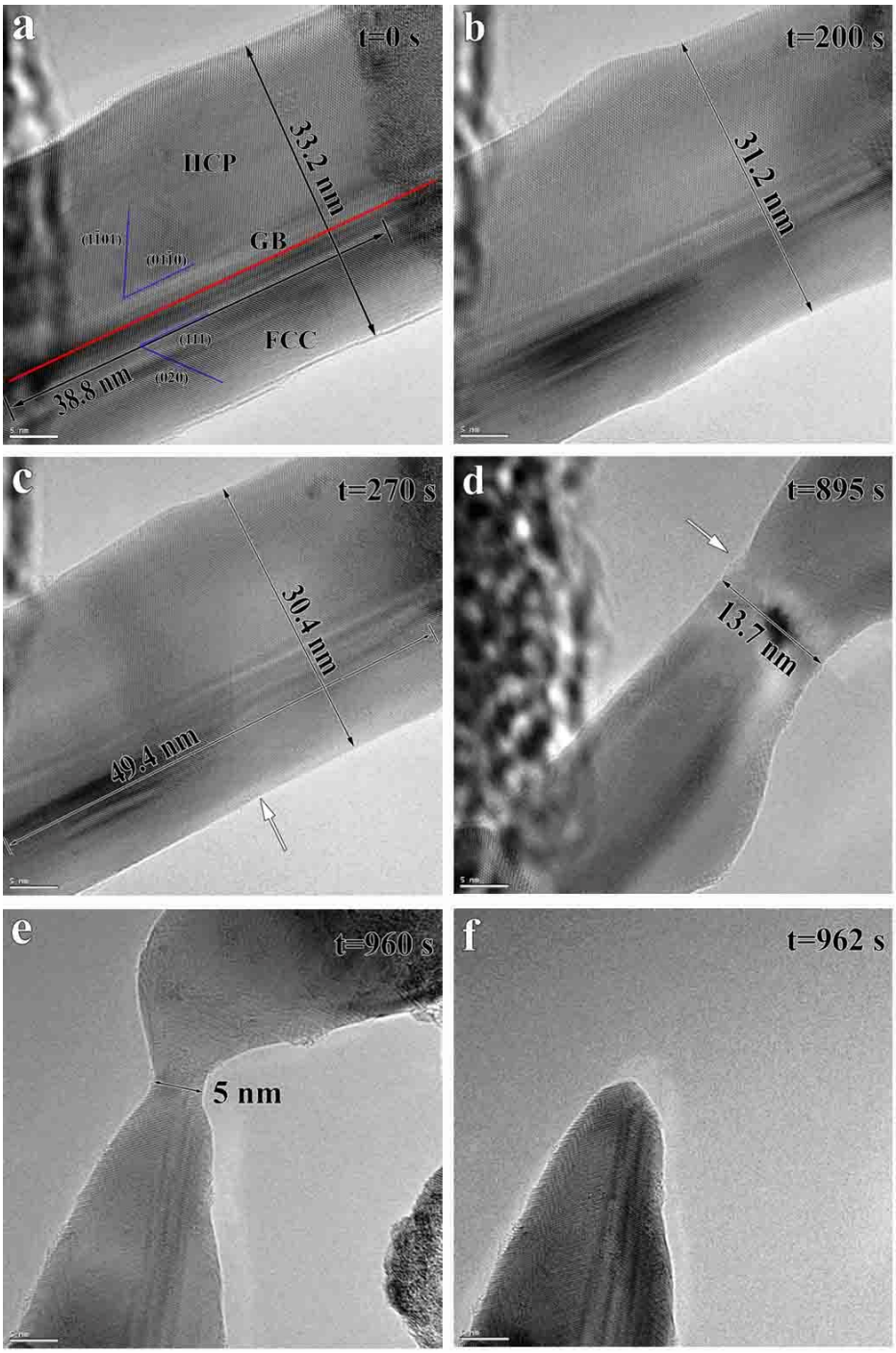

Figure 4.3: HRTEM observation of the deformation process of the 33.2 nm silver nanowire. (a) t=0 s, tensile test beginning; (b) t=200 s, the nanowire was uniformly elongated along the wire axis and its diameter decreases to 31.2 nm; (c) t=270 s, necking initiated at the center of the nanowire; (d) t=895 s, dislocations multiply in the necking area and form a grain boundary (white arrow indicates a notch); (e) t=960 s, 5 nm nanobridge formed between the two detaching parts; (f) After failure.

be formed (Fig. 4.3e). It reminds us at the nanowire formation by the mechanically controllable break junction (MCBJ) method[137]. Interestingly, the nanobridge was not necked down but uniformly elongated a little and finally broken. Figure 4.3f shows the morphology of the fracture nanowire. From crystallographic analysis, the two parts still have the two phases of fcc and hcp. But unlike the original nanowire, as the distance closes to the broken point, the ratio between hcp phase and fcc phase is increasing.

Checking the HRTEM images of the nanowire before necking in Figure 4.3, we found the contrast in the center area of the fcc part changed a lot and later the necking initiated from this area. It seems something happened in the center area. Figure 4.4a and Figure 4.4c are the silver nanowire morphologies when tensile test start and just before necking starting, respectively. Figure 4.4b and Figure 4.4d are the corresponding FFT of Figure 4.4a and Figure 4.4c, respectively. Comparing with FFT pattern of Figure 4.4a, no obvious new diffraction spots appear in the FFT of Figure 4.4d. This indicates that there seems to be no new crystal structure appearing in the silver nanowire during the tensile test. There are still the two phases of fcc and hcp. But as we can notice in the Figure 4.4d, all diffraction spots are elongated along the [111] direction, which is the wire axis. This means many stacking faults initiated along the [111] direction. To understand further what happened inside the fcc part, we performed inverse Fast Fourier-filtered transformation (IFFT) on the dynamic HRTEM micrographs. Figure 4.5 shows a series of IFFT images of the silver nanowrie from beginning to the state of necking starting. Figure 4.5a, c and d is the IFFT image corresponding to Figure 4.5a, b and c, respectively. From these IFFT images, the fcc and hcp phase can be easily indentified in the sample and clearly

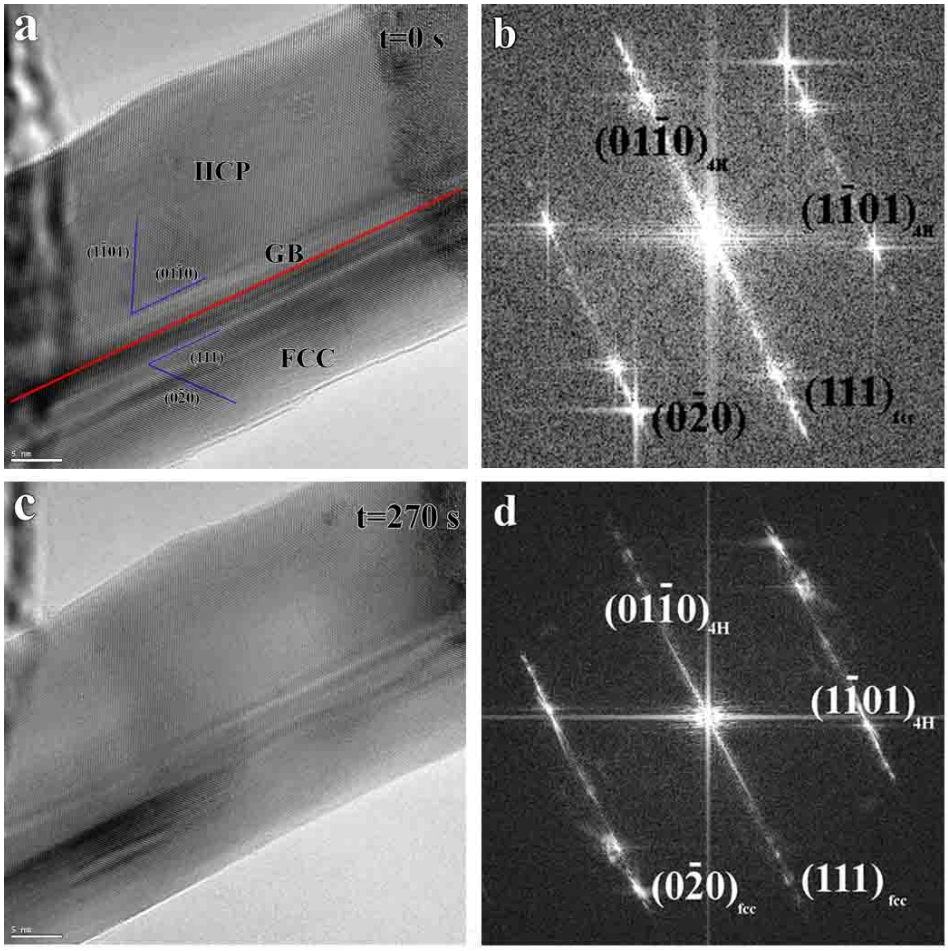

Figure 4.4: (a) The silver nanowire at beginning of the tensile test. (b) FFT of Figure a. (c) The silver nanowire just before necking. (d) FFT of Figure c.

is delineated by the red line. Surprisingly, as the nanowire elongated, the fcc phase area started shrinking (Figure 4.5b). It should note here that the fcc part is not decreased from the side contacting area, but from the surface and boundary area in the center and keeps going to the middle. Such shrinking induced a "necking" like morphology of the fcc part. The fcc part keep decreasing as the nanowire kept pulling and finally it was divided into two, as shown in Figure 4.5c. After further pulling, the two fcc parts kept separating and decreasing (Figure 4.5d).

It is well known that the stacking faults formation normally by consecutive Shockley partial dislocations gliding[138-140]. A question is raised: is the deformation

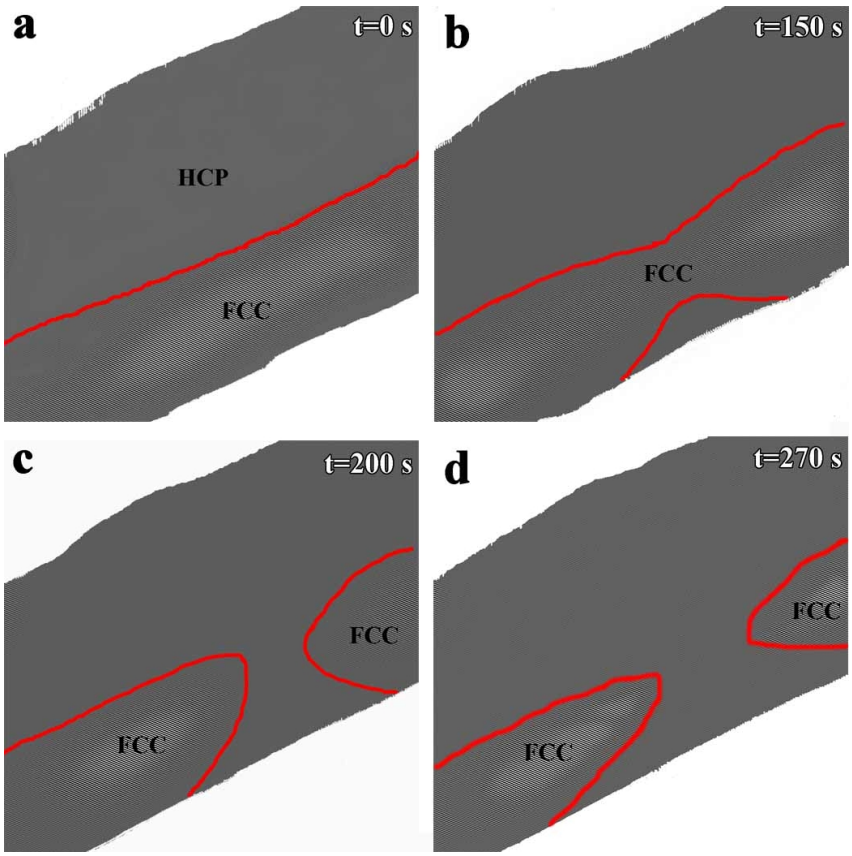

Figure 4.5: Dynamic IFFT images of structure evolution of the silver nanowire (red lines delineate the boundary of the fcc phase). (a) IFFT of Figure 4.3a. t=0 s, tensile test beginning; (b) t=150 s, fcc part "necked" down in the center; (c) IFFT image of Figure 4.3 b. t=200 s, fcc part was divided into two; (d) IFFT image of Figure 4.3 c. t=270 s, the two fcc parts kept separating and decreasing.

mechanism of the stacking faults formation here the same as the above one? To answer this question, we carried out the detailed analysis of the HRTEM images to understand what is going on during the transformation in our silver nanowire. Figure 4.6a, c and e show the morphologies of the silver nanowire at t=200 s to t=202 s during the tensile test. Figure 4.6b, d and f are the enlarged HRTEM images of the area framed with the black box in Figure 4.6a, c and e, respectively. From these images, we didn't find the partial dislocation glide on the (111) plane. But interestingly, we found vacancies formed inside the silver nanowire. As show in Figure 4.6b, vacancies were produced on

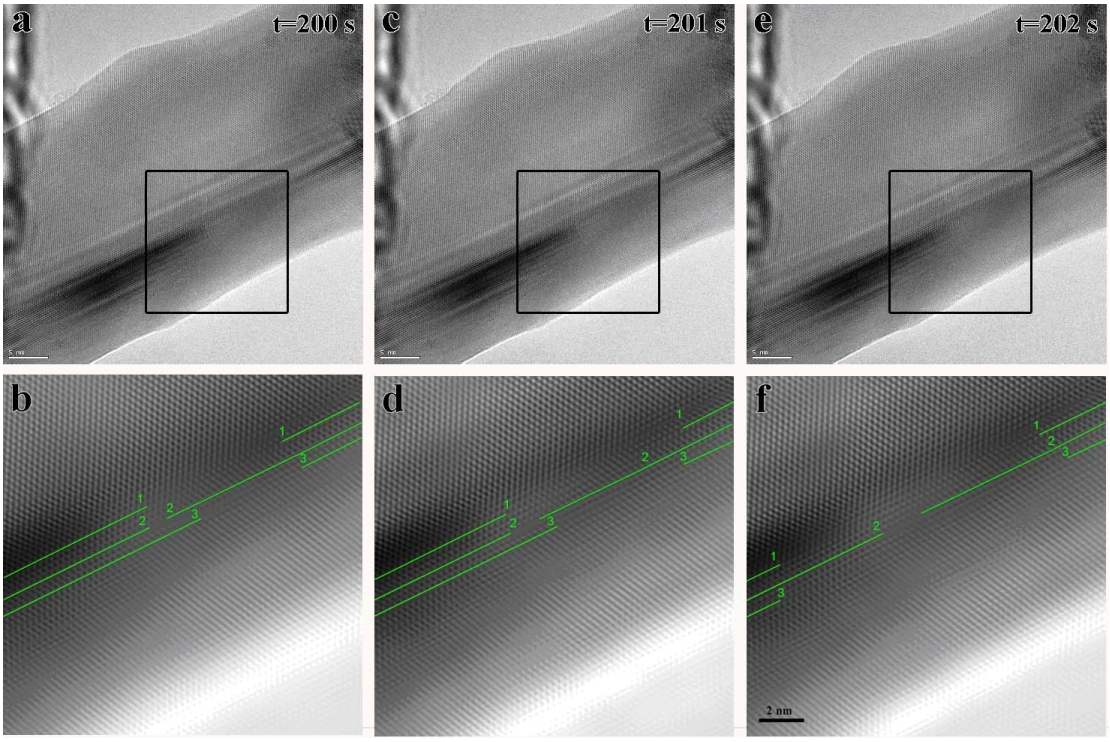

Figure 4.6: Frank loops formation and expansion. (a) Morphology of the silver nanowire at t=200 s. (b) Enlarged HRTEM image of the black box in Figure a. (c) Morphology of the silver nanowire at t=201 s. (d) Enlarged HRTEM image of the black box in Figure c. (e) Morphology of the silver nanowire at t=202 s. (f) Enlarged HRTEM image of the black box in Figure e.

the plane 2 and made the plane 2 to be two extra half planes, which are delineated by the green lines in images. Please note that two vacancy Frank loops already existed on the plane 1 and plane 3 at this moment. After the nanowire pulled a second, the vacancy cluster on plane 2 grew up along the (111) plane and formed a vacancy Frank loop with the length of 1.2 nm, as shown in Figure 4.6d. Once a frank loop formed inside the fcc Ag, a stacking fault (local hcp structure) is induced. The vacancy Frank loops on the plane 1 and plane 3 also expanded along the (111) plane. As the details show the Frank expansion in Figure 4.7, we can see the Frank loop 1 and Frank loop 3 expanded much faster than the Frank loop 2. We think that the surface and boundary may have the effect on the speed of the Frank loops close to

them. As the nanowire is loaded further, these vacancy Frank loops will become larger and larger. By the formation and expansion of the vacancy Frank loops, lots of stacking faults formed inside the silver nanowire and changed the local stacking sequence.

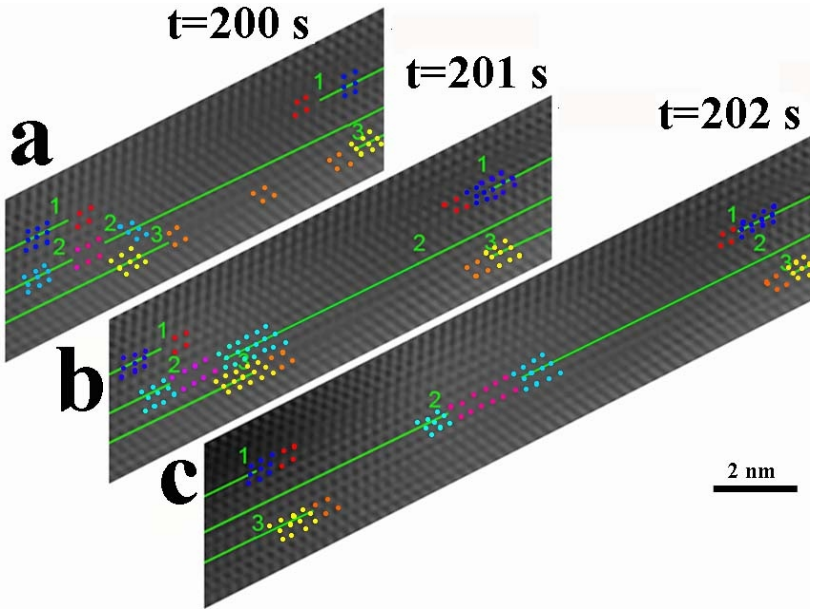

Figure 4.7: Details of the Frank loops expansion. (a) A Frank loop formed on plane 2. Another two Frank loops already existed on plane 1 and 3. (b) Frank loop 2 expanded one atomic distance. Frank loop 1 and Frank loop 3 also expanded along the tensile direction. (c) Frank loop 2 expanded one more atomic distance. Frank loop 1 and frank loop 3 expanded much fast than Frank loop 2.

4.4 DISCUSSION

Under cold working, a metastable phase will try to change to a stable one[141]. For buck silver, fcc is the stable phase because it has lower internal energy than other phases if we don't consider the effect from surface or interface. However, the surface effect will become more significant if the nanowire diameter shrink to less than a few tens

of nanometers, and in that case it should not be neglected. Recently, it was reported that silver nanoparticles[132] and silver nanowires[134] having a new structure 4H, which is different with bulk silver microstructure and indicates that the hcp structure will be a stable phase for silver in nanometer scale. To determine which phase will be more stable in nanoscale Ag, Liu et al.[134] did the calculation on the total energy difference between a 4H- and fcc Ag nanowire. The 4H-AgNW is demonstrated to be more energetically favorable if the nanowrie diameter smaller than 50 nm and it will have lowest energy when D* = 25.5 nm[134]. So it means that the fcc phase will be a metastable phase if the silver nanowire diameter decreasing to a small scale[134]. And if external energy affording on the metastable fcc phase, it is going to transform to the stable hcp phase. Under the tensile test, the force applied on the silver nanowire gave the energy to the fcc phase and assisted the transformation from fcc to hcp, which is more stable phase. The deformation-induced stacking faults (local hcp phase) in our tensile Ag nanowire is energy favored.

To explain the deformation induced stacking faults, various models had been proposed. All these models are based on dislocation mechanisms[142,143]. In these models, the stacking faults are formed by partial dislocations gliding on alternating close packed plane[138]. The Burgers vector for a Shockley partials is $b = 1/6 < 112 >_{FCC} = 1/3 < 1\bar{1}00 >_{HCP}$ [138]. And to provide accommodation for a small alteration of the close packed planes interplanar spacing, there should exist a perpendicular Burgers vector to the glide plane[144]. However, in our case, the stacking fault formation is not based on dislocation slip. We can rule out the dislocation mechanism from several aspects. First, if the extra-half planes in Figure 4.6 are relevant to Shockley partial dislocations gliding along the interfaces (111), the relevant extra-half planes should not be parallel to the interface. Second, if the

extra-half planes are relevant to the dislocations gliding, the slip planes should not be parallel to the interface plane. However, as we indicated in Figure 4.6b, d and f, the position of extra-half planes continuously moved parallel to the interface, this hypothesis may also be unfavorable. Moreover, at the starting of our tensile test, we strained the nanowire almost near the longitudinal direction. The Schmid factor for those interfacial dislocations is almost zero because the interface is parallel to the direction of straining. According to the Schmid law, Shockley partial dislocations' gliding is unfavorable in this case.

The stacking faults here are induced by Frank loops formation and expansion. It is well known that Frank loops can be produced by severe plastic deformation. As the size decreases, the nanowire can endure higher stress than bulk materials. Silver nanowire can sustain very high yield stress over 7 GPa[107]. So for the 33 nm silver nanowire in the present work, the stress can quickly build up upon loading. The high stress inside the nanowire can nucleate point defects (either vacancies or self-interstitial atoms). Since the vacancy formation energy is lower than for interstitial formation energy, the vacancies will be much easier to form[145]. As the deformation goes on, the vacancy density will increase. The vacancies keep lowering the free energy of the system by migrating, coalescing, and form microscopic clusters[145-147]. The energy of the system can be further lowering when a vacancy cluster absorbs more vacancies and grows to a vacancy Frank loop[145]. In general, it will be energetically unfavorable for creation of Frank loops throughout the matrix, but due to kinetics of point defect migration, it can be achievable at interfaces. The system always aims to reduce point defects to lower the total energy, which is the driving force for point defect move to the sink sites, i.e., interfaces, and extinction there.

4.5 CONCLUSIONS

The mechanical behavior of a 33 nm silver nanowire has been in-situ explored in HRTEM under low local strain rate. The plastic deformation of the silver nanowire is mainly attributed to the stacking faults formation, which is not like the plasticity of most crystalline materials dominated by dislocation nucleation and propagation. By in-situ HRTEM observation, we found the stacking faults are not induced by Shockley partial dislocations movement, but by the frank loops formation and expansion. Vacancies nucleated inside the silver nanowire, migrated and coalesced to form microscopic clusters. Further, a vacancy Frank loop can be formed from the vacancy cluster by absorbing more vacancies. The density of Frank loops increased during the deformation and induced more stacking faults, which changes the local stacking sequence, resulting a “necking” like morphology for the fcc part.

5.0 IN-SITU MECHANICAL TESTING OF SILICA NANOWIRES

5.1 INTRODUCTION

Owing to their small length scale and large surface atom number, small-scale structures exhibit unique mechanical properties comparing to their bulk form. To understand the deformation mechanism of small-scale structures, MD simulations have been employed to analyze their mechanical behaviour and revealed many novel phenomena such as single atomic chains formation during tensile testing[18,19], surface stress-induced phase transformation and lattice reorientation[15-17], shape memory and pseudoelastic behavior[20-22], and deformation induced amorphization[23,24]. The theoretical analyses and numerical simulations show there are strong size effects on the mechanical response and deformation mechanism of nanowire due to the high surface stresses[32,91,94,95]. The mechanical properties of nanostructures are implied to be different with that of their bulk forms.

Recently, a considerable effort has been put on the nanomechanical characterization of nanowires since the importance of evaluateing the applications of nanowires in nanotechnology field like nanoresonators[10,11], nanocantilever[117,148], piezoelectric nanogenerators[92,93], and NEMS. Recently, the tensile testing on Si and SiC nanowire show unusual mechanical properties can be shown in brittle materials with the reduction in dimensionality[69,110,112]. It is surprising that these nanowrie can sustain unusually large plasticity near room temperature[69,110,112]. However, these

nanowires were under electron beam irradiation during the deformation process. And it is showed that electron beam irradiation can help the plasticity[149]. So there raised a question: is the ductility from beam effect or size effect?

In this report, we performed in situ tensile measurement on silica glass nanowires in TEM. The study directly shows the continuous beam irradiation can totally change the mechanical behaviour of silica glass from brittle to ductile. And we show the glass nanowires larger than 20 nm can turn back brittle when beam is shut down. However, once the silica nanowire smaller than 20 nm, the e-beam damage will permanently trigger the brittle to ductile transition.

5.2 EXPERIMENTAL APPROACH

The tensile tests were carried out at room temperature inside a TEM, using a Nanofactory TEM-AFM platform (see schematics in Figure 5.2a), which allows for accurate force measurements (see Section 3.1.2 for a detailed instruction of the sample preparation and experimental set-up). A displacement control is provided by a piezo tube and the forces are measured from the deflection of the AFM tip. Engineering stresses are calculated from the forces using the wire diameter obtained from TEM. All the silica glass nanowires used in this study were directly drawn from large silica glass via a self-modulated taper-drawing process[124] (Figure 3.3 and Figure 3.4a). Short sections of 200 nm to 500 nm were cut from the silica glass nanowires and mounted between the tungsten probe and the AFM tip (Figure 3.4b). Dog-bone shaped samples with diameters in the range from 1 nm to 40 nm were prepared inside the TEM by a method similar to the hot-drawn or flame brushing technique[150] (see

Section 3.1.2.2). The tensile experiments were performed under beam and no beam conditions. For no beam experiments, only images at start and end were captured. The sample length before (l_0) and after fracture (l_f) were determined from the TEM pictures and used to calculate the plastic elongation at fracture, which was calculated according to $\varepsilon_{pm} = (l_f - l_0)/l_0$. After nanowire broken, the failure regions were further checked by HRTEM to determine whether the specimens crystallized during deformation (Figure 3.4c, d).

5.3 EXPERIMENTAL RESULTS

5.3.1 Tensile tests on silica nanowire under beam irradiation

Amorphous SiO_2 fibres with diameters over 50 nm exhibit brittle fracture during tensile deformation[100,151]. To check whether beam irradiation will affect the mechanical behavior of silica glass nanowier, we first performed continuous e-beam irradiation on silica glass nanowire with diameter over 100nm. Figure 5.1 shows an example of a 128.8 nm silica glass nanowire under in situ tensile elongation. The strain rate is 2.7×10^{-4} s^{-1} and the nanowire original length is 518 nm (Fig. 5.1a). Since the contacting area of the STM probe side is smaller than the middle area, the nanowire will undergo local thinning from this area upon loading (Figure 5.1b). After nanowire is pulled 69 minutes, the diameter of the thinning area reducing from 128.8 nm to 88 nm made the nanowires to a 337 nm diameter dog-bond-shaped sample (Figure 5.1c), which is ideal for the tensile test. Interestingly, this local thinning did

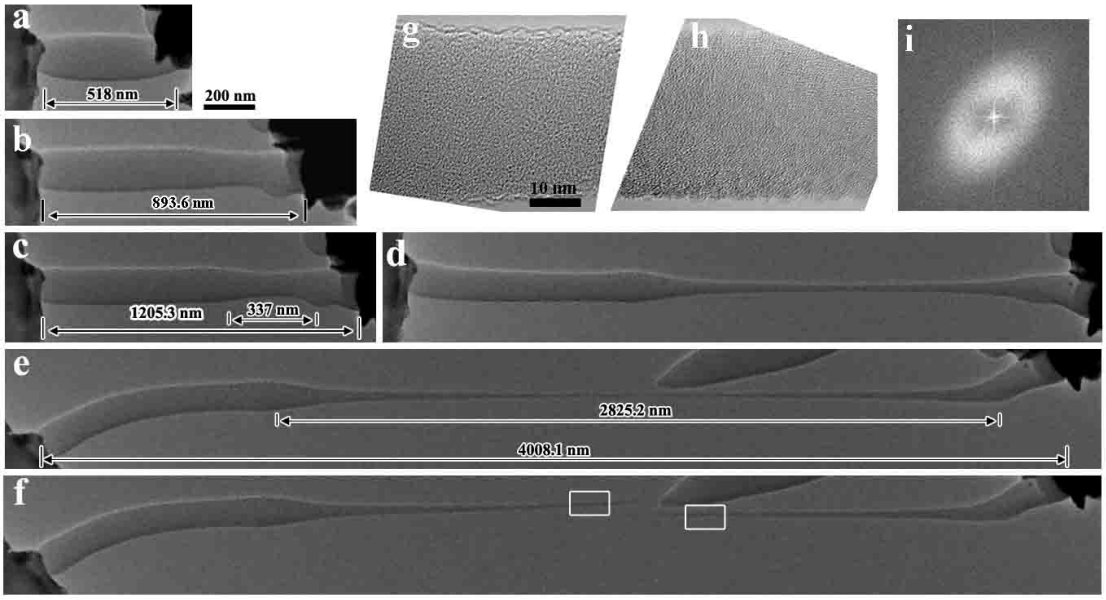

Figure 5.1: In situ tensile elongation of a 128.8 nm silica glass nanowire at strain rate of 2.7×10^{-4} s^{-1}. (a) t=0 min, tensile test beginning. (b) t=22 min, local thinning happened at the place near the contacting area of the STM probe side. (c) t=69 min, a dog-bond-shaped sample; (d) t=212 min, the dog-bond-shaped sample uniformly elongated along the wire axis; (e) t=246 min, the nanowire just before failure; (f) Failure of the nanowire. (g) and (h) are HRTEM images of the white framed regions in (f). (i) FFT of (h).

not induce the catastrophic failure of the sample, but uniform elongation of the nanowire along the tensile axis, which is very similar with deformation process of the superplastic ceramic and cabon nanotubes. It is incredible since nearly all the silicon and oxygen atoms diffuse and rearrange in the nanowires, which indicates the elongation process is quite depend on the bond-switching process. As the total elongation reached 384%, the piezo tube was up to its limitation on back-forward movement (Figure 5.1d). So we have to use the left-right mode to move the sample. Surprisingly, though the shear was put on the nanowire, it did not fail instantly and still uniformly elongated along its axis. Figure 5.1e shows the nanowire just before failure, the total tensile stain reached 673.8 % (If we just consider the local thinning

area, it experienced an elongation of 738.3 %). One more pulse will cause the sample finally to fail at the center of the dog-bond-shaped sample, but no obvious retraction of the two broken parts. This indicates the silica nanowire can sustain extraordinary plastic deformation with just a little elastic strain happened. The fractured nanowire was checked by HRTEM (Figure 5.1g and 5.1h). The HRTEM images and FFT image (Figure 5.1i) clearly demonstrate no deformation-induced crystallization in the uniform deformed amorphous silica nanowire.

5.3.2 Evaluation of possible irradiation damage

Electron beam during the sample preparation and imaging capturing process will cause the knock-on displacement and help the plastic deformation of silica nano ligements. The displacement energies for Si is 15~20 eV[152,153], which correspond to ~200 keV for the threshold incident energy calculated by the following formula[154]:

$$E_{\max} = E_0(1.02 + E_0/10^6)/(465.7A) \quad (5.1)$$

Our experiments were performed with 300 kV TEM accelerating voltage, therefore, displacement of Si occurred under beam irradiation. To determine whether or not the beam irradiation influences the composition, electron energy loss spectroscopy (EELS) was performed.

We checked the composition change of a nano ligament drawn under TEM from 56 nm (Figure 5.2a and b) to 24.6 nm (Figure 5.2c). The beam intensity and duration were ~2.5×10^{-3} A/cm^2 and 1 min similar to those used during dog-bone sample preparation. The EELS results of Si-L2,3 edge and O-K edge in Figure 5.2d and e showed the composition and structure changes for the sample before and after

irradiation. The intensity of Si-L2,3 edge decreasing after sample preparation and e-beam irradiation indicated that Si was displaced during e-beam irradiation and knocked out of the sample. The lack of a peak at ~531 eV indicates there is no detectable molecular oxygen (O_2) generated during irradiation[155]. However, it should note that although e-beam irradiation didn't transform the Si-O bonds into O_2, the electron beam still damage the Si-O bonds and produce the Si dangling bond and non-bridging oxygen.

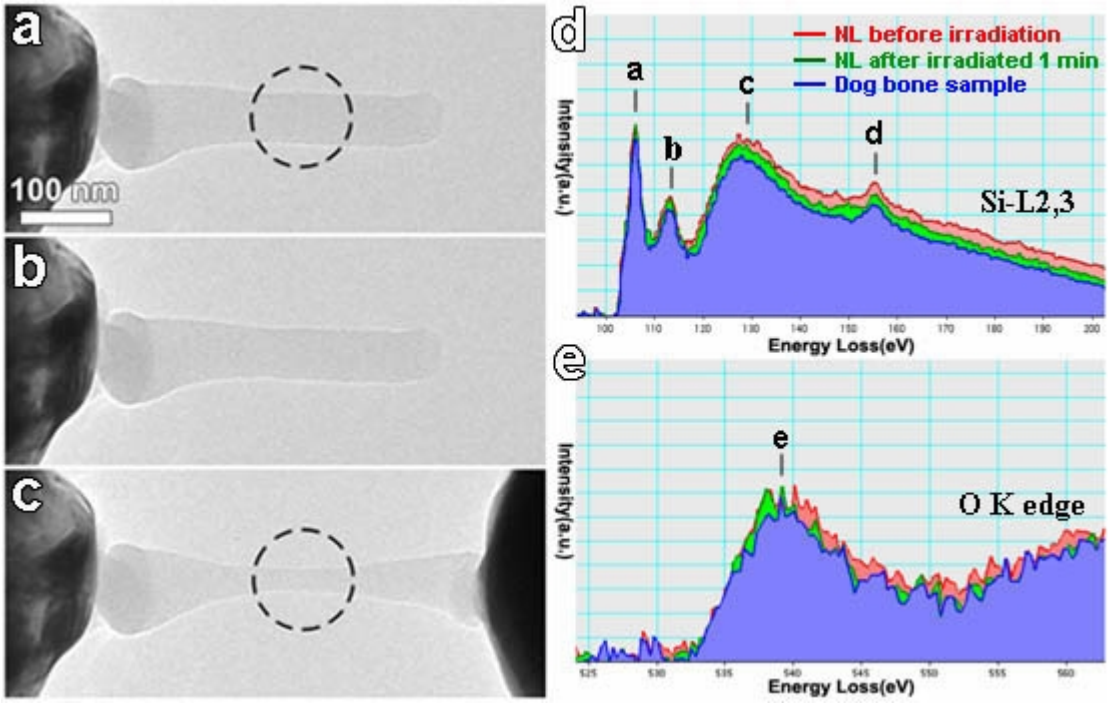

Figure 5.2: EELS on a 56 nm diameter nano ligament and an as-prepared 24.6 nm diameter dog-bone sample (the dotted circles marked the areas where we took the EELS). (a) and (b) show the nano ligament before and after 1 minute irradiation; (c) is an as-prepared dog-bone sample with a diameter of 24.6 nm for EELS test. (d) and (e) are the corresponding EELS spectra of Si-L2,3 edge and O-K edge. The EELS peak energy is: a-106.0, b-112.9, c-128.8, d-155.2, e-539.0 eV.

5.3.3 Tensile tests on silica nanowire under no beam condition

The continuous e-beam irradiation offered an unceasing source to produce Si dangling bond and non-bridging oxygen, which facilitated the bond switching process and helped the plastic flow of silica. Recently, irradiation experiment on glass show the e-beam damage of silica glass can recover ~90% after blanking beam for more than 2 minutes[155]. Here raise a question: is the ~10% left beam damage still large enough to change the mechanical behaviour of small scale silica glass?

To check whether the unrecovered beam damage will affect the deformation behavior of silica glass, we performed the tensile testing on 72 SiO_2 nanowires with diameters smaller than 50 nm after blanking beam more than 2 minutes. Figure 5.3 are examples of tensile tests on two nanowires with diameters of 33.9 and 5.3 nm. The sample with diameter of 33.9 nm shows clearly brittle failure (Figure 5.3b (before deformation) and Figure 5.3c (after fracture). Its stress vs. strain curve in Figure 5.3f shows only elastic deformation before brittle failure with a fracture stress of 2.2 GPa. The flat fracture surfaces (Figure 5.3c) orthogonal to the tensile axis also indicates no plastic deformation for the large sample. The smaller nanowire with diameter of 5.3 nm on the other hand shows clear ductile characteristics as exemplified by the plastic region in Figure 5.1f. The nanowire has a large elastic deformation of 5.4%, followed by a substantial plastic flow with flow stress of ~4.7 GPa. After the plastic flow, necking and ductile fracture were identified by TEM image as shown in Figure 5.3e in comparison with the sample before deformation (Figure 5.3d). The plastic elongation calculated from the TEM image (Figure 5.3e) is 8%. These results clear show that the unrecovered beam damage will not affect the mechanical behavior of silica nanowire if

its diameter is big enough. However, it really triggered the brittle to ductile transition when size of silica nanowire decreasing below some critical size.

The summary of the maximum plastic strains of the nanowires with different diameters is shown in Fig. 5.4. The nanowires with diameter smaller than 20 nm show

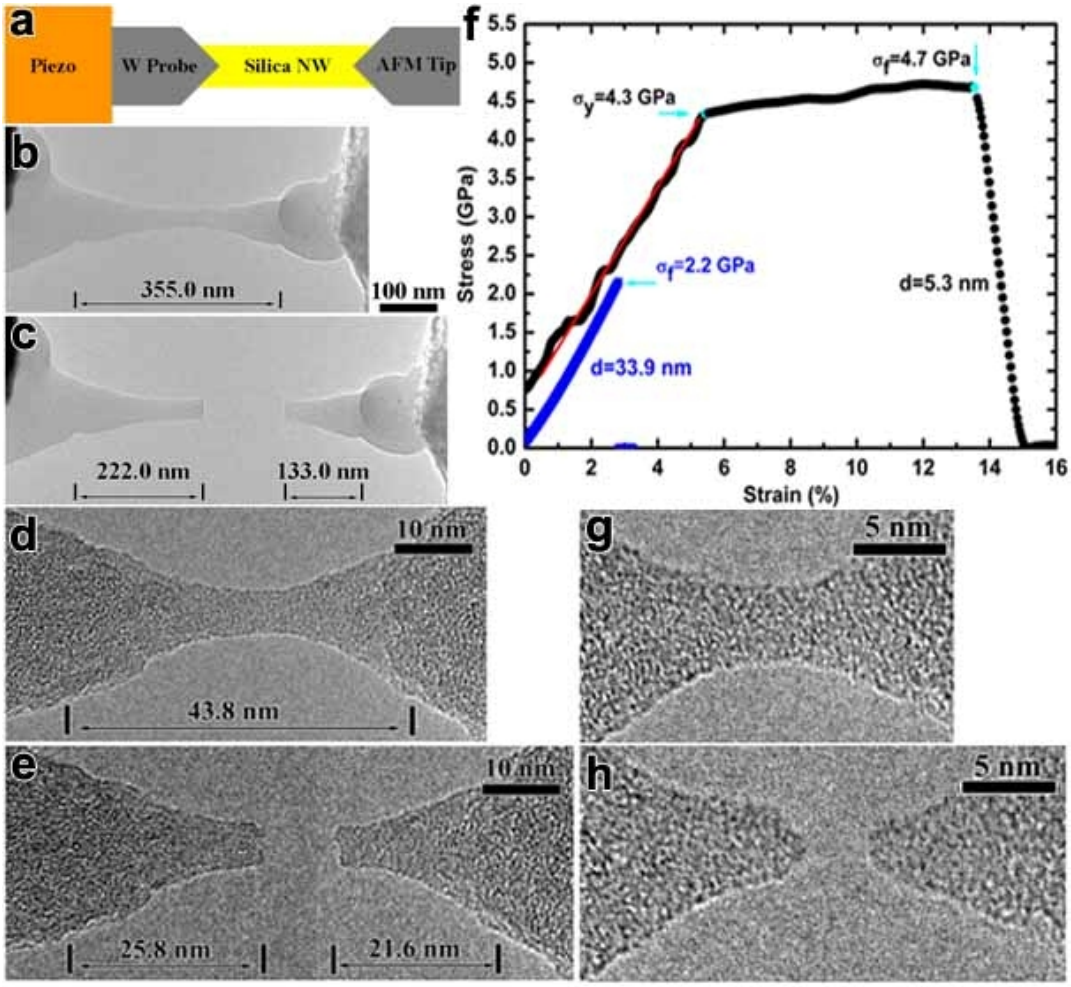

Figure 5.3: Tensile elongations of a 33.9 nm diameter NW at a strain rate of 3.3×10^{-2} s^{-1} and a 5.3 nm diameter NW at a strain rate of 1.1×10^{-2} s^{-1}. (a) Schematics of the experimental set-up. Images of the 33.9 nm NW b before loading and c after fracture. A 5.3 nm diameter NW (d) before loading and (e) after fracture with plastic elongation of 8%. (f) Strain-stress curves of the two NWs shown in b-e (the red line is a linear fit to the elastic slope of the 5.3 nm diameter NW). g and h show that necking occurred in a 4.0 nm diameter NW at a strain rate of 5.2×10^{-4} s^{-1}.

significant plastic deformation before failure, where shear deformation and necking during fracture have been identified in the TEM images (Figure 5.3e and 5.3h) taken after fracture, while those with diameter larger than 20 nm show brittleness with a flat fracture surface (Figure 5.3c). Figure 5.3g and 5.3h show necking occurred in a 4.0 nm diameter NW. The strain rate is 5.2×10^{-4} s^{-1}. Pronounced plastic elongations up to 18% have been found for the wires with diameters around 5 nm (Figure 5.4). As the diameter goes down to ~1 nm, the fracture stress approaches 13.2 GPa (Figure 5.5), which is result from high strain rate for visco-plastic silica, although the strength is close to the theoretical one of silica (16 GPa) under elastic-brittle mode[156]. These results demonstrated the deformation mode of e-beam damaged silica can change from completely elastic to elastic-plastic once the diameter of the silica nanowire is below a critical value at a set strain rate. According to the reference line for 1% elongation (magenta dotted line, Figure 5.4), for a strain rate of 10^{-1} s^{-1}, the critical diameter for the beam damages to trigger the onset of a ductile failure mode is about 5 nm. For a strain rate of 10^{-4} s^{-1}, it is about 18 nm. It might lead to ductility in even thicker nanowires by further decreasing the strain rate. Since the beam damage intensity is proportional inversed with r^2, as the sample size decreasing, the beam damage intensity will increase quickly, or in another word the dangling bonds density will become larger. The higher density dangling bonds will be much easier to facilitate the plastic flow of the beam damaged silica nanowire and enhanced the ductility. This induced the strong size effect on the ductility of the e-beam damaged silica nanowires. Shown from Figure 5.4, the silica nanowires ductility will peak up as the size decreasing. However, we should keep in mind that such size effect is actually some kind result from the beam effect.

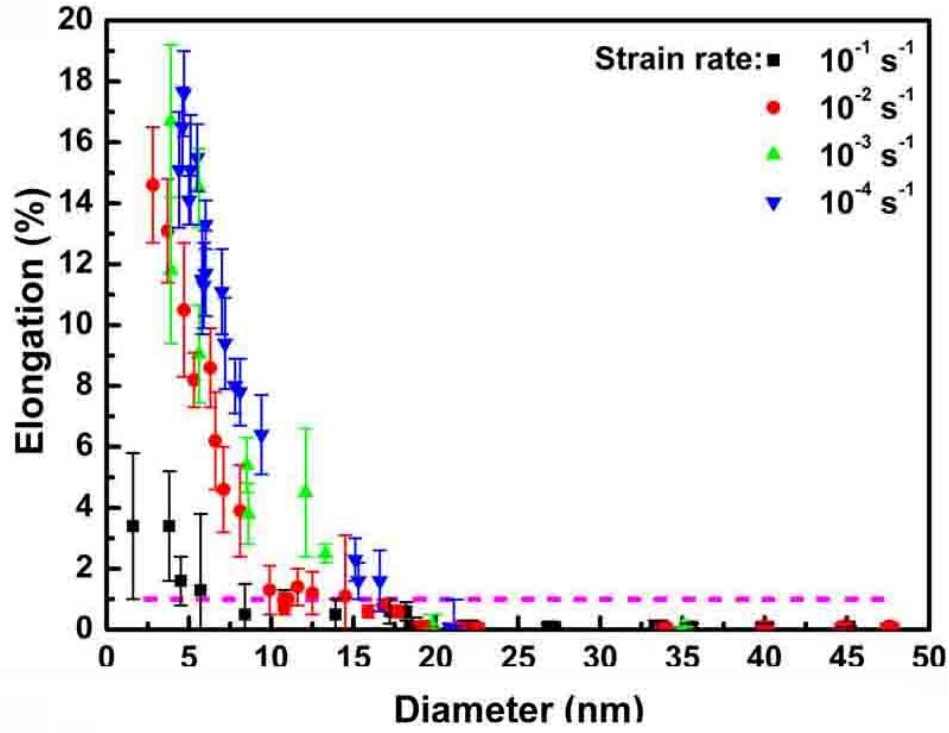

Figure 5.4: Summary of the maximum plastic strains of nanowires with different diameters (magenta dot line indicates 1% elongation).

The ductility is strain rate dependent: lower strain rates will lead to larger elongations (Figure 5.3). The strain rate depended ductility indicate the mechanical response of the silica nanowires is time dependent. For a viscous material, the stress and strain rate are related through the following expression under uniaxial tension[157],

$$\sigma = K\dot{\varepsilon}^{m} \tag{5.2}$$

Here K is a constant, and m denotes the strain rate hardening exponents. Normally, the strain rate hardening exponents ($= \partial \ln\sigma / \partial \ln\dot{\varepsilon}$) is between 0.3~0.8[158]. So from the formula (5.2), the flow stress will increase as the strain rate increased for a viscous material. To validate this, we perform the calculation on the fracture stress of the 72 silica nanowires. Table 5.1 summarized the fracture stress and plastic elongation of the silica nano ligaments in room temperature tensile experiments. The

engineering fracture stress was calculated by $4\Delta F/\pi d_0^2$, where ΔF refers to the force at the fracture point and d_0 is the initial diameter of the nano ligament. The plastic elongation was calculated by $(L_f - L_0)/L_0$, where L_0 and L_f are the initial and final (i.e. determined after fracture) gauge length of the nano ligament. Figure 5.5 clearly shows that the fracture stress is strain rate dependent if sample size below the critical size where beam damage takes effect. The dependence of the fracture stresses on strain rates shows a little scatter, but with a tendency of lower fracture stresses for slower strain rates[159]. The strain rate dependent fracture stresses clear shown beam damage will change the silica nanowire from elastic material to viscous material if the diameter of nanowire is less than the critical diameter. These results keep consistent with the conclusion from formula 5.1. Figure 5.5 shows fracture stress is increased as NW diameter decreases below 20 nm, where large visco-plasticity occurred due to e-beam effect. However, it is not clear why the fracture stress can reach such high (2.5-13 GPa) under with visco-plastic deformation mode.

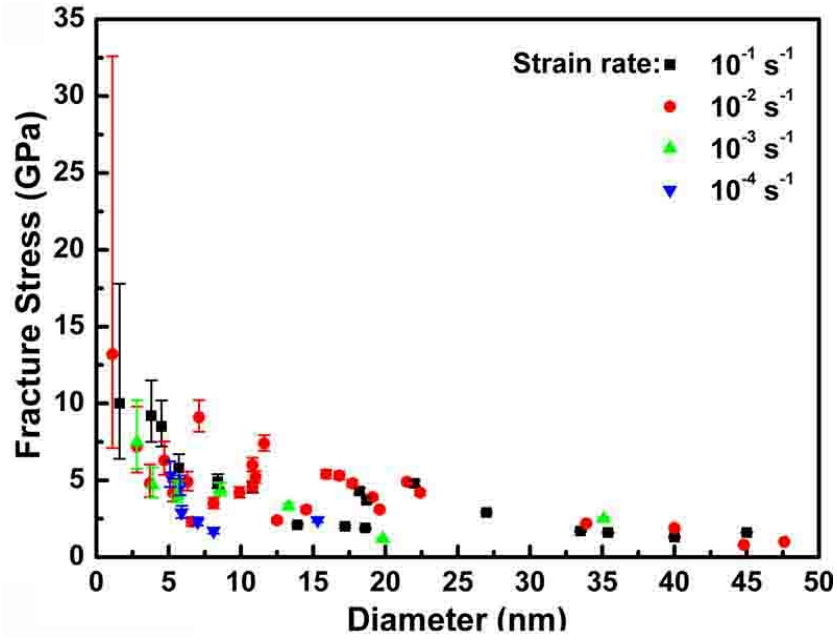

Figure 5.5: Summary of the fracture stresses of nanowires with different diameters.

The strain rate dependent stress also be observed in other amorphous systems such as metallic glasses[160,161] and ceramics[158]. The strain rate dependent plasticity indicated that the plastic deformation of the small diameter nanowire is a time dependent event. As revealed by MD simulation, the plastic deformation of such small nanowire is induced by a bond-switching process, which delayed formation of voids with critical size and subsequently postpones the eventual fracture (See Appendix for simulation details and results). The bond-switching process is a time dependent process. If the strain rate increased, the extent of completion of the bond-switching in the silica nanowire will be decreased since there will be enough time for some danging bonds to connect with the non-bridged oxygen, thus the elongation decreased.

Table 5.1: Summary of fracture stress and plastic elongation of SiO_2 nano ligaments

Sample	Initial diameter/Initial gauge length (nm/nm) d_0/L_0	Elongation (%) $(L_f-L_0)/L_0$	Fracture stress (GPa) $4\Delta F/\pi d_0^2$	Strain rate (s^{-1})
NL1-1	1.6/16.5	3.4	10.0	6.1×10^{-2}
NL1-2	3.8/21.8	3.4	9.2	1.2×10^{-1}
NL1-3	4.5/50.3	1.6	8.5	1.7×10^{-1}
NL1-4	5.7/15.8	1.3	5.8	1.6×10^{-1}
NL 1-5	8.4/38.7	0.5	4.9	5.0×10^{-1}
NL 1-6	10.8/95.1	0.9	4.5	1.1×10^{-1}
NL 1-7	13.9/75.1	0.5	2.1	1.3×10^{-1}
NL 1-8	17.2/93.1	0.6	2.0	1.1×10^{-1}
NL 1-9	18.2/142.4	0.6	4.3	7.0×10^{-2}
NL 1-10	18.6/99.7	0.0	1.9	1.2×10^{-1}
NL 1-11	18.7/193	0.0	3.7	6.0×10^{-2}
NL 1-12	22/118.9	0.0	4.8	8.4×10^{-2}
NL 1-13	27/160.3	0.0	2.9	6.2×10^{-2}
NL 1-14	33.5/151.9	0.0	1.7	6.6×10^{-2}
NL 1-15	35.4/168.6	0.0	1.6	5.9×10^{-2}

Table 5.1 (continued).

NL 1-16	40/192	0.0	1.3	5.2×10^{-2}
NL 1-17	45/344.3	0.0	1.6	5.8×10^{-2}
NL 2-1	1.1/11.2	—	13.2	1.8×10^{-2}
NL 2-2	2.8/21.2	14.6	7.2	4.7×10^{-2}
NL 2-3	3.7/24.2	13.1	4.8	9.4×10^{-3}
NL 2-4	4.7/17.8	10.5	6.3	4.2×10^{-2}
NL 2-5	5.3/43.8	8.2	4.2	1.1×10^{-2}
NL 2-6	6.3/30.4	8.6	4.9	6.9×10^{-3}
NL 2-7	6. 6/24.9	6.2	2.3	2.3×10^{-2}
NL 2-8	7.1/28.0	4.6	9.1	1.8×10^{-2}
NL 2-9	8.1/27.1	3.9	3.5	2.1×10^{-2}
NL 2-10	9.9/48.1	1.3	4.2	2.8×10^{-2}
NL 2-11	10.8/223.2	1.0	4.6	1.1×10^{-2}
NL 2-12	10.8/207.7	0.7	6.0	4.8×10^{-2}
NL 2-13	11/281.7	1.0	5.2	4.3×10^{-2}
NL 2-14	11.6/67.0	1.4	7.4	1.6×10^{-2}
NL 2-15	12.5/54.0	1.2	2.4	4.3×10^{-2}
NL 2-16	14.5/20.0	1.1	3.1	8.1×10^{-3}
NL 2-17	15.9/204.0	0.6	5.4	4.9×10^{-2}
NL 2-18	16.8/237.7	0.8	5.3	4.2×10^{-2}
NL 2-19	17.7/255.4	0.6	4.8	3.9×10^{-2}
NL 2-20	19.1/218.2	0.0	3.9	4.6×10^{-2}
NL 2-21	19.6/365.8	0.0	3.1	2.7×10^{-2}
NL 2-22	21.5/208.8	0.0	4.9	4.8×10^{-2}
NL 2-23	22.4/226.7	0.0	4.2	4.4×10^{-2}
NL 2-24	33.9/355.0	0.0	2.2	3.3×10^{-2}
NL 2-25	40/300.9	0.0	1.9	3.3×10^{-2}
NL 2-26	44.8/236.6	0.0	0.8	4.2×10^{-2}
NL 2-27	47.6/206.8	0.0	1.0	4.8×10^{-2}
NL 3-1	2.8/49.2	—	7.5	2.0×10^{-3}
NL 3-2	3.9/16.3	11.8	4.7	1.8×10^{-3}
NL 3-3	3.9/16.2	16.7	N/A	6.2×10^{-4}
NL 3-4	5.6/24.9	9.05	4.3	4.0×10^{-3}
NL 3-5	5.6/29.8	14.5	4.1	7.9×10^{-4}
NL 3-6	8.5/43.6	5.4	4.4	3.6×10^{-3}
NL 3-7	8.6/39.8	3.8	4.4	2.4×10^{-3}
NL 3-8	12.1/19.3	4.5	—	5.2×10^{-4}
NL 3-9	13.3/155.7	2.5	3.3	6.4×10^{-4}
NL 3-10	19.8/76.5	0.0	1.2	1.3×10^{-3}
NL 3-11	35.1/394.1	0.0	2.5	2.5×10^{-3}
NL 4-1	4.4/20.8	15.1	—	4.8×10^{-4}
NL 4-2	4.6/29.9	16.5	—	3.3×10^{-4}
NL 4-3	4.7/29.5	17.6	—	2.8×10^{-4}
NL 4-4	5.0/50.6	14.1	—	2.0×10^{-4}
NL 4-5	5.1/22.3	15.1	5.3	4.5×10^{-4}
NL 4-6	5.5/36.2	15.5	—	2.8×10^{-4}

Table 5.1 (continued).

NL 4-7	5.8/22.8	11.5	4.6	4.4×10^{-4}
NL 4-8	5.9/28.6	11.3	2.9	3.5×10^{-4}
NL 4-9	6.0/55.6	13.3	—	1.8×10^{-4}
NL 4-10	6.0/29.5	11.7	—	3.4×10^{-4}
NL 4-11	7.0/28.6	11.1	2.3	3.5×10^{-4}
NL 4-12	7.2/27.3	9.4	—	3.7×10^{-4}
NL 4-13	7.8/43.3	8.0	—	2.4×10^{-4}
NL 4-14	8.1/36.7	7.8	1.7	2.7×10^{-4}
NL 4-15	9.4/31.4	6.4	—	3.2×10^{-4}
NL 4-16	15.1/53.5	2.3	—	1.9×10^{-4}
NL 4-17	15.3/65.6	1.6	2.4	1.5×10^{-4}
NL 4-18	16.6/42.0	1.6	—	2.4×10^{-4}
NL 4-19	21.1/40.4	0.0	—	2.5×10^{-4}

—: Image not clear; Force not recorded

5.3.4 Experiment of comparision - Mechanical testing on diamond nanopillars

As revealed by the above section, we found if we keep the beam on during the whole straining process, the beam damage can change deformation of silica nanowire from brittle to ductile and even superplastic deformation. However, after blanking beam, the unrecovered beam damage will not change the deformation behavior of big diameter SiO_2 nano ligaments. But for the silica nanowrie with really small diameter, the e-beam during the sample preparation will inevitably produced more dangling bonds inside the nano ligaments and is enough to trigger the brittle to ductile transition. The beam induced atom displacement and the produced additional dangling bonds helped the plastic deformation of the silica nanowires with small diameter, although it has no effect on the deformation behavior of SiO_2 nanowire with big diameter (> 20 nm). To further check the beam effect, we chose another covalent bonding material: diamond, which is the strongest material in nature. The compression tests were carried out under room temperature inside a transmission

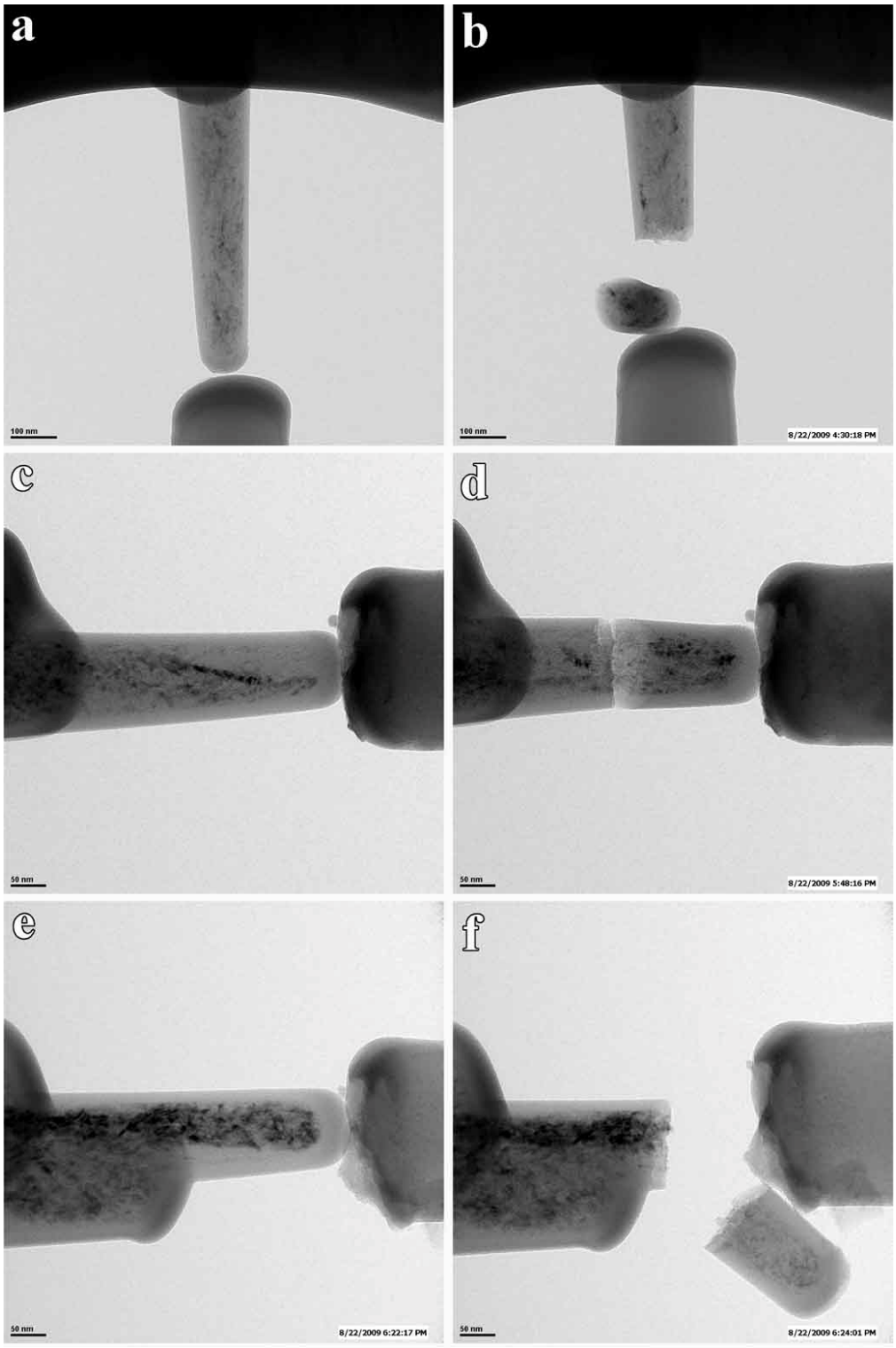

Figure 5.6: Compression tests on diamond nanopillars. (a) and (b) show a 87 nm diameter nanopillar before and after testing with beam current of 2×10^{-3} A/cm^2. (c) and (d) show a 88 nm diameter nanopillar before and after testing with beam current of 1.3×10^{-2} A/cm^2. (e) and (f) show a 66 nm diameter nanopillar before and after testing with beam current of 1.6×10^{-1} A/cm^2.

electron microscope (TEM), using a Nanofactory TEM-indenter platform (Fig. 3.9). We carried out the testing on different diameters nanopillars under different beam conditions to check the size effect and beam effect. Three examples of the compression tests on the diamond pillars are shown in Fig. 5.6. Upon compression, the 87 nm diameter diamond nanopillar under 2×10^{-3} A/cm^2 e-beam irradiation was elastically strained and facture. There is no any significant deformation and it quickly fractured with the crack nearly vertical to the applied tensile stress direction, producing a relatively flat surface (Fig. 5.6b). Under such condition, the diamond is totally brittle. To check if increasing beam density will change the deformation mode of diamond pillar change, we carried out the second set of compression test. In Fig. 5.6c, the beam current was increased to 1.3×10^{-2} A/cm^2 to irradiate an 88 nm diameter nanopillar. Same with the result shown in Fig. 5.6a and 5.6b, the nanopillar still showed brittle fracture. We increased the beam current and tried the testing on an even smaller pillar. As shown in Fig. 5.6e, a 66 nm diameter nanopillar was irradiated by e-beam with beam current of 1.6×10^{-1} A/cm^2. Even under such high density e-beam, no plastic deformation happened in the nanopillar with such small diameter. These results indicate that diamond is very stable under e-beam irradiation. Not like in silica, there will be no such enough dangling bonds produced during beam illumination to change the deformation behavior of diamond.

5.4 DISCUSSION

Ductility characterizes a material's ability to plastically deform and dissipate mechanical energy up to the point of gross failure. A room-temperature tensile ductility of silica glass is abnormal. Surfaces were usually perceived as preferred

crack initiation sites[162-164], due to damages caused in processing and by the environment. However, in our experiments, it appears that the ductility of the beam damaged silica nanowires is benefited from surfaces. To elucidate the roles of surfaces on the deformation and failure of silica, molecular dynamics (MD) simulations were performed (See Appendix for simulation details and results). The simulation indicates the plastic deformation of such small nanowire is due to the delayed formation of voids with critical size and subsequently postpones the eventual fracture. Upon pulling, the Si-O bonds will break and create void-like volumes. However, it can be recovered by the dangling Si that quickly bonds with the non-bridging O-defect and forms Si-O bonds again (Figure 9.1). We defined this process as a bond-switching process. MD reveals that there is a surface-plasticized region where bond-switching dominates. Our experiments suggest that the plasticized layer thickness is about 8–10 nm (Figure 5.4). In this region of enhanced plasticity flaws can be somewhat blunted, and once the surface affected region spans the wire it can deform plastically, as shown in Figure 5.4.

Glass transition temperature, Tg, of bulk silica glass is well known higher than 1200 ℃[165,166], so the temperature rise due to the e-beam irradiation was no more than a few tens of degrees[167,168], should have little consequence on the plasticity. However, based on the superplastic silica nanowire experiment (Figure 5.1) and compresion tests on diamond pillars (Figure 5.6), beam induced atom displacement and additional dangling bonds helped the plastic deformation of the silica nanowires with small diameter. The displacement energy of Si is 15~20 eV[152,153], calculated by the formula (5.1)[154], the TEM accelerating voltage (300keV) is large enough to cause Si atoms to displace and lead the formation of Si dangling bonds, which enhanced the bond switching process in SiO_2. So if there has source to unceasingly produce the enough

Si dangling bonds, ductility even superplastic behavior can be observed in even bigger diameter nanowire (Figure 5.1). However, beam damage can be partially recovered in glasses. Mkhoyan et al.[155] found the electron beam induced damage can totally recover in $CaO\text{-}Al_2O_3\text{-}SiO_2$ glass after the beam is off 2 min. But increasing the silica fraction, the recovery will be decreased to ~90% for $(CaO\text{-}Al_2O_3)_{0.67}\text{-}(2SiO_2)_{0.33}$ glass and 20% molecular O_2 will decrease. It was revealed that during beam damage, O_2 produced on amorphous SiO_2 can bond to the silicon dangling bonds[155,169], which induced the formation of links and peroxy radicals[155,170,171]. So the degree of the beam induced damage recovery is depended on how many oxygen atoms get involved in the bonding with silicon dangling bonds in the network, which cause the possibility of reabsorbing the silicon number by the nonbridging sites decreasing[155]. In our research, we used a very weak beam to produce the tensile sample. No detectable molecular oxygen (O_2) was generated during the sample preparation process (see section 5.3.2), so most silicon dangling bonds connected with the nonbridging oxygen atoms and reformed the Si-O bonds once the beam is off. If we blank beam on big diameter sample after long time exposure, the electron beam induced damage recovered ~90% after the beam is off. There are no enough additional dangling bonds and no external source to keep creating such defects during the whole straining process, the exist bond-switching process couldn't complete through the whole nanowire and thus the big diameter nanowires are still brittle even after long time beam exposure. The cavities or crack-nuclei in the interior of the sample have no way out but to coalesce, quickly exceeding the critical size and developing into a crack. And the pre-existing large flaws in bulk silica will quickly induce the sample failure. However, as sample size decreased, the beam damage intensity will increase up quickly. Once the sample size

below the critical diameter, the unrecovered beam induced the dangling bonds will exist across through the whole nanowire. The beam damage enhanced bond switching process spans the nanowires and thus trigger the plastic deformation.

Because of its high corresponding threshold value of incident energy E_0[154], which is ~330 keV[154], diamond behaves much stable under the beam. The TEM accelerating voltage is not large enough to cause C atoms to displace and lead the formation of enough C dangling bonds to facilitate the plastic flow. The diamond pillars behaving brittle also accounts for the larger sample size (>60nm), which will pre-exist more large flaws. These large structural flaws will operate due to the instability under high stress and cause brittle failure of the samples.

5.5 CONCLUSIONS

Assisted by beam, the silica glass nanowires can turn ductile, and even superplastic in very large size. The ductility of silica nanowires comes from the beam damages enhanced bond switching process. Beam blanked more than 2 minutes will partially recover the beam damage and change the mechanical response to brittle for nanowire bigger than 20 nm. However, the unrecovered beam damages are large enough to trigger the brittle to ductile transition in silica nanowire with size reduction to below 20 nm. The ductility, high strength (close to the theoretical strength) and high elastic-strain limit can prompt a wide range of applications for nanoscale glass structures[172]. The beam enhanced extreme ductility may also be used for a specific purpose such as manufacturing the optical nanofibers[150].

6.0 IN-SITU TEM OBSERVATION ON THE DEFORMATION OF NANOSCALE METALLIC GLASS[173]

6.1 INTRODUCTION

For metallic glasses, brittleness is consider as a critical weakness if applied in the engineering fields[173,174]. Therefore, there are lots of researches focusing on improving the plastic deformation capability of metallic glasses[175-177]. Recently, several metallic glass composites designed by Hofmann *et al.* showed a large ductility with plastic strain more than 10% and an apparent necking approaching fracture[178]. It was suggested by them that the plastic zone[179] in crack tip for most metallic glasses is around several micrometers. If we can control the size of metallic glass in micrometers range, then it should greatly improve the toughness or the capability of plastic deformation for metallic glass[173].

It well known that shear bands propogation caused the metallic glasses failure[173,180-183]. However, if view in a microscopic way, since the severe plastic deformation can be endured by shear band whether under deformation, metallic glasses is supposed to have outstanding toughness[182,184]. The maximum localized strain can reach 10^2-10^3% in the shear region, although the overall plastic strain is almost zero[185,186]. In general, the shear band thickness, t_s, is about 10-20 nm[185,187], and it can develop to ~1 μm through shear bands propagation[188]. In buck metallic glass, the shear band constrains the plastic deformation totally in such small area, which

causes the overall plastic deformation almost zero. However, what will happen if we control the tensile sample size nearly or smaller than the minimum size of shear band? In this circumstance, the shear band region is effective enough to totally cover the whole tensile sample[173]. Will some change happens in the metallic glass flow mechanism if the sample size below the smallest shear band thickness and how is it[173]?

The experiment results presented in this report directly give the evidence that metallic glass can turn ductile, even super plastic, if its size below 20 nm[173]. Large homogeneous tensile plasticity and obvious necking with the reduction in area nearly 100% is demonstrated in this nanometer length scaled metallic glass sample[173].

6.2 EXPERIMENTAL APPROACH

The in-situ tensile tests were carried using a Nanofactory TEM-STM system in a Tencai F30 TEM, as schematically illustrated in Figure 6.1a[173]. The metallic glass nanohill at the edge of the thin foil was bonded with a tungsten probe controlled by a piezo manipulator (Figure 6.1a). Once the nanohill sample and W probe were connected, it was pulled by the piezo manipulator with a strain rate less than 10^{-3} s^{-1} until failure. A nanohill sample without touched by W probe and after bonding are shown in Figure 6.1b and 1c. These high resolution TEM images demonstrated that the twin-jet polished sample is still amorphous and no crystallization after connectd by the W tip[173].

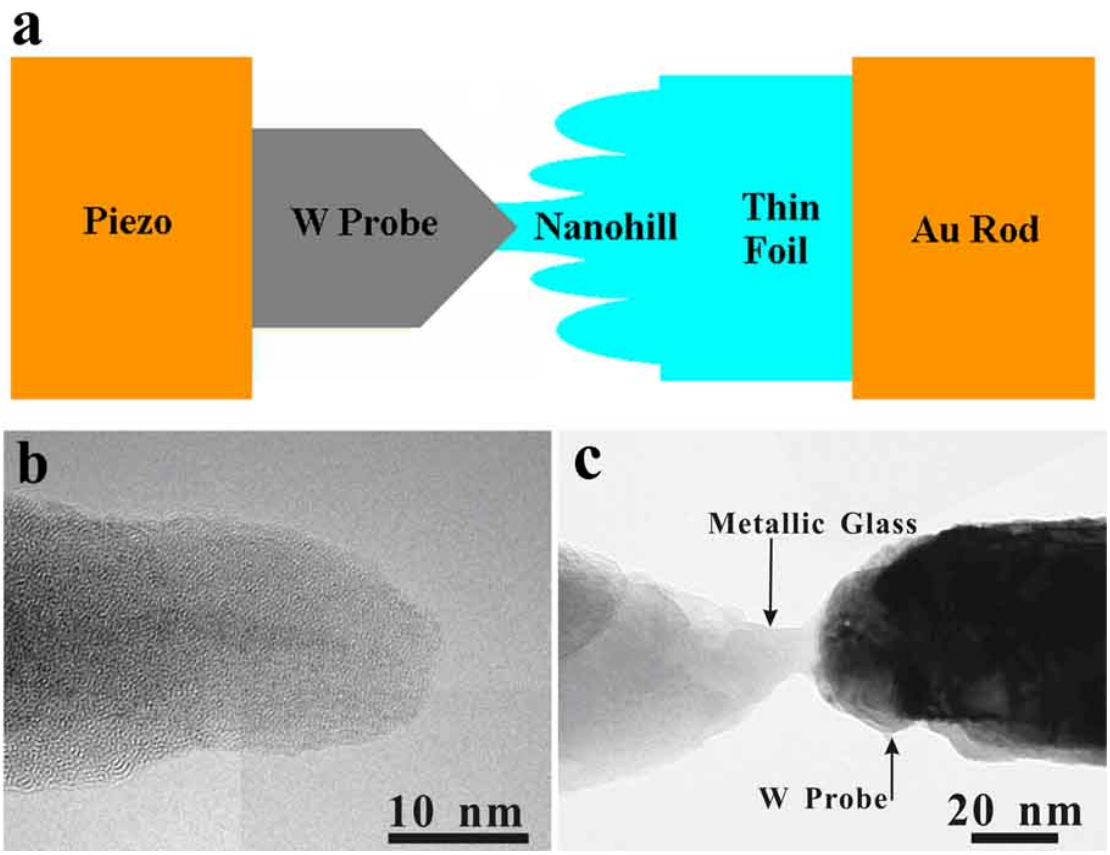

Figure 6.1: Experimental set-up. (a) The bond between the tungsten and the $Al_{90}Fe_5Ce_5$ sample. (b) HRTEM image of the $Al_{90}Fe_5Ce_5$ nanohill showing fully amorphous structure. (c) HRTEM image of the $Al_{90}Fe_5Ce_5$ nanohill after bonding exhibiting no crystalline structure[173].

6.3 EXPERIMENTAL RESULTS AND DISCUSSION

An example of a 14.3 nm diameter sample under in-situ tensile test is shown in Fig. 6.2 and 6.3. A large ductility was found in this nano size sample[173]. During the tensile testing, shear band propagation didn't happen in this nanoscaled metallic glass. The sample was first homogeneous plastic deformed, which induced the diameter shrinked to 4.5 nm from 14.3 nm (Figure 6.2a-6.2d). The strain of plastic deformation is as high as 200% calculated by the formula $\varepsilon = (l_t - l_0)/l_0$, here l_0 represents the

original length and l_t represents the length at time t. For metallic glasses, this plastic strain is extreme high, which usually just happen when metallic glass is around glass transition temperature. And the area reduction for the sample is calculated around 90% using the formula $\Psi=(A_0-A_t)/A_0$, here A_0 represents the area of cross section for original sample and A_t represents that for the sample before necking at time t[173]. The sample starts necking after the homogenous deformation, as shown in Fig. 6.3a. And there formed a nanobridge with diameter of 1.4 nm in the necking area (Figure 6.3b). As the sample continued deformed, the nanobridge diameter kept reducing (Figure 6.3b-6.3d). When the sample is close to break, the nanobridge was even developed to an atomic chain (Figure 6.3e). It is almost 100% for the area reduction of the necking area. An interesting thing is that the nanobridge as well the atomic chain is extremely flexible. It can be seen from Figure 6.3c to 6.3e, the nanobridge can be stretched from ~3 nm to ~3.4 nm in length. We also found the end of the nanobridge, which is close to the STM probe, has very high mobility. The end of the chain can move smoothly on the surface as it is extended[173]. The arrowheads in Figure 6.3c to 6.3e marked the mobile end positions, which clearly show the trace of the end gliding on the surface. Although Atomic chain has been reported in some ductile metals[18,19], there is no any previous reports demonstrate that atomic chain can exist in metallic glasses. The phenomena of superelongation in our nanoscaled metallic glass as well the formation of atomic chain point out that sample size decreasing to nanoscale can improve the ductility of the brittle metallic glass systems[173].

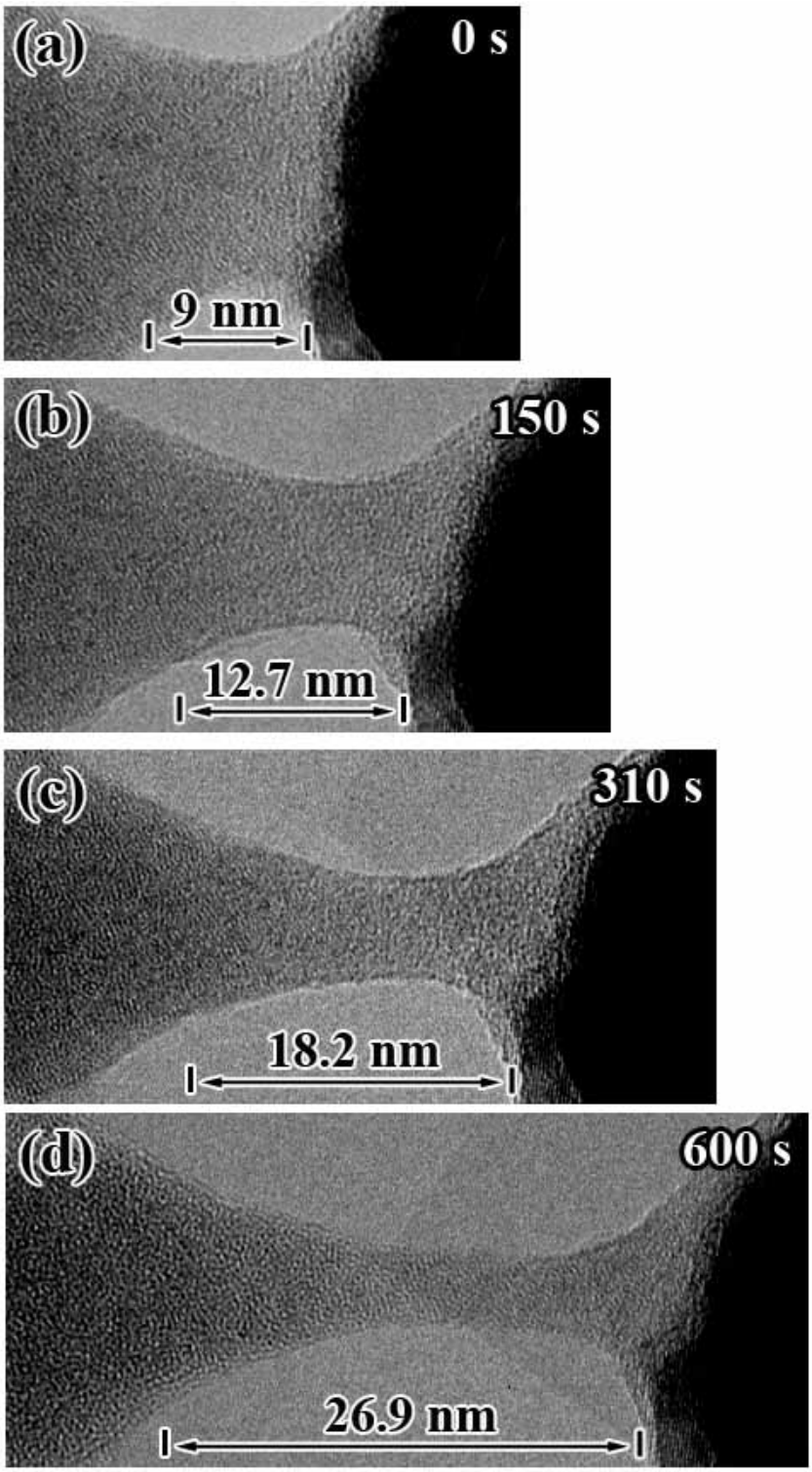

Figure 6.2: In-situ tensile test of a 14.3 nm diameter sample at a tensile strain rate of 2.9×10^{-3} s^{-1}. (a)-(d) HRTEM images of the superelongated metallic glass nanoscaled sample with (a) Original length of 9 nm and (d) final length of 26.9 nm[173].

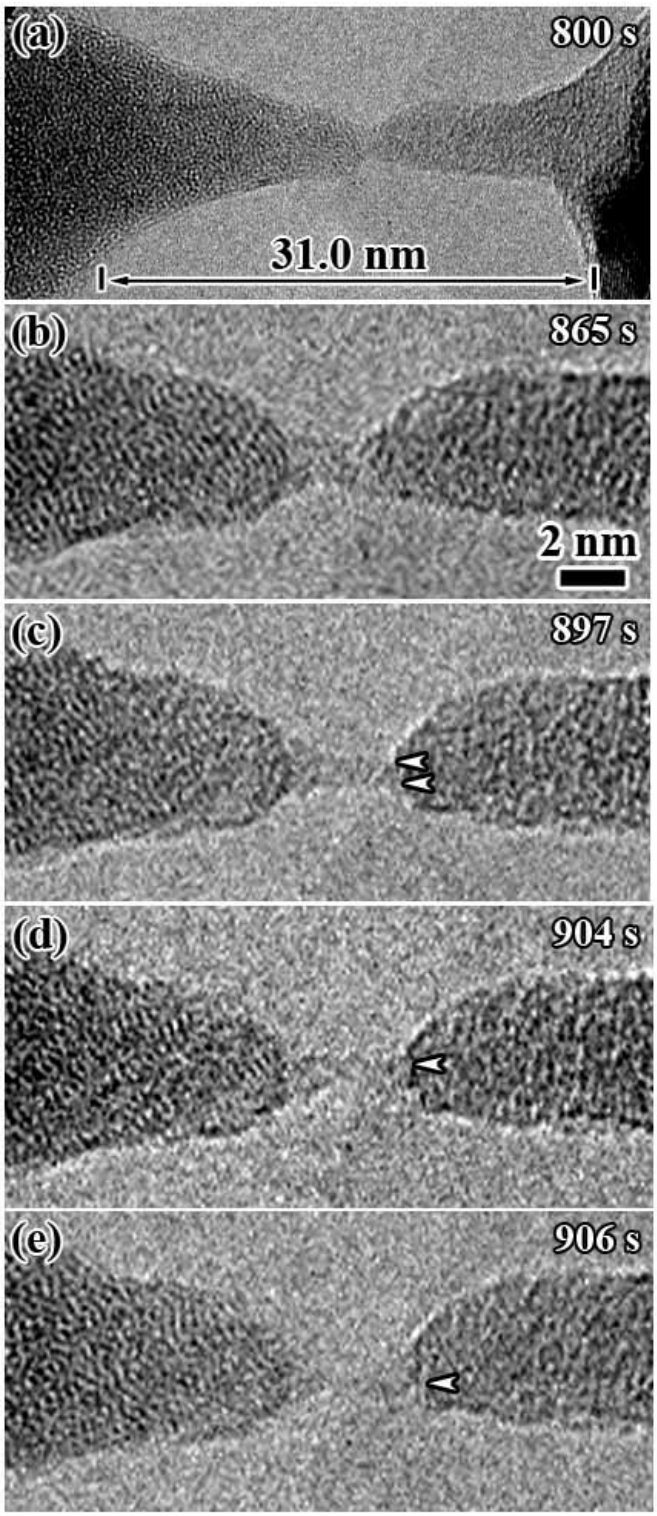

Figure 6.3: Formation of metallic glasses atomic chain. (a) Necking started in the center of the sample. (b) A nanobridge with diameter of 1.4 nm formed in the necking region. (c, d) The nanobridge shrink as the sample was continuously stretched. (e) An atomic chain was created. Its one end flexibly move on the surface. Arrowheads in (c) to (e) indicate the the nanobridge and atomic chain mobile end positions, show the trace [173].

The ductility of nanoscaled metallic glass sample may be enhanced by the irradiation of electron beam[173]. Two types of damaging was caused by electron beam: ionization and displacement. Ionization usually occurs in organic samples, therefore it is not considered in our samples which are all metallic[173]. Therefore displacement is considered as the likely damaging mechanism. For Al, Fe, Ce, the displacement energies are 17 eV[154], 40 eV[189] and 44 eV[190], so the corresponding electron beam energies are 180 keV, 630 keV and 1250 keV[173]. Ten TEM accelerating voltage in our experiments was 300 kV, consequently, it occurred Al displacement in our sample, which could possible help the plastic deformation of the metallic glass. Since metallic glass have excellent thermal conductivity, the effects from beam-heating can be neglected[191]. To make the effect from beam minimize, tensile testing with no beam condition were performed. In this condition, the electron beam was moved away when pulling the sample. For every ~2 minutes, the beam was moved back to capture a TEM image for around 5 seconds. It is surprising that there still happened superelongation for the metallic glass sample even under no beam condition[173]. It is shown in Fig. 6.4 that a ~8.3 length metallic glass nanoscaled sample (Figure 6.4a) was stretched to ~20.5 nm (Figure 6.4c). The calculated elongation is around 147% for this nanosized metallic glass sample. Even under no beam condition, the sample still shows superelongation as well necking. The similar phenomenon from with beam condition and no beam condition indicated that the extraordinary ductility may be the intrinsic property of metallic glasses in nanoscale, though electron beam could do favor on it. For the beam heating effect, it can be neglected because the beam in normal imaging condition will not increase temperature more than 50 K in metals[192,193]. It was confirmed by Fisher's theory that the increase temperature should

no more than 10 K in electron irradiated aluminum foil[193]. Thus, the electron beam heating should have no help on the superelongation[173].

In what follows, we discuss possible mechanisms leading to the extraordinary ductility of nanosized metallic glasses[173]. For bulk metallic glass, homogeneous plastic deformation only occurs when it is near glass transition temperature[180,194], which is far higher than room temperature. Under that condition, viscous flow causes the large ductility, and superplastic behavior has to require high strain-rate sensitivity. However, it is revealed from our results that the brittle metallic glass can change to extreme plastic even under ambient temperature by decreasing size to nanometer range. It is apparently unlike what shown in bulk tensile metallic glass where brittle deformation is quite universal. Firstly, from the aspect of global plasticity, it shows very large plasticity in the nanosized metallic glass. Secondly, from the view point of microscopic mechanism, no shear band assisted the deformation of nanosized metallic glass. These deformation behaviors are drastically different from that of bulk metallic glass. In the following, we will do more discussion on the factors which cause nanosized metallic glasses deform uniquely[173].

From the viewpoint of the thickness of shear band (t_s) in metallic glass, due to the sample size being close to t_s, if there exists shear band in it, the whole effective sample will be covered by the shear band[173]. For a fully developed and mature shear band, if we assume 10 nm for thickness of the incipient shear band, the diameter of the nucleus would be around 0.5 μm[195]. Therefore, the shear band for the present sample has no enough space to develop itself to the unstable level. The shear transform zones (STZ) will robustly collaborate together in this quite small volume, and propagate all through the entire[173]. In the meantime, the atomic diffusion induced

short-range or modest-range structure transformation will be significant in this case and help the homogeneous deformation[173,191].

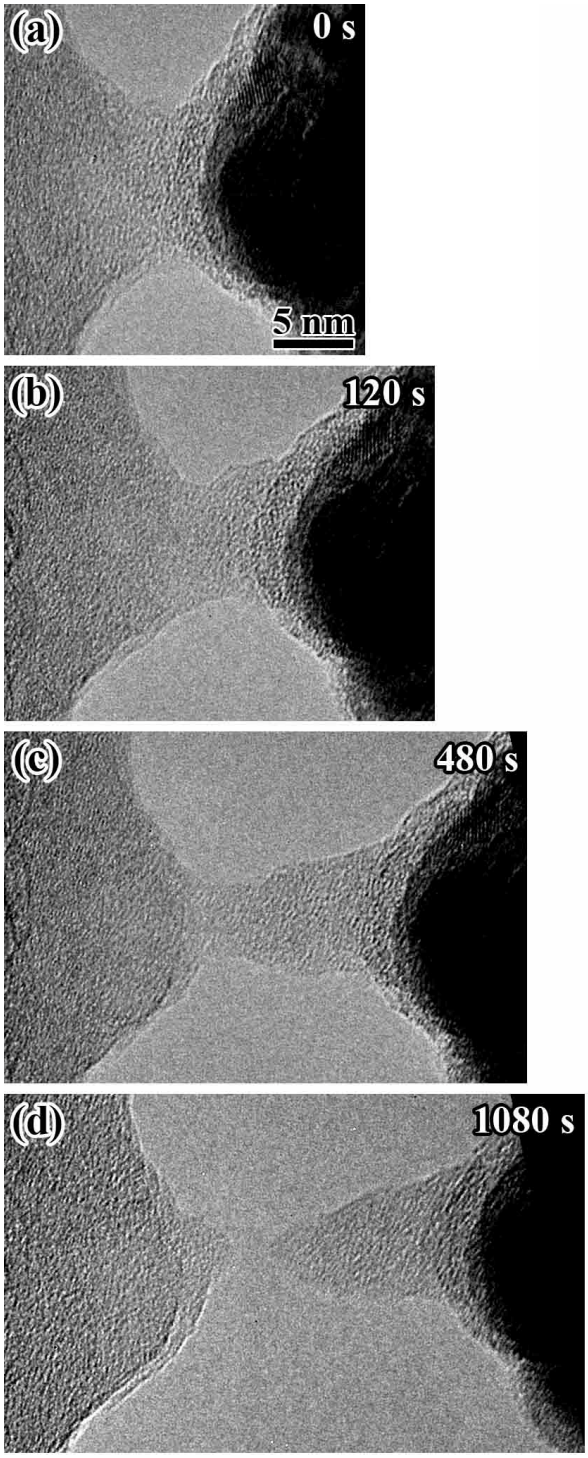

Figure 6.4: Tensile test a nanosized metallic glass sample at a strain rate of 3.1×10^{-3} s^{-1} under no beam condition[173].

The surface effect will turn significant if the sample size decreasing to nanoscale[173,196-198]. The surface stress will turn stronger as the sample size decreasing. To compensate the surface stress induced compressive stress on the sample, it will have to apply some tensile stress. The amount of the extra applied tensile stress can be estimated using γ / r [54], where γ is the surface energy considering a cylindrical sample with radius, *r*, under tension. This surface induced compressive stresses could make the tensile fracture strength enhanced to some extent, and it could postpone the shear band nucleation in the nanoscaled sample. Meanwhile, under the constraint of the surface compressive stress, a normal stress close the band help operating shear band, resulting in a more stable shear deformation[178,199]. At the nanoscale, the shear transform zone (STZ) will react with the compressive stress outside, and make STZ multiple and pervade into the whole effective sample. Meanwhile, small size will decrease the statistic distribution of defects whether in large size or small size. This results in a STZ difficult to initiate and further to grow up to a mature shear band, which is regard as another fact for the plastic strain increasing[173].

Based on the deformation energy viewpoint, the stored elastic energy is mostly dissipated as heat on the surface of fracture plane because of the shear deformation highly localized in metallic glass[173,200]. The important roles of heat are: it can make shear band softening and have effect on the metallic glass catastrophic fracture[201]. The releasing of elastic energy upon fracture induced the shear fracture surface energy density can be generally proportional to the sample size (the diameter of a cylindrical sample). As sample size reducing, the dissipated energy density on the fracture surface of shear plane decreases linearly. So the stability of the shear band can be enhanced by sample size decreasing, i.e., the crack forming by the propagation of shear band becomes hard. Therefore, as sample size reducing, it will turn more

likely that homogeneous shear deformation happen in the full sample, thus the metallic glass plasticity can be enhanced[173,191,202].

Recently, Greer et al. reported a mode change from highly localized deformation to homogeneous deformation in Zr-based metallic glass nanopillars with diameter of 100nm, and keep the yield strength no change[203]. As we know, there are two competing processes existing when metallic glass deforms: shear-band propagation by cracks and homogeneous flow[203]. As sample size varies, each process will give different contribution on the whole deformation. Considering these factors, a phenomenological model was proposed to explain this special homogeneous deformation caused by size effect[203]. The pre-existing shear band propagation to fracture drive stress is given as[204]:

$$\sigma = \sqrt{\frac{2\sqrt{2}\Gamma E}{ad}}$$

As shown in the deformation map in their report, there is a critical sample size d* for deformation transiting from propagation of shear-band to homogeneous deformation, however the sample size do not have affect on the stress initiating room temperature homogeneous flow[203]. Normally, the maximum shear stress τ can be estimated by $\tau/G=0.036-0.016(T/T_g)^{2/3}$and the ideal strength is estimated around $E/30$[203,205]. With E=66 GPa[206], G=24.4 GPa and T_g=543 K[207], the stress for homogeneous deformation of our $Al_{90}Fe_5Ce_5$ metallic glass is estimated between 1.3 and 2.2 GPa. When the size of specimen is much bigger than d*, the shear-band propagation will dominate the metallic glass deformation[203]. However, once the size of specimen is lesser than the d*, the homogeneous deformation will dominate since the shear band embryo will be stable enough to not propagated[203]. The materials will finally fail when the stress is increased enough to over the shear-band propagation stress[203].

Referring with the estimation on Γ from Greer et al[203], Γ is estimated to be ~10 Jm^{-2}, and consider a ~6.5, the critical sample size d* is estimated to be ~60－170 nm. Our sample size is only 14.3nm, which is much smaller than the d*, so referring the deformation map[203], the homogeneous deformation will prevail in such small sample, which is consistent with our observation.

The phenomenon that occurred in the present nanoscale sample will be helpful for us to understand the physical nature of metallic glass and indicative for us to design new metallic glass materials with excellent performance properties[173]. One can control the bulk metallic glass in nanoscale pieces by introducing the second phase. Each piece of metallic glass with nanoscale will display great tensile plastic deformation. The cooperation of all pieces of metallic glass results in considerable tensile plastic deformation. Recent progress in Zr-Ti-based metallic glass composite can be a good example of this condition[178,208]. In that work, these series of metallic glass composites exhibits great tensile plastic deformation, and even necking occurred in them[173].

6.4 CONCLUSIONS

Quite difference with the bulk metallic glasses which show disastrous tensile failure, nanosized metallic glass exhibits extreme ductility with uniform elongation[173]. After the superelongation, the area reduction can reach 100% in the necking region. However, shear bands were not found during the whole deformation process and is not the reason to cause the excellent tensile plasticity. These findings can be used to improve the understanding on various metallic glasses systems with their mechanical

properties, deformation behavior, and fracture mechanisms. And it can indicate us a potential direction to design metallic glass materials with excellent performance in engineering fields[173].

7.0 PULLING SUPERPLASTIC SODIUM CHLORIDE NANOWIRES FROM THE COMMON SALT SURFACE[209]

7.1 INTRODUCTION

It is a abnormal property of material that it has superplasticity at ambient temperature, in other word it can elongated more than >100% until fracture, which have only been observed in some covalent materials[209,210]. If nanoscaled sodium chloride (the common salts) can have superplasticity, it will be really unexpected because we know that salt is brittle material and we can squash them using fingers. The only materials can be pulled into nanowires in condition lower than their melting point are metals [211-214]. It is not reported that the superplasticity can exsit in other one-dimensional nanomaterials, such as ceramic nanowires and carbon nanotubes[39,69,110,112,215], to foresee such special behavior for ionic nanowires. It is really necessary to comprehensive know the NaCl deformation mechanism since it can give the guide to understand the geotechnical problems by relating the measurements from labrotary[216,217]. It is will be extremely useful for comprehending the aerosols physicochemical reactions of sea salt. The wide problems such as asthmatic reactions in human body, cloud nucleation, and smog formation has implicated this[218,219]. By imaging in atomic-scale, NaCl crystal surfaces has been demonstrated to transform noticeably in environments with humid[220,221]. Normally, if the atomic diffusion close to dislocations, kinks, steps and surface[209], the bulk plasticity induced will be much faster [222,223]. In this report, it will show a superplastic NaCl nanowire can be formed

by retracting a sharp tip from the common salt crystal. This reveals that the plastic deformation can exist in nanoscaled sodium chloride and even in a pretty dry environment, however under the shower of electrons. The superplasticity is because of atomic diffusion, which facilitates quick migration of atoms and heal the defect induced by deformation or electron irradiation[209]. It is also discussed in this report on the stabilizing the superplastic deformation by possible Na^+ to Na partial reduction[209].

7.2 EXPERIMENTAL APPROACH

The in-situ experiments were performed under 100 keV with low dose 1 A/cm^2 in a FEI TEM (Tencai F30) using a TEM-STM platform (Nanofactory)[209]. The nanowires was formed by retracting a gold probe from NaCl(100) surface[209].

7.3 EXPERIMENTAL RESULTS AND DISCUSSION

Figure 7.1a shows a nanowire under superelongation and compression with length of ～580 nm at begining[209]. In the left side of the nanowire, the crystal contrast was appeared in a heavily strained single crystal[209]. As shown in Fig 7.1a and 7.1b, the middle part of the nanowire was uniformly elongated first during stretching until two ~30 nm height surface steps shown close to its two ends (Figure 7.1c). Upon further stretching, only the section of the nanowire between the two steps elongated drastically. Because of reaching the limitation of the manipulator in this pulling direction, it could not stretch the nanowire any more. The final length of the obtained extreme long nanowire is ～2190 nm with no fracture. It is ～280% for the

elongation of this nanowrie, however this is only minimum value[209]. The reduction of the nanowire diameter during the superelongation is from 210 nm (Fig. 7.1a) to 100 nm (Fig. 7.1c), however it is increased by 75% for the nanowire volume. The increasing of volume is a sign of that there happened transportation of NaCl from the to the nanowire. The contrast change appearing in Figure 7.1c may be caused by crystalline structure formation as the nanowire elongated and it is thought because of the atomic diffusion. And it is possible some recrystallization induced by deformation caused by this. However dislocation activities such as nucleation or propagation were not detected during the elongation although it show heavily strain contrast in those areas with recrystallization. There has only homogeneous gray contrast shown in the elongated nanowire. If dislocation activity is stable during the tensile process, it should show strong diffraction contrast in the strained nanowire. A possibility is that dislocation movement is too quick to move out of the surface of nanowire and thus TEM imaging couldn't capture it[224]. After the limitation of the manipulator in this pulling direction reached, we can only compress the nanowire by pushing back the STM probe as shown in Fig. 7.1d and 7.1e. It is remarkable that we can buckle the over 90° as the overlapped nanowire in Fig. 7.1f indicated. During the compression, it intermittently appeared the strong contrast resulted from recrystallization (Figure 7.1e), which also designated the deformation is dominated by atomic diffusion[209].

The electron beam irradiation was found helpful for plasticity[209]. Different kinds of defects can be introduced by electron damage, which can collapse bulk NaCl into nanocrystals[225,226] . In our experiment, numerous nanocrystals of NaCl formed on the edge and turn the smooth bulk surface to rough after electron beam irradiating the bulk NaCl a few minutes. The heating effect from the beam may also can help

improve the ductility of the nanowire. To not let the beam affect the ductility too much, we performed the same experiments again without beam irradiation. After

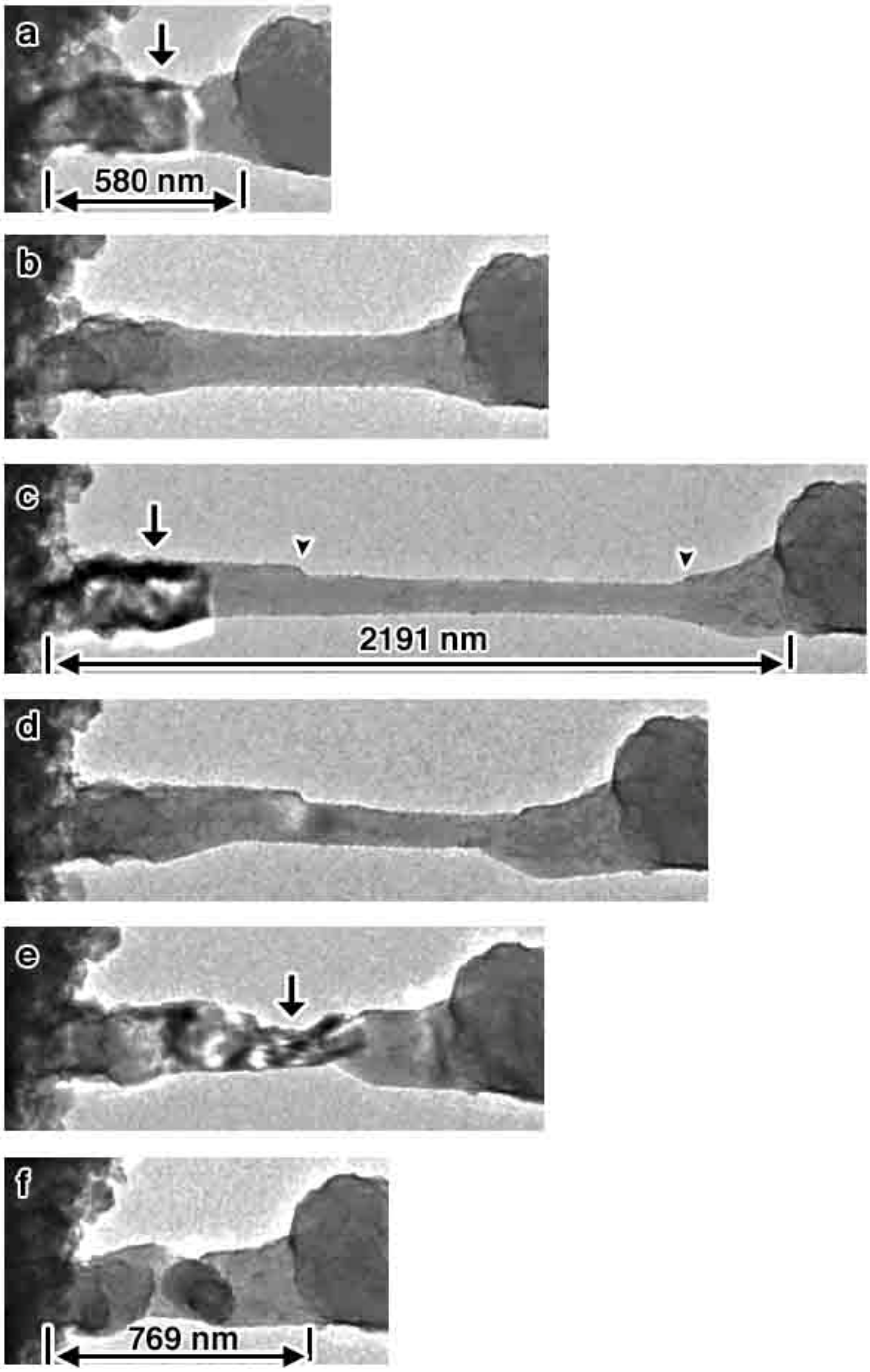

Figure 7.1: (a)-(c) A nanowire was super elongated with a strain rate of 5.5×10^{-3} s^{-1}. (c)-(f) Compress the nanowire with a strain rate of 2.4×10^{-3} s^{-1}. The arrows marked the contrast change induced by crystallization[209].

nanowire and then kept straining it. To take the images, in every ~5 min we only move the beam back and stay on the nanowire for only ~1 s intermittently. Even with no beam condition, the nanowire can still be super elongated (Fig. 7.2). The nanowire was elongated to ~440 nm (Figure 7.2b) from ~210 nm (Figure 7.2a), thus the calculated elongation is around 110%. During the elongation, the crystalline contrast can still be observed[209]. The center of the nanowire will neck down when it is closed to failure. The necking is a typical feature of plastic deformation[209].

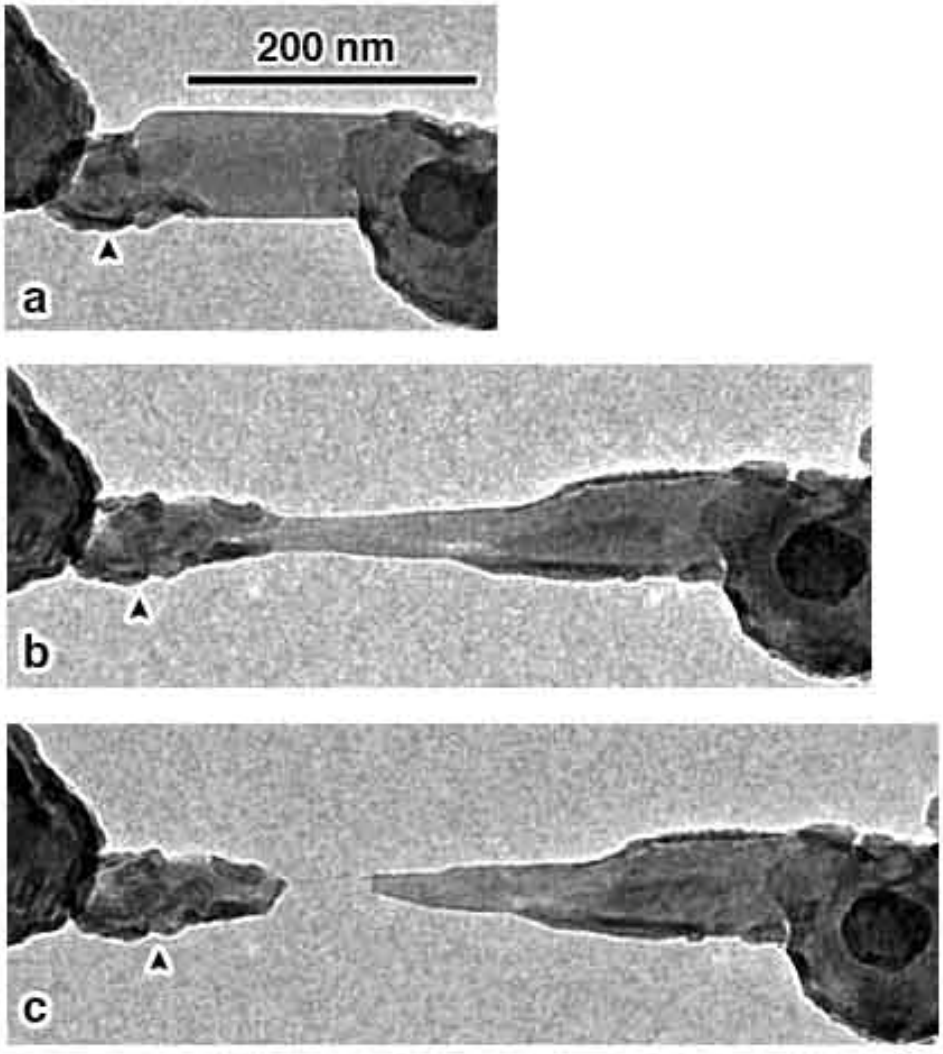

Figure 7.2: A nanowire was super elongated with a strain rate of 2.6×10^{-3} under no beam condition when it is pulled[209].

To check change of the composition, we performed electron energy loss spectroscopy (EELS) characterization on the nanowire before and after superelongation[209]. Figure 7.3a and 7.3b show a nanowire before and after pulling with beam condition with final elongation of ~256%. Figure 7.3c show the EELS collecting area. Fig 7.3d and Fig 7.3e are the EELS spectras of Na-L2,3 edges and Cl L-2,3 edges for the pristine NaCl, the nanowire before pulling and the nanowire after pulling[209]. The energies of different peaks (eV) in the EELS spectras are: a, 9.1; b, 15.3; c, 20.9; d, 32.1; e, 2.8; f, 5.4; g, 11; h, 16.4; i, 21.8; j, 30.6; k, 199.7; l, 208.5; m, 215.7[209]. The Na-L2,3 and Cl-L2,3 edges show clearly in the EELS spectra of the nanowire before and after pulling referring with a standard EELS spectra[227], which means that both Na and Cl exsit in the orginal and elongated nanowire. However as the nanowire elongated, the Cl content keep decreasing. The Cl content in the superelongated nanowires confirmed by Energy dispersive X-ray spectroscopy (EDX) measurement is no more than 10% (Fig. 7.4). And it was found in the Na-L2,3 edge show up more peaks in the nanowires after supereleongation such as peaks e, f, and g in Fig. 7.3d, which was thought resulting from the precipitation of Na induced plasmon oscillation. Because NaCl is quite easy to be decomposed under the higher electron fluxes, using HRTEM to get the atomic image of the NaCl nanowire is not possible. However use similar beam dose to irradiate buck NaCl crystal surface, we can perform HRTEM imaging and found numerous nanocrystals with small grain size <20 nm formed. Using EDX, the structures of these nanocrystals are confirmed still NaCl, however as shown in Fig. 7.4 there has reduction for Cl content (～23%)[209].

A lot of research has revealed that electron beam is quite easy to decompose alkali halides[209,228]. So even under no beam condition, there still have possibility that the low dose electron beam during image capturing have strong effects on plasticity.

The NaCl bond energy is about 8 eV, which is much lower than the NaCl threshold displacement energy ~25 eV (converting to electron energy, it will be more than 350 keV)[209,229]. And irradiated by electron beam, it will form a lot of vacancies and interstitials of the halogen. These point defects can move fast to the surface[226]. Combined with atoms diffusion from bulk NaCl, the vacancies and interstitials may be recovered quickly. This is quite analogous process with that happened in superelongated carbon nanotubes[39]. Together with lots of point defects, the declining of Cl- will also possibly make grain smaller, which may enhance the unexpected plasticity of NaCl nanowire[209]. For instance, it has been reported that some ceramics

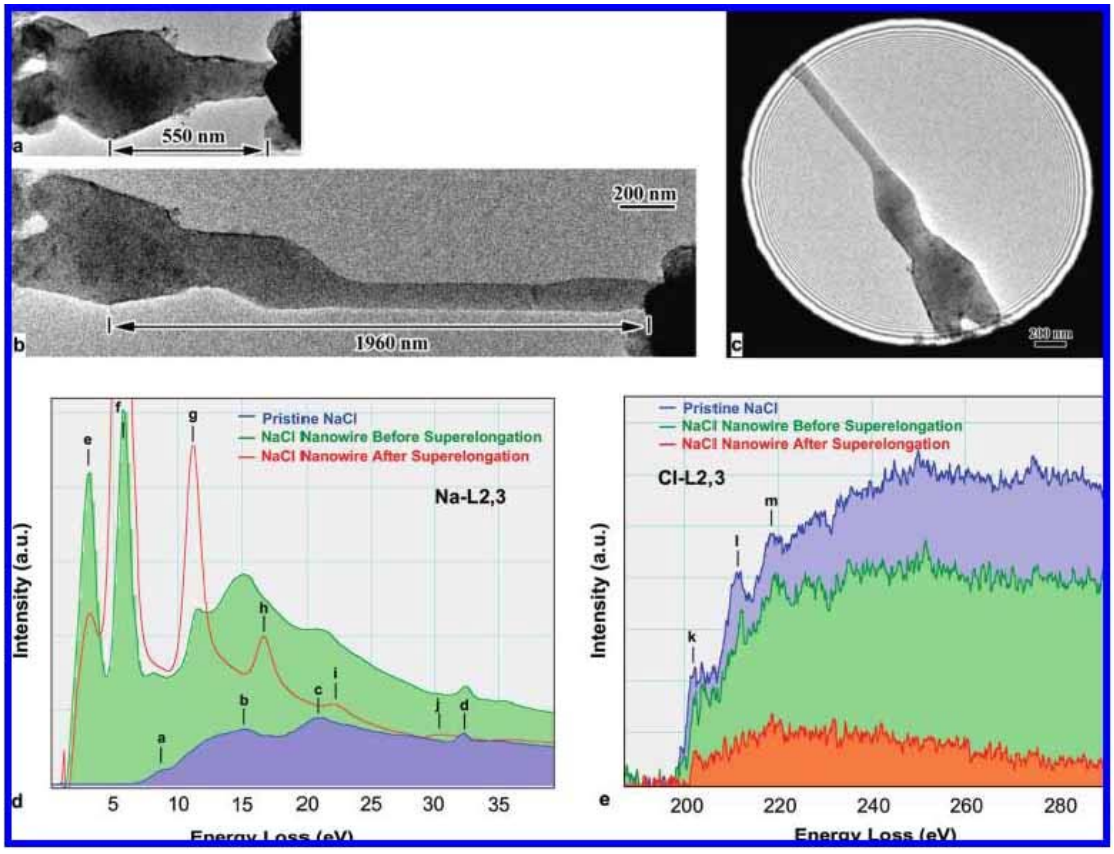

Figure 7.3: (a), (b) TEM images of a nanowire before and after superelongation. (c) The position to do the EELS measurment. (d), (e) EELS spectra of the Na-L2,3 edge and Cl L2,3 edge[209].

can change from brittle to ductile if decreasing the grain size to a few nanometers, because of the enhanced grain boundary atoms diffusion[230]. The enhanced ductility may also possible get help from the precipitation of metallic Na. Although the bond energy of Na-Na 0.76 eV is significantly lower than the bond energy of Na-Cl~8 eV, it is not constrained stoichiometrically for Na-Na bonds, and the conductivity of them will possible help the charging dissipating of electron beam[209].

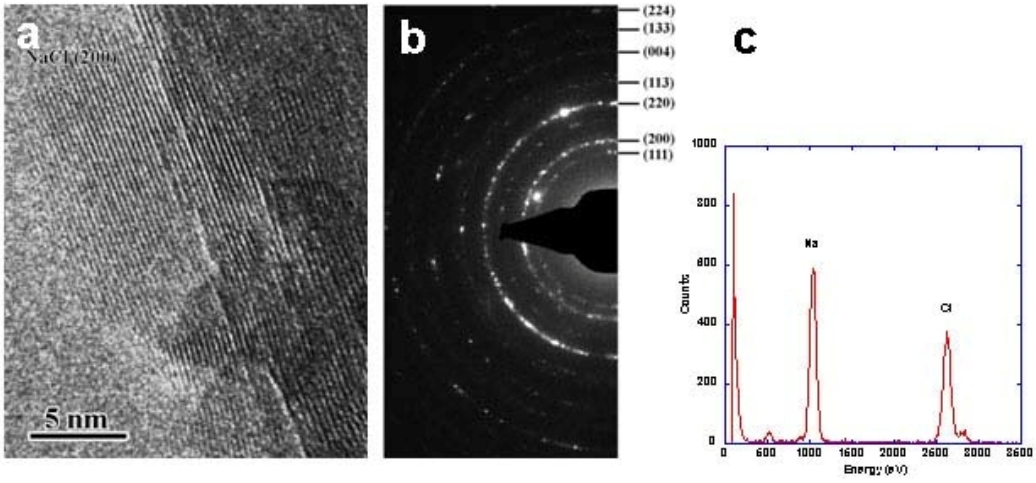

Figure 7.4: (a) Lattice image of the nanocrystals in NaCl. (b) A lot of nanocrystals on the NaCl surfarce are clearly shown in the SAD patter (c) EDX spectrum shows there are only 65% Na and 35% Cl in NaCl nanocrystals[209].

7.4 CONCLUSIONS

In summary, superplastic nanowires formation by retracting a sharp probe on common salt surface was demonstrated by in situ TEM experiments[209]. The superplasticity was resulted by a number of factors including the small cross section area, fast diffusion of atoms, quite small grain size of nanocrystals, and precipitation of Na. it is indicated from these results that formation of nanowires is possible

happened during colliding of sea salt aerosols or gliding of rock salt. These discoveries may make it clear on the underground sediments flow, lithification, and numerous atmospheric reactions[216-219,231]. It is a notable and surprising example that common salt can change from brittle to superplastic to demonstrating that decreasing material size to nanoscale can exceedingly alter its physical properties[209].

8.0 SUMMARY AND CONCLUSIONS

In summary, the mechanical behavior of a 33 nm silver nanowire has been in-situ explored in HRTEM under low local strain rate. Not like the plasticity of most crystalline structures are generally controlled by the dislocation nucleation and multiplication[232], the silver nanowire plastic deformation is mainly contributed to stacking faults formation inside the nanowire. By in-situ HRTEM observation, we found the stacking faults are not induced by Shockley partial dislocations movement, but by the Frank loops formation and expansion. Vacancies nucleated inside the silver nanowire migrated and coalesced to form microscopic clusters. Further, a vacancy Frank loop can be formed from the vacancy cluster by absorbing more vacancies. The density of Frank loops increased during the deformation process and induced more stacking faults, which changes the local stacking sequence, resulting a "necking" like morphology for the fcc part.

Assisted by beam, the silica glass nanowires can turn ductile, and even superplastic in very large size. The ductility of silica nanowires comes from the beam damages enhanced bond switching process. Beam blanked more than 2 minutes will partially recover the beam damage and change the mechanical response to brittle for nanowire bigger than 20 nm. However, the unrecovered beam damages are large enough to trigger the brittle to ductile transition in silica nanowire with size reduction to below 20 nm. The ductility, high strength (close to the theoretical strength) and high elastic-strain limit can prompt a wide range of applications for nanoscale glass

structures[172]. The beam enhanced extreme ductility may also be used for a specific purpose such as manufacturing the optical nanofibers[150].

Quite difference with the bulk metallic glasses which show disastrous tensile failure, nanosized metallic glass exhibits extreme ductility with uniform elongation[173]. After the superelongation, the area reduction can reach 100% in the necking region. However, shear bands were not found during the whole deformation process and is not the reason to cause the excellent tensile plasticity. These findings can be used to improve the understanding on various metallic glasses systems with their mechanical properties, deformation behavior, and fracture mechanisms. And it can indicate us a potential direction to design metallic glass materials with excellent performance in engineering fields[173].

Superplastic nanowires formation by retracting a sharp probe on common salt surface was demonstrated by in situ TEM experiments[209]. The superplasticity was resulted by a number of factors including the small cross section area, fast diffusion of atoms, quite small grain size of nanocrystals, and precipitation of Na. it is indicated from these results that formation of nanowires is possible happened during colliding of sea salt aerosols or gliding of rock salt. These discoveries may make it clear on the underground sediments flow, lithification, and numerous atmospheric reactions[216-219,231]. It is a notable and surprising example that common salt can change from brittle to superplastic to demonstrating that decreasing material size to nanoscale can exceedingly alter its physical properties[209].

APPENDIX

MOLECULAR DYNAMICS SIMULATION ON SILICA NANOWIRES

Erik Bitzek, Ju Li*
Department of Materials Science and Engineering, University of Pennsylvania,
Philadelphia PA 19104, USA
* *E-mail: liju@seas.upenn.edu*

A.1 Methods

Molecular dynamics simulations of uniaxial tensile deformation at a constant strain rate of 10^9 s^{-1} at 300K were performed on two amorphous silica samples: a nano ligament of a diameter d=4.5 nm and a length l=11nm with periodic boundary conditions along the ligament axis, and a rectangular sample of dimensions 5.5x5.5x11 nm^3 under periodic boundary conditions in all directions. Two interaction potentials were used: the original silica three-body potential by Vashishta et al.[233] cut off, shifted and smoothed at r_c=0.8 nm according to the procedure detailed in ref. **234**, and the two-body potential by van Beest, Kramer and van Santen (BKS)[235] which was cut off and shifted at r_c=1.5 nm using a smooth cut-off function.

The bulk sample was constructed from a crystobalite crystal following the stepwise cooling procedure laid out in ref. **236** while maintaining 0 MPa pressure, following an energy minimization and subsequent equilibration at 300K, again at 0

MPa pressure. With the Vashishta potential, the so obtained sample has a density of ρ=2.42 (2.2) g/cm^3 and 0K elastic constants (experimental values from[237] in brackets): Youngs modulus E=109 (73-74) GPa, shear modulus G=44 (31) GPa, and bulk modulus B=61 (31-38) GPa, leading to Poisson's ratio of ν=0.21(0.17-0.18). The BKS sample has the following properties: ρ=2.38 (2.2) g/cm^3, E=71 (73-74) GPa, G=31.7 (31) GPa, B=36.6 (31-38) GPa. With these values the Poisson ratio can be calculated to ν=0.16 (0.17-0.18).

From the relaxed sample the nano ligament was cut out, taking care that the overall charge neutrality was maintained. It is important to note that as the nano ligament was created from the bulk sample, the inside of the nano ligament shares the same micro structure as the bulk sample, and both samples were free of apparent flaws. The nano ligament was again relaxed and equilibrated at 300 K. MD simulations were carried out using the DLPOLY package[238] using the Berendsen thermostat with a time step of 1 fs and the smoothed particle mesh Ewald method for calculating the coulombic interactions (real space cut-off 1.05 nm and accuracy of 10^{-6}). In the bulk simulations, the length of the box vectors orthogonal to the tensile direction is controlled by the Berendsen barostat to maintain uniaxial stress conditions.

The number of atoms with lost, switched or gained bonds determined the bonding topology between the actual configuration and the reference configuration at zero strain. Each atom is identified by its unique number ID. Atoms are considered to have lost bonds when their coordination number z (the number of atoms within the nearest neighbor shell of radius r=0.2016 nm) has decreased with respect to the reference configuration. Atoms which gain a bond show respectively an increase of z.

Atoms with switched bonds have the same z as in the reference configuration, however, at least one nearest neighbor has a different ID than in the reference configuration.

A.2 Results

The stress – strain response of the wire and the PBC sample are shown in Figure 9.1a. The wire shows an earlier deviation from the elastic slope and lower stress levels compared to the PBC sample. After a plastic region (between about 10 and 15% strain) the PBC sample abruptly failed by cleavage (see Figure 9.2), whereas the wire shows a large drop in the stress but is not fully fractured and still can sustain the maximum plastic strain of 20% (Figure 9.1a and 9.1b). Analysis of the atomic configurations shows a connecting ligament was formed during the fracture process of the wire (Figure 9.1b).

As a general observation – which is not limited to glasses - we hypothesize that (a) plastic flow is caused by "bond switching" (S) events, whereas (b) damage and failure are caused by irreversible "bond loss" (L) events in materials. Our central hypothesis is that the ratio of these atomic-level S/L events directly correlates with the observed sample-scale ductility. We note that the accumulation of damage due to a net loss of bonds is a generalization of the classic Griffith concept of surface creation. The S/L statistics from MD simulations are shown as function of strain in Figure 9.1a, and in the colour code of the atoms in Figure 9.1b and 9.1c. From this analysis it becomes evident that plastic deformation by bond switching (S) and damage accumulation by bond loss (L) takes place already during the "elastic" part in the stress-strain curve, see Figure 9.1a. Furthermore, pre-existing free surfaces are seen to promote plasticity: S/L is about 1 : 2–2.5 for the wire compared to 1 : 2.5–4 in

the case without surfaces. From this and other examples (see Supplementary Materials) it becomes clear that the S/L statistics indeed controls ductility. Figure 9.1c shows that the atoms involved in the plastic deformation are mostly situated close to the surface of the wire. All of the plastic deformation in SiO_2 involves bond-switching and thus changes in the bonding topology. In contrast, damage and irreversible bond loss in silica entails the net creation of under-coordinated atoms and free volume. Their local accumulation leads to the nucleation of internal surfaces like cavities or crack-nuclei. Bond switching processes (as shown in Figure 9.1d), which are characterized by correlated bond breaking and subsequent bond formation, on the other hand do not induce a net increase of under-coordinated atoms. They do, however, as we observe in both the BKS- and the Vashishta-potential, require the existence of under- or over-coordinated atoms (coordination defects), such as non-bridging oxygens[239]. The influence of the surface on the plastic deformation is thus twofold: first, the missing bonding constraints at the surface lead to an increased flexibility of the partly un-bonded silica tetrahedra (as seen e.g. in the rotation of a tetrahedron in Fig. 9.3d). These can rotate and thereby bring e.g. their non-bridging oxygen close to under-coordinated silicon atoms. Secondly, the presence of under-coordinated atoms at the surface catalyses bond switching and thus plastic deformation. In the course of deformation these defects can migrate by bond-switching processes inside the wire.

Based on this general reasoning, one can assume that the existence of a surface will lead to a region of enhanced plasticity beneath it. Due to the high strain rate in the simulations the thickness of this surface-plasticized region in the MD simulation cannot be expected to be directly compared to the experimental situation[72]. The experiments (Figure 5.3) suggest however a thickness of the plasticized layer of about

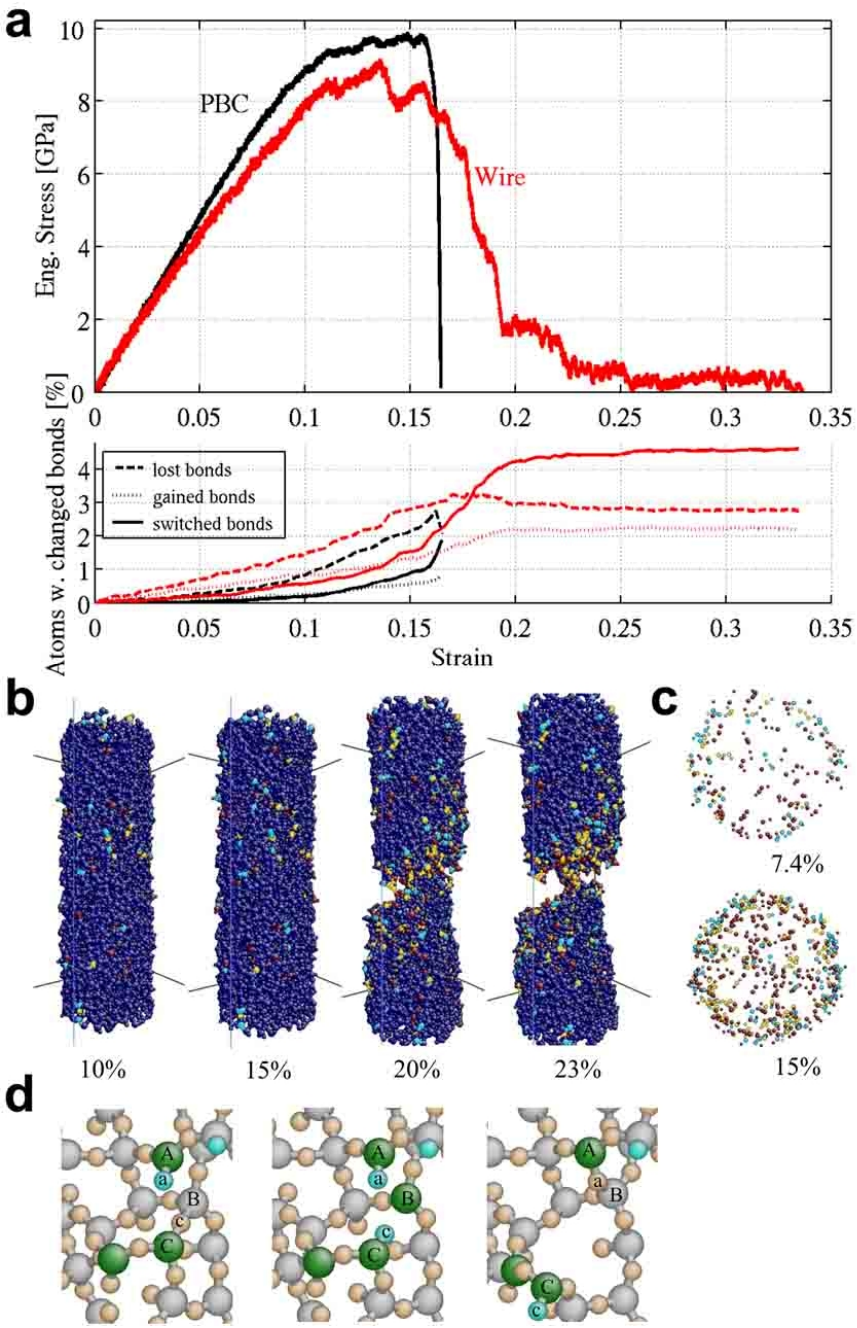

Figure 9.1: Molecular dynamics simulations of the tensile behaviour of silica glass (Vashishta potential). (a) Stress-strain responses of the wire and the PBC sample together with the bond-switching statistics. (b) Snapshots of the wire at different strains (blue atoms have no change in bonding topology, cyan atoms have gained bonding partners, yellow atoms have switched bonds, red atoms have lost bonds). (c) Top view of the wire, showing only atoms with changes in bonding topology (same colour code as in (b)). (d) An example of a bond-switching process involving the migration of non-bridging O-defect and the rotation of a partially unbonded silica tetrahedron (around C) (colour coding according to the coordination number).

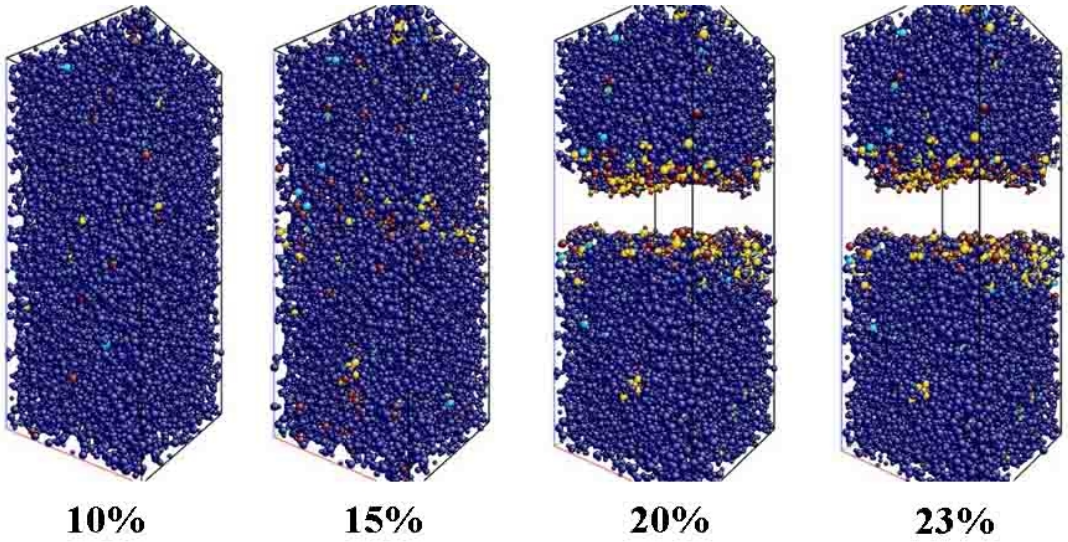

Figure 9.2: Snapshots from the bulk Vashishta sample at different strains. The atoms are colored according to the to changes of their bonding topology: dark blue atoms have exactly the same neighbors as in the strain free initial configuration, light blue atoms have gained a bond, yellow atoms have switched bonding partners while maintaining the same coordination number, red corresponds to broken bonds.

8–10 nm (about 10 ring diameters). In this region of enhanced plasticity flaws can be somewhat blunted, and once the surface affected region spans the wire it can deform plastically, as shown in Figure 5.2.

The existence of surface-plasticized layer 8–10 nm thick in silica glass may also resolve the puzzle why the fracture seems to proceed by the nucleation and coalescence of cavities when monitored at the intersection of the crack tip front with a macroscopic free surface[240,241], whereas analysis of fractography inside the sample does not reveal any signs of ductility[242.]

It is clear that the failure behaviour in the simulation of silica glass depends strongly on the interaction potential. We therefore performed simulations with the three-body potential of Vashishta et al.[233] and the two-body potential by van Best,

Kramer and van Santen (BKS)[235]. It is important to note that both potentials lead to different defect structures in the unstrained glass samples. In particular, the BKS potential allows for the existence of over-coordinated atoms, which are not observed in the Vashishta samples. As can be seen from the stress-strain curves in Figure 9.3 and the snapshots in Figure 9.4, with the BKS potential, both the wire and the bulk sample deform in a ductile fashion. It is interesting to note that by suppressing the stress relaxation orthogonal to the tensile axis leads to brittle fracture of the PBC sample. However, these boundary conditions, also frequently used in MD simulations of glass fracture, do not represent the situation in experimental (uniaxial) tensile tests. From the bond switching (S) and loss (L) statistics (Figure 9.3) one sees clearly that more atoms are switching bonding partner than losing bonds. The S/L statistics during deformation can be thus used to characterize the ductility or brittleness of a given interaction potential.

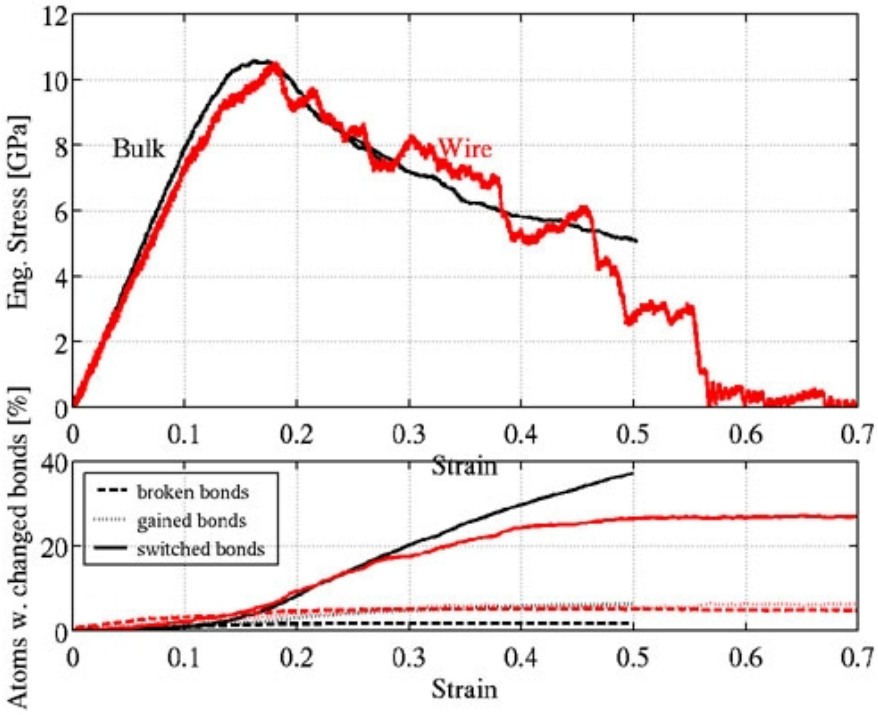

Figure 9.3: Stress-Strain response for the BKS sample together with the bond-change statistics.

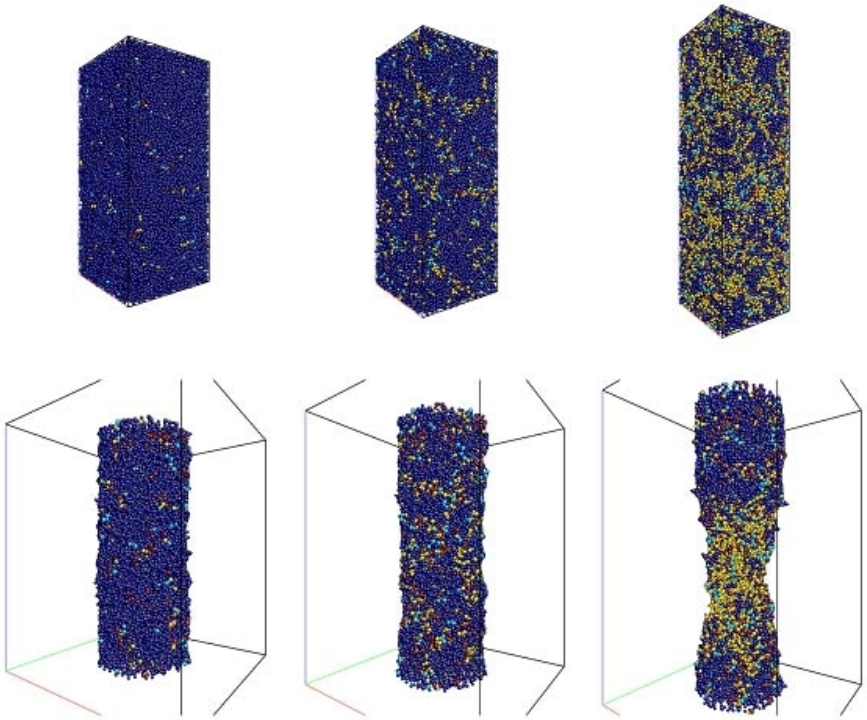

Figure 9.4: Snapshots of the simulations with the BKS Potential at strains of 10, 20, and 40%. See Figure 9.2 for the colour code of the atoms.

BIBILOGRAPHY

[1]. Ng, D.K.T., Tan, L.S., & Hong, M.H., Synthesis of GaN nanowires on gold-coated substrates by pulsed laser ablation. *Current Applied Physics* 6 (3), 403-406 (2006).

[2]. Cui, Y., Duan, X., Huang, Y., & Lieber, C.M., *in Nanowires and Nanobelts: Materials, Properties and Devices I*. (Kluwer Academic, Boston, MA 2003).

[3]. Lieber, C.M., Nanoscale Science and Technology: Building a Big Future from Small Things. *MRS Bull.* 28, 486 (2003).

[4]. Li, Y., Qian, F., Xiang, J., & Lieber, C.M., Nanowire electronic and optoelectronic devices. *Materials Today* 9 (10), 18-27 (2006).

[5]. Zeng, H. *et al.*, Magnetic properties of self-assembled Co nanowires of varying length and diameter. *J. Appl. Phys.* 87, 4718-4720 (2000).

[6]. Wang, H., Xu, C., Cheng, F., & Jiang, S., Pd nanowire arrays as electrocatalysts for ethanol electrooxidation. *Electrochemistry Communications* 9 (5), 1212-1216 (2007).

[7]. Wu, B., Heidelberg, A., & Boland, J.J., Mechanical properties of ultrahigh-strength gold nanowires. *Nat Mater* 4 (7), 525-529 (2005).

[8]. Cui, Y. & Lieber, C.M., Functional Nanoscale Electronic Devices Assembled Using Silicon Nanowire Building Blocks. *Science* 291 (5505), 851-853 (2001).

[9]. Zheng, G., Lu, W., Jin, S., & Lieber, C.M., Synthesis and Fabrication of High-Performance n-Type Silicon Nanowire Transistors. *Advanced Materials* 16 (21), 1890-1893 (2004).

[10]. Husain, A. *et al.*, Nanowire-based very-high-frequency electromechanical resonator. *Applied Physics Letters* 83 (6), 1240-1242 (2003).

[11]. Feng, X.L., He, R., Yang, P., & Roukes, M.L., Very High Frequency Silicon Nanowire Electromechanical Resonators. *Nano Letters* 7 (7), 1953-1959 (2007).

[12]. Zheng, G., Patolsky, F., Cui, Y., Wang, W.U., & Lieber, C.M., Multiplexed electrical detection of cancer markers with nanowire sensor arrays. *Nat Biotech* 23 (10), 1294-1301 (2005).

[13]. Liu, H., Kameoka, J., Czaplewski, D.A., & Craighead, H.G., Polymeric Nanowire Chemical Sensor. *Nano Letters* 4 (4), 671-675 (2004).

[14]. Rao, C.N.R., Deepak, F.L., Gundiah, G., & Govindaraj, A., Inorganic nanowires. *Progress in Solid State Chemistry* 31 (1-2), 5-147 (2003).

[15]. Diao, J., Gall, K., & Dunn, M.L., Surface-stress-induced phase transformation in metal nanowires. *Nat Mater* 2 (10), 656-660 (2003).

[16]. Gall, K. *et al.*, Tetragonal Phase Transformation in Gold Nanowires. *Journal of Engineering Materials and Technology* 127 (4), 417-422 (2005).

[17]. Kondo, Y. & Takayanagi, K., Gold Nanobridge Stabilized by Surface Structure. *Physical Review Letters* 79 (18), 3455 (1997).

[18]. Ohnishi, H., Kondo, Y., & Takayanagi, K., Quantized conductance through individual rows of suspended gold atoms. *Nature* 395 (6704), 780-783 (1998).

[19]. BettiniJ *et al.*, Experimental realization of suspended atomic chains composed of different atomic species. *Nat Nano* 1 (3), 182-185 (2006).

[20]. Liang, W., Zhou, M., & Ke, F., Shape Memory Effect in Cu Nanowires. *Nano Letters* 5 (10), 2039-2043 (2005).

[21]. Park, H.S., Gall, K., & Zimmerman, J.A., Shape Memory and Pseudoelasticity in Metal Nanowires. *Physical Review Letters* 95 (25), 255504 (2005).

[22]. Liang, W. & Zhou, M., Pseudoelasticity of Single Crystalline Cu Nanowires Through Reversible Lattice Reorientations. *Journal of Engineering Materials and Technology* 127 (4), 423-433 (2005).

[23]. Branicio, P.S. & Rino, J.P., Large deformation and amorphization of Ni nanowires under uniaxial strain: A molecular dynamics study. *Physical Review B* 62 (24), 16950 (2000).

[24]. Ikeda, H. *et al.*, Strain Rate Induced Amorphization in Metallic Nanowires. *Physical Review Letters* 82 (14), 2900 (1999).

[25]. Hyde, B., Espinosa, H., & Farkas, D., An atomistic investigation of elastic and plastic properties of Au nanowires. *JOM Journal of the Minerals, Metals and Materials Society* 57 (9), 62-66 (2005).

[26]. Koizumi, H., Oshima, Y., Kondo, Y., & Takayanagi, K., Quantitative high-resolution microscopy on a suspended chain of gold atoms. *Ultramicroscopy* 88 (1), 17-24 (2001).

[27]. Heidelberg, A. *et al.*, A Generalized Description of the Elastic Properties of Nanowires. *Nano Letters* 6 (6), 1101-1106 (2006).

[28]. Zhu, Y., Xu, F., Qin, Q., Fung, W.Y., & Lu, W., Mechanical Properties of Vapor-Liquid-Solid Synthesized Silicon Nanowires. *Nano Letters* (2009).

[29]. Richter, G. *et al.*, Ultrahigh Strength Single Crystalline Nanowhiskers Grown by Physical Vapor Deposition. *Nano Letters* 9 (8), 3048-3052 (2009).

[30]. Rubio-Bollinger, G., Bahn, S.R., Agrait, N., Jacobsen, K.W., & Vieira, S., Mechanical Properties and Formation Mechanisms of a Wire of Single Gold Atoms. *Physical Review Letters* 87 (2), 026101 (2001).

[31]. Cao, A.J., Wei, Y.G., & Mao, S.X., Deformation mechanisms of face-centered-cubic metal nanowires with twin boundaries. *Applied Physics Letters* 90 (15), 151909-151903 (2007).

[32]. Koh, S.J.A. & Lee, H.P., Molecular dynamics simulation of size and strain rate dependent mechanical response of FCC metallic nanowires. *Nanotechnology* 17 (14), 3451-3467 (2006).

[33]. Wang, D. *et al.*, Where, and How, Does a Nanowire Break? *Nano Letters* 7 (5), 1208-1212 (2007).

[34]. Sorensen, M.R., Brandbyge, M., & Jacobsen, K.W., Mechanical deformation of atomic-scale metallic contacts: Structure and mechanisms. *Physical Review B* 57 (6), 3283 (1998).

[35]. Diao, J., Gall, K., Dunn, M.L., & Zimmerman, J.A., Atomistic simulations of the yielding of gold nanowires. *Acta Materialia* 54 (3), 643-653 (2006).

[36]. Kang, J.-W. & Hwang, H.-J., Mechanical deformation study of copper nanowire using atomistic simulation. *Nanotechnology* 12 (3), 295-300 (2001).

[37]. Dao-Long, C. & Tei-Chen, C., Mechanical properties of Au nanowires under uniaxial tension with high strain-rate by molecular dynamics. *Nanotechnology* 16 (12), 2972 (2005).

[38]. Kumar, K.S., Van Swygenhoven, H., & Suresh, S., Mechanical behavior of nanocrystalline metals and alloys. *Acta Materialia* 51 (19), 5743-5774 (2003).

[39]. Huang, J.Y. *et al.*, Superplastic carbon nanotubes. *Nature* 439 (7074), 281-281 (2006).

[40]. Huang, J.Y. *et al.*, Kink Formation and Motion in Carbon Nanotubes at High Temperatures. *Physical Review Letters* 97 (7), 075501-075504 (2006).

[41]. Huang, J.Y. *et al.*, Enhanced Ductile Behavior of Tensile-Elongated Individual Double-Walled and Triple-Walled Carbon Nanotubes at High Temperatures. *Physical Review Letters* 98 (18), 185501-185504 (2007).

[42]. Fisher, J.C. & Hollomon, J.H., Symposium: Effect of Multiaxial Stresses on Metals - A Statistical Theory of Fracture in *AIME Transactions* (1947), pp. 2218-2233.

[43]. Ng, K.S. & Ngan, A.H.W., Small Scale Plasticity - an ad hoc Review. *IOP Conference Series: Materials Science and Engineering* 4 (1), 012002 (2009).

[44]. Brenner, S.S., Tensile Strength of Whiskers. *Journal of Applied Physics* 27 (12), 1484-1491 (1956).

[45]. Von Blanckenhagen, B., Gumbsch, P., & Arzt, E., Dislocation sources and the flow stress of polycrystalline thin metal films. *Philos. Mag. Lett.* 83, 1-8 (2003).

[46]. Uchic, M.D., Dimiduk, D.M., Florando, J.N., & Nix, W.D., Sample Dimensions Influence Strength and Crystal Plasticity. *Science* 305 (5686), 986-989 (2004).

[47]. Julia, R.G., Warren, C.O., & William, D.N., Size dependence of mechanical properties of gold at the micron scale in the absence of strain gradients. 53 (6), 1821-1830 (2005).

[48]. Zhu, T.T., Bushby, A.J., & Dunstan, D.J., Materials mechanical size effects: a review. *Materials Technology: Advanced Performance Materials* 23, 193-209 (2008).

[49]. Greer, J.R., Oliver, W.C., & Nix, W.D., Size dependence of mechanical properties of gold at the micron scale in the absence of strain gradients. *Acta Materialia* 53 (6), 1821-1830 (2005).

[50]. Greer, J.R. & Nix, W.D., Nanoscale gold pillars strengthened through dislocation starvation. *Physical Review B (Condensed Matter and Materials Physics)* 73 (24), 245410-245416 (2006).

[51]. Eshelby, J.D., Screw Dislocations in Thin Rods. *Journal of Applied Physics* 24 (2), 176-179 (1953).

[52]. Agrawal, R. & Espinosa, H.D., Multiscale Experiments: State of the Art and Remaining Challenges. *Journal of Engineering Materials and Technology* 131 (4), 041208-041215 (2009).

[53]. Shan, Z.W., Mishra, R.K., Syed Asif, S.A., Warren, O.L., & Minor, A.M., Mechanical annealing and source-limited deformation in submicrometre-diameter Ni crystals. *Nat Mater* 7 (2), 115-119 (2008).

[54]. Sieradzki, K., Rinaldi, A., Friesen, C., & Peralta, P., Length scales in crystal plasticity. *Acta Materialia* 54 (17), 4533-4538 (2006).

[55]. Cammarata, R.C. & Sieradzki, K., Surface and Interface Stresses. *Annual Review of Materials Science* 24 (1), 215-234 (2003).

[56]. Marszalek, P.E., Greenleaf, W.J., Li, H., Oberhauser, A.F., & Fernandez, J.M., Atomic force microscopy captures quantized plastic deformation in gold nanowires. *Proceedings of the National Academy of Sciences of the United States of America* 97 (12), 6282-6286 (2000).

[57]. Diao, J., Gall, K., & Dunn, M.L., Yield Strength Asymmetry in Metal Nanowires. *Nano Letters* 4 (10), 1863-1867 (2004).

[58]. Ji, C., Ph.D. dissertation, Vanderbilt University, 2007.

[59]. Park, H.S., Klein, P.A., & Wagner, G.J., A surface Cauchy-Born model for nanoscale materials. *International Journal for Numerical Methods in Engineering* 68 (10), 1072-1095 (2006).

[60]. Diao, J., Gall, K., & Dunn, M.L., Surface stress driven reorientation of gold nanowires. *Physical Review B* 70 (7), 075413 (2004).

[61]. Park, H.S. & Ji, C., On the thermomechanical deformation of silver shape memory nanowires. *Acta Materialia* 54 (10), 2645-2654 (2006).

[62]. Liang, W. & Zhou, M., Atomistic simulations reveal shape memory of fcc metal nanowires. *Physical Review B (Condensed Matter and Materials Physics)* 73 (11), 115409-115411 (2006).

[63]. Cao, A. & Wei, Y., Atomistic simulations of the mechanical behavior of fivefold twinned nanowires. *Physical Review B (Condensed Matter and Materials Physics)* 74 (21), 214108-214107 (2006).

[64]. Haftel, M.I. & Gall, K., Density functional theory investigation of surface-stress-induced phase transformations in fcc metal nanowires. *Physical Review B (Condensed Matter and Materials Physics)* 74 (3), 035420-035412 (2006).

[65]. Streitz, F.H., Cammarata, R.C., & Sieradzki, K., Surface-stress effects on elastic properties. I. Thin metal films. *Physical Review B* 49 (15), 10699 (1994).

[66]. Lee, B. & Rudd, R.E., First-principles calculation of mechanical properties of Si<001> nanowires and comparison to nanomechanical theory. *Physical Review B (Condensed Matter and Materials Physics)* 75 (19), 195328-195313 (2007).

[67]. Li, X., Ono, T., Wang, Y., & Esashi, M., Ultrathin single-crystalline-silicon cantilever resonators: Fabrication technology and significant specimen size effect on Young's modulus. *Applied Physics Letters* 83 (15), 3081-3083 (2003).

[68]. Kizuka, T., Takatani, Y., Asaka, K., & Yoshizaki, R., Measurements of the atomistic mechanics of single crystalline silicon wires of nanometer width. *Physical Review B* 72 (3), 035333 (2005).

[69]. Han, X.D. *et al.*, Low-Temperature In Situ Large-Strain Plasticity of Silicon Nanowires. *Advanced Materials* 19 (16), 2112-2118 (2007).

[70]. Jing, G.Y. *et al.*, Surface effects on elastic properties of silver nanowires: Contact atomic-force microscopy. *Physical Review B (Condensed Matter and Materials Physics)* 73 (23), 235409-235406 (2006).

[71]. Cuenot, S., Fretigny, C., Demoustier-Champagne, S., & Nysten, B., Surface tension effect on the mechanical properties of nanomaterials measured by atomic force microscopy. *Physical Review B* 69 (16), 165410 (2004).

[72]. Zhu, T., Li, J., Samanta, A., Leach, A., & Gall, K., Temperature and Strain-Rate Dependence of Surface Dislocation Nucleation. *Physical Review Letters* 100 (2), 025502-025504 (2008).

[73]. Frank, F.C. & Read, W.T., Multiplication Processes for Slow Moving Dislocations. *Physical Review* 79 (4), 722 (1950).

[74]. Mason, J.K., Lund, A.C., & Schuh, C.A., Determining the activation energy and volume for the onset of plasticity during nanoindentation. *Physical Review B (Condensed Matter and Materials Physics)* 73 (5), 054102-054114 (2006).

[75]. Ngan, A.H.W., Zuo, L., & Wo, P.C., Size dependence and stochastic nature of yield strength of micron-sized crystals: a case study on Ni3Al. *Proceedings of the Royal Society A: Mathematical, Physical and Engineering Science* 462 (2070), 1661-1681 (2006).

[76]. Volkert, C.A., Lilleodden, E.T., Kramer, D., & Weissmuller, J., Approaching the theoretical strength in nanoporous Au. *Applied Physics Letters* 89 (6), 061920-061923 (2006).

[77]. Dimiduk, D.M., Uchic, M.D., & Parthasarathy, T.A., Size-affected single-slip behavior of pure nickel microcrystals. *Acta Materialia* 53 (15), 4065-4077 (2005).

[78]. KOTAKE, #160, & S., *Molecular mechanical engineering*. (Japan Society of Mechanical Engineers, Tokyo, JAPON, 1995).

[79]. Ji, C. & Park, H.S., The Effect of Defects on the Mechanical Behavior of Silver Shape Memory Nanowires. *Journal of Computational and Theoretical Nanoscience* 4, 578-587 (2007).

[80]. Sutrakar, V.K. & Mahapatra, D.R., Coupled effect of size, strain rate, and temperature on the shape memory of a pentagonal Cu nanowire. *Nanotechnology* 20 (4), 045701 (2009).

[81]. Lao, J. & Moldovan, D., Surface stress induced structural transformations and pseudoelastic effects in palladium nanowires. *Applied Physics Letters* 93 (9), 093108-093103 (2008).

[82]. Guo, X., Liang, W., & Zhou, M., Mechanism for the Pseudoelastic Behavior of FCC Shape Memory Nanowires. *Experimental Mechanics* 49 (2), 183-190 (2009).

[83]. Mehrez, H. & Ciraci, S., Yielding and fracture mechanisms of nanowires. *Physical Review B* 56 (19), 12632 (1997).

[84]. Wen, Y.-H., Zhu, Z.-Z., Shao, G.-F., & Zhu, R.-Z., The uniaxial tensile deformation of Ni nanowire: atomic-scale computer simulations. *Physica E: Low-dimensional Systems and Nanostructures* 27 (1-2), 113-120 (2005).

[85]. Wen, Y.-H., Zhu, Z.-Z., & Zhu, R.-Z., Molecular dynamics study of the mechanical behavior of nickel nanowire: Strain rate effects. *Computational Materials Science* 41 (4), 553-560 (2008).

[86]. Garcia-Mochales, P., Paredes, R., Pelaez, S., & Serena, P.A., Statistical analysis of the breaking processes of Ni nanowires. *Nanotechnology* 19 (22), 225704 (2008).

[87]. Hakkinen, H., Barnett, R.N., Scherbakov, A.G., & Landman, U., Nanowire Gold Chains: Formation Mechanisms and Conductance. *The Journal of Physical Chemistry B* 104 (39), 9063-9066 (2000).

[88]. Harold, S.P. & Jonathan, A.Z., Stable nanobridge formation in 〈110〉 gold nanowires under tensile deformation. 54 (6), 1127-1132 (2006).

[89]. da Silva, E.Z., da Silva, A.J.R., & Fazzio, A., How Do Gold Nanowires Break? *Physical Review Letters* 87 (25), 256102 (2001).

[90]. Bahn, S.R. & Jacobsen, K.W., Chain Formation of Metal Atoms. *Physical Review Letters* 87 (26), 266101 (2001).

[91]. Liang, W. & Zhou, M., Response of copper nanowires in dynamic tensile deformation. *Proceedings of the Institution of Mechanical Engineers, Part C: Journal of Mechanical Engineering Science* 218 (6), 599-606 (2004).

[92]. Wang, Z.L. & Song, J., Piezoelectric Nanogenerators Based on Zinc Oxide Nanowire Arrays. *Science* 312 (5771), 242-246 (2006).

[93]. Lin, Y.-F., Song, J., Ding, Y., Lu, S.-Y., & Wang, Z.L., Piezoelectric nanogenerator using CdS nanowires. *Applied Physics Letters* 92 (2), 022105-022103 (2008).

[94]. Gall, K., Diao, J., & Dunn, M.L., The Strength of Gold Nanowires. *Nano Letters* 4 (12), 2431-2436 (2004).

[95]. Liang, H., Upmanyu, M., & Huang, H., Size-dependent elasticity of nanowires: Nonlinear effects. *Physical Review B* 71 (24), 241403 (2005).

[96]. Zhang, Y., Tan, E.P.S., Sow, C.H., & Lim, C.T., Nanomechanical Characterization of One-Dimensional Nanostructures. *Micro and Nano Mechanical Testing of Materials and Devices*, 105 (2008).

[97]. Zhu, Y., Ke, C., & Espinosa, H., Experimental Techniques for the Mechanical Characterization of One-Dimensional Nanostructures. *Experimental Mechanics* 47 (1), 7-24 (2007).

[98]. Zhou, P., Wu, C., & Li, X., Three-point bending Young's modulus of nanowires. *Measurement Science and Technology* 19 (11), 115703 (2008).

[99]. Salvetat, J.P. *et al.*, Mechanical properties of carbon nanotubes. *Applied Physics A: Materials Science & Processing* 69 (3), 255-260 (1999).

[100]. Ni, H., Li, X., & Gao, H., Elastic modulus of amorphous SiO_2 nanowires. *Applied Physics Letters* 88 (4), 043108-043103 (2006).

[101]. Chen, Y. *et al.*, Mechanical elasticity of vapour–liquid–solid grown GaN nanowires. *Nanotechnology* 18 (13), 135708 (2007).

[102]. Timoshenko, S.P. & Gere, J.M., *Mechanics of Materials*. (Van Nostrand Reinhold, New York, 1972).

[103]. Ni, H., Li, X., Cheng, G., & Klie, R., Elastic modulus of single-crystal GaN nanowires. *Journal of materials research* 21, 2882-2887 (2006).

[104]. Ding, Y. *et al.*, The elastic module of Ag nanowires prepared from electrochemical deposition. *Journal of Alloys and Compounds* 474 (1-2), 223-225 (2009).

[105]. Wong, E.W., Sheehan, P.E., & Lieber, C.M., Nanobeam Mechanics: Elasticity, Strength, and Toughness of Nanorods and Nanotubes. *Science* 277 (5334), 1971-1975 (1997).

[106]. Song, J., Wang, X., Riedo, E., & Wang, Z.L., Elastic Property of Vertically Aligned Nanowires. *Nano Letters* 5 (10), 1954-1958 (2005).

[107]. Wu, B. *et al.*, Microstructure-Hardened Silver Nanowires. *Nano Letters* 6 (3), 468-472 (2006).

[108]. Ding, W., Calabri, L., Chen, X., Kohlhaas, K.M., & Ruoff, R.S., Mechanics of crystalline boron nanowires. *Composites Science and Technology* 66 (9), 1112-1124 (2006).

[109]. Han, X., Zhang, Z., & Wang, Z.L., Experimental nanomechanics of one-dimensional nanomaterials by in situ microscopy. *Nano* 2 (05), 249-271 (2007).

[110]. Han, X.D. *et al.*, Low-Temperature in Situ Large Strain Plasticity of Ceramic SiC Nanowires and Its Atomic-Scale Mechanism. *Nano Letters* 7 (2), 452-457 (2006).

[111]. Zheng, K. *et al.*, Atomic Mechanisms Governing the Elastic Limit and the Incipient Plasticity of Bending Si Nanowires. *Nano Letters* 9 (6), 2471-2476 (2009).

[112]. Zhang, Y. *et al.*, Direct Observation of Super-Plasticity of Beta-SiC Nanowires at Low Temperature. *Advanced Functional Materials* 17 (17), 3435-3440 (2007).

[113]. Zhu, Y. & Espinosa, H.D., An Electromechanical Material Testign System for In situ Electron Microscopy and Applications. *Proceedings of the National*

Academy of Sciences of the United States of America 102 (41), 14503-14508 (2005).

[114]. Peng, B., Zhu, Y., Petrov, I., & Espinosa, H.D., A Microelectromechanical System for Nano-Scale Testing of One Dimensional Nanostructures. *Sensor Letters* 6, 76-87 (2008).

[115]. Zhu, Y. & Espinosa, H.D., An electromechanical material testing system for in situ electron microscopy and applications. *Proceedings of the National Academy of Sciences of the United States of America* 102 (41), 14503-14508 (2005).

[116]. Poncharal, P., Wang, Z.L., Ugarte, D., & de Heer, W.A., Electrostatic Deflections and Electromechanical Resonances of Carbon Nanotubes. *Science* 283 (5407), 1513-1516 (1999).

[117]. Zhou, J. *et al.*, Nanowire as pico-gram balance at workplace atmosphere. *Solid State Communications* 139 (5), 222-226 (2006).

[118]. Yu, M.-F., Wagner, G.J., Ruoff, R.S., & Dyer, M.J., Realization of parametric resonances in a nanowire mechanical system with nanomanipulation inside a scanning electron microscope. *Physical Review B* 66 (7), 073406 (2002).

[119]. Dikin, D.A., Chen, X., Ding, W., Wagner, G., & Ruoff, R.S., Resonance vibration of amorphous SiO[sub 2] nanowires driven by mechanical or electrical field excitation. *Journal of Applied Physics* 93 (1), 226-230 (2003).

[120]. Chen, C.Q., Shi, Y., Zhang, Y.S., Zhu, J., & Yan, Y.J., Size Dependence of Young's Modulus in ZnO Nanowires. *Physical Review Letters* 96 (7), 075505-075504 (2006).

[121]. Chen, C., Shi, Y., Zhang, Y., Zhu, J., & Yan, Y., Size Dependence of Young's Modulus in ZnO Nanowires. *Physical review letters* 96 (7), 75505 (2006).

[122]. Li, X., Gao, H., Murphy, C.J., & Caswell, K.K., Nanoindentation of Silver Nanowires. *Nano Letters* 3 (11), 1495-1498 (2003).

[123]. Caswell, K.K., Bender, C.M., & Murphy, C.J., Seedless, Surfactantless Wet Chemical Synthesis of Silver Nanowires. *Nano Letters* 3 (5), 667-669 (2003).

[124]. Tong, L., Lou, J., Ye, Z., Svacha, G.T., & Mazur, E., Self-modulated taper drawing of silica nanowires. *Nanotechnology* 16 (9), 1445-1448 (2005).

[125]. Walker, J.F. & Broom, R.F., Surface damage of semiconductor TEM samples prepared by focused ion beams. *Institute of Physics Conference Series* 157, 473-478 (1997).

[126]. Kato, N.I., Reducing focused ion beam damage to transmission electron microscopy samples. *J Electron Microsc (Tokyo)* 53 (5), 451-458 (2004).

[127]. Langford, R.M., Focused ion beams techniques for nanomaterials characterization. *Microscopy Research and Technique* 69 (7), 538-549 (2006).

[128]. Bei, H., Shim, S., Miller, M.K., Pharr, G.M., & George, E.P., Effects of focused ion beam milling on the nanomechanical behavior of a molybdenum-alloy single crystal. *Applied Physics Letters* 91 (11), 111915-111913 (2007).

[129]. Shim, S., Bei, H., Miller, M.K., Pharr, G.M., & George, E.P., Effects of focused ion beam milling on the compressive behavior of directionally solidified micropillars and the nanoindentation response of an electropolished surface. *Acta Materialia* 57 (2), 503-510 (2009).

[130]. Boisen, A., Thaysen, J., Jensenius, H., & Hansen, O., Environmental sensors based on micromachined cantilevers with integrated read-out. *Ultramicroscopy* 82 (1-4), 11-16 (2000).

[131]. Novgorodova, M.I., Gorshkov, A.I., & Mokhov, A.V., Native silver and its new structural modifications. *Zap. Vses. Mineral. Obshch* 108, 552-563 (1979).

[132]. Taneja, P., Banerjee, R., Ayyub, P., & Dey, G.K., Observation of a hexagonal (4H) phase in nanocrystalline silver. *Physical Review B* 64 (3), 033405 (2001).

[133]. Wetli, E., Hochstrasser, M., & Erbudak, M., Epitaxial growth of Ag in the hexagonal structure. *Surface Science* 377-379, 876-881 (1997).

[134]. Liu, X., Luo, J., & Zhu, J., Size Effect on the Crystal Structure of Silver Nanowires. *Nano Letters* 6 (3), 408-412 (2006).

[135]. Doremus, R.H., *Growth and perfection of crystals: proceedings*. (Wiley, 1958).

[136]. Sastry, S., Ramaswami, B., & Goetz, F., Fatigue deformation of silver single crystals. *Metallurgical and Materials Transactions A* 7 (2), 243-248 (1976).

[137]. Yanson, A.I., Bollinger, G.R., van den Brom, H.E., Agrait, N., & van Ruitenbeek, J.M., Formation and manipulation of a metallic wire of single gold atoms. *Nature* 395 (6704), 783-785 (1998).

[138]. Waitz, T. & Karnthaler, H.P., The f.c.c. to h.c.p. martensitic phase transformation in CoNi studied by TEM and AFM methods. *Acta Materialia* 45 (2), 837-847 (1997).

[139]. Olson, G. & Cohen, M., A general mechanism of martensitic nucleation: Part I. General concepts and the FCC→HCP transformation. *Metallurgical and Materials Transactions A* 7 (11), 1897-1904 (1976).

[140]. Mahajan, S., Green, M., & Brasen, D., A model for the FCC→HCP transformation, its applications, and experimental evidence. *Metallurgical and Materials Transactions A* 8 (2), 283-293 (1977).

[141]. Huang, J.Y., Wu, Y.K., & Ye, H.Q., Phase transformation of cobalt induced by ball milling. *Applied Physics Letters* 66 (3), 308-310 (1995).

[142]. Christian, J.W., Dislocations and Properties of' Real Materials (The Institute of Metals, London, 1985), pp. 94-124.

[143]. Olson, G.B. & Cohen, M., Dislocations in Solids, edited by FRN Nabarro (North-Holland, Amsterdam, 1986), Vol. 7, pp. 295-407.

[144]. Christian, J.W., Martensite, edited by G. B. Olson and W. S. Cohen (ASM International, Ohio, USA, 1992), pp. 103-123.

[145]. Wu, X.L., Li, B., & Ma, E., Vacancy clusters in ultrafine grained Al by severe plastic deformation. *Applied Physics Letters* 91 (14), 141908-141903 (2007).

[146]. Detemple, K., Kanert, O., De Hosson, J.T.M., & Murty, K.L., In situ nuclear magnetic resonance investigation of deformation-generated vacancies in aluminum. *Physical Review B* 52 (1), 125 (1995).

[147]. Zehetbauer, M.J., Steiner, G., Schafler, E., Korznikov, A., & Korznikova, E., Deformation Induced Vacancies with Severe Plastic Deformation: Measurements and Modelling. *Materials Science Forum* 503-504, 57-64 (2006).

[148]. Huang, Y., Bai, X., & Zhang, Y., In situ mechanical properties of individual ZnO nanowires and the mass measurement of nanoparticles. *Journal of Physics: Condensed Matter* 18 (15), L179-L184 (2006).

[149]. Ajayan, P.M. & Iijima, S., Electron-beam-enhanced flow and instability in amorphous silica fibres and tips. *Philosophical Magazine Letters* 65 (1), 43 - 48 (1992).

[150]. Tong, L. *et al.*, Subwavelength-diameter silica wires for low-loss optical wave guiding. *Nature* 426 (6968), 816-819 (2003).

[151]. Brambilla, G. & Payne, D.N., The Ultimate Strength of Glass Silica Nanowires. *Nano Letters* 9 (2), 831-835 (2009).

[152]. Boer, W.d. *et al.*, Radiation hardness of diamond and silicon sensors compared. *physica status solidi (a)* 204 (9), 3004-3010 (2007).

[153]. Mota, F., Caturla, M.J., Perlado, J.M., Dominguez, E., & Kubota, A., Atomistic simulations of threshold displacement energies in SiO2. *Journal of Nuclear Materials* 329-333 (Part 2), 1190-1193 (2004).

[154]. Egerton, R.F., Li, P., & Malac, M., Radiation damage in the TEM and SEM. *Micron* 35 (6), 399-409 (2004).

[155]. Mkhoyan, K.A., Silcox, J., Ellison, A., Ast, D., & Dieckmann, R., Full Recovery of Electron Damage in Glass at Ambient Temperatures. *Physical Review Letters* 96 (20), 205506-205504 (2006).

[156]. Bourhis, E.L., *Glass: mechanics and technology*. (Wiley-VCH, 2007).

[157]. Hutchinson, J.W. & Neale, K.W., Influence of strain-rate sensitivity on necking under uniaxial tension. *Acta Metallurgica* 25 (8), 839-846 (1977).

[158]. Maehara, Y. & Langdon, T.G., Superplasticity in ceramics. *Journal of Materials Science* 25 (5), 2275-2286 (1990).

[159]. Wang, J.-G. & Raj, R., Mechanism of Superplastic Flow in a Fine-Grained Ceramic Containing Some Liquid Phase. *Journal of the American Ceramic Society* 67 (6), 399-409 (1984).

[160]. Kawamura, Y., Nakamura, T., & Inoue, A., Superplasticity in Pd40Ni40P20 metallic glass. *Scripta Materialia* 39 (3), 301-306 (1998).

[161]. Kawamura, Y., Shibata, T., Inoue, A., & Masumoto, T., Superplastic deformation of Zr65Al10Ni10Cu15 metallic glass. *Scripta Materialia* 37 (4), 431-436 (1997).

[162]. Scholze, H., *Glass: nature, structure, and properties*. (Springer, New York, 1991).

[163]. Griffith, A.A., The Phenomena of Rupture and Flow in Solids. *Philosophical Transactions of the Royal Society of London. Series A, Containing Papers of a Mathematical or Physical Character* 221, 163-198 (1921).

[164]. Bartenev, G.M., The structure and strength of glass fibers. *Journal of Non-Crystalline Solids* 1 (1), 69-90 (1968).

[165]. Ferreira Nascimento, M.L. & Zanotto, E.D., Diffusion processes in vitreous silica revisited. *Physics and Chemistry of Glasses* 48, 201-217 (2007).

[166]. Muralidharan, K., Simmons, J.H., Deymier, P.A., & Runge, K., Molecular dynamics studies of brittle fracture in vitreous silica: Review and recent progress. *Journal of Non-Crystalline Solids* 351 (18), 1532-1542 (2005).

[167]. Hobbs, L.W., *Introduction to analytical electron microscopy*. (Plenum Press, New York, 1979).

[168]. Williams, D.B. & Carter, C.B., *Transmission electron microscopy*. (Plenum Press, New York, 1996).

[169]. Griscom, D.L., E' center in glassy SiO2: Microwave saturation properties and confirmation of the primary Si29 hyperfine structure. *Physical Review B* 20 (5), 1823 (1979).

[170]. Friebele, E.J., Griscom, D.L., Stapelbroek, M., & Weeks, R.A., Fundamental Defect Centers in Glass: The Peroxy Radical in Irradiated, High-Purity, Fused Silica. *Physical Review Letters* 42 (20), 1346 (1979).

[171]. Tsai, T.E. & Griscom, D.L., Experimental evidence for excitonic mechanism of defect generation in high-purity silica. *Physical Review Letters* 67 (18), 2517 (1991).

[172]. Marsh, D.M., Plastic Flow and Fracture of Glass. *Proceedings of the Royal Society of London. Series A, Mathematical and Physical Sciences* 282 (1388), 33-43 (1964).

[173]. Luo, J., Wu, F., Huang, J., Wang, J., & Mao, S., Superelongation and atomic chain formation in nanosized metallic glass. *Physical review letters* 104 (21), 215503.

[174]. Zhang, Z.F., Zhang, H., Shen, B.L., Inoue, A., & Eckert, J., Shear fracture and fragmentation mechanisms of bulk metallic glasses. *Philosophical Magazine Letters* 86, 643-650 (2006).

[175]. Conner, R.D., Choi-Yim, H., & Johnson, W.L., Mechanical properties of Zr57Nb5Al10Cu15.4Ni12.6 metallic glass matrix particulate composites. *J. Mater. Res.* 14 (8), 3292-3297 (1999).

[176]. Conner, R.D., Dandliker, R.B., & Johnson, W.L., Mechanical properties of tungsten and steel fiber reinforced Zr41.25Ti13.75Cu12.5Ni10Be22.5 metallic glass matrix composites. *Acta Materialia* 46 (17), 6089-6102 (1998).

[177]. Das, J. *et al.*, "Work-Hardenable" Ductile Bulk Metallic Glass. *Physical Review Letters* 94 (20), 205501 (2005).

[178]. Hofmann, D.C. *et al.*, Designing metallic glass matrix composites with high toughness and tensile ductility. *Nature* 451 (7182), 1085-1089 (2008).

[179]. Xi, X.K. *et al.*, Fracture of Brittle Metallic Glasses: Brittleness or Plasticity. *Physical Review Letters* 94 (12), 125510 (2005).

[180]. Schuh, C.A., hufnagel, T.C., & Ramamurty, U., Mechanical behavior of amorphous alloys. *Acta Mater.* 55, 4067-4109 (2007).

[181]. Zhang, Z.F., Wu, F.F., He, G., & Eckert, J., Mechanical properties, damage and fracture mechanisms of bulk metallic glass materials. *J. Mater. Sci. Technol.* 23 (6), 747-767 (2007).

[182]. Pampillo, C.A., Flow and fracture in amorphous alloys. *Journal of Materials Science* 10 (7), 1194-1227 (1975).

[183]. Johnson, W.L., Bulk glass-forming metallic alloys: Science and technology. *MRS Bull.* 24 (10), 42-56 (1999).

[184]. Matthews, D.T.A., Ocelik, V., Bronsveld, P.M., & De Hosson, J.T.M., An electron microscopy appraisal of tensile fracture in metallic glasses. *Acta Materialia* 56 (8), 1762-1773 (2008).

[185]. Chen, H., He, Y., Shiflet, G.J., & Poon, S.J., Deformation-induced nanocrystal formation in shear bands of amorphous alloys. *Nature* 367 (6463), 541-543 (1994).

[186]. Wu, F.F. *et al.*, Multiplication of shear bands and ductility of metallic glass. *Applied Physics Letters* 90 (19), 191909-191903 (2007).

[187]. Zhang, Y. & Greer, A.L., Thickness of shear bands in metallic glasses. *Applied Physics Letters* 89 (7), 071907-071903 (2006).

[188]. Guo, H., Wen, J., Xiao, N.M., Zhang, Z.F., & Sui, M.L., The more shearing, the thicker shear band and heat-affected zone in bulk metallic glass. *J. Mater. Res.* 23, 2133-2138 (2008).

[189]. Stoller, R.E., Odette, G.R., & Wirth, B.D., Primary damage formation in bcc iron. *Journal of Nuclear Materials* 251, 49-60 (1997).

[190]. Yasunaga, K., Yasuda, K., Matsumura, S., & Sonoda, T., Electron energy-dependent formation of dislocation loops in CeO2. *Nuclear Instruments and Methods in Physics Research Section B: Beam Interactions with Materials and Atoms* 266 (12-13), 2877-2881 (2008).

[191]. Guo, H. *et al.*, Tensile ductility and necking of metallic glass. *Nat Mater* 6 (10), 735-739 (2007).

[192]. Mitome, M., Tanishiro, Y., & Takayanagi, K., On the structure and stability of small metal particles: high-resolution UHV electron microscope study in *Small Particles and Inorganic Clusters* (Springer Berlin Heidelberg, 1989), pp. 45-51.

[193]. Fisher, S.B., On the temperature rise in electron irradiated foils. *Radiation Effects* 5 (2), 239-243 (1970).

[194]. Inoue, A., Stabilization of metallic supercooled liquid and bulk amorphous alloys. *Acta Mater.* 48 (1), 279-306 (2000).

[195]. Schuh, C.A., Lund, A.C., & Nieh, T.G., New regime of homogeneous flow in the deformation map of metallic glasses: elevated temperature nanoindentation experiments and mechanistic modeling. *Acta Materialia* 52 (20), 5879-5891 (2004).

[196]. Li, Q.-K. & Li, M., Effects of surface imperfections on deformation and failure of amorphous metals. *Applied Physics Letters* 87 (3), 031910-031913 (2005).

[197]. Li, Q.-K. & Li, M., Molecular dynamics simulation of intrinsic and extrinsic mechanical properties of amorphous metals. *Intermetallics* 14 (8-9), 1005-1010 (2006).

[198]. Li, Q.K. & Li, M., Free volume evolution in metallic glasses subjected to mechanical deformation. *Mater. Trans.* 48 (7), 1816-1821 (2007).

[199]. Zhang, Z.F., Eckert, J., & Schultz, L., Difference in compressive and tensile fracture mechanisms of Zr59Cu20Al10Ni8Ti3 bulk metallic glass. *Acta Materialia* 51 (4), 1167-1179 (2003).

[200]. Lewandowski, J.J. & Greer, A.L., Temperature rise at shear bands in metallic glasses. *Nat Mater* 5 (1), 15-18 (2006).

[201]. Yang, B. *et al.*, In-situ thermographic observation of mechanical damage in bulk-metallic glasses during fatigue and tensile experiments. *Intermetallics* 12 (10-11), 1265-1274 (2004).

[202]. Shan, Z.W. *et al.*, Plastic flow and failure resistance of metallic glass: Insight from in situ compression of nanopillars. *Physical Review B (Condensed Matter and Materials Physics)* 77 (15), 155419-155416 (2008).

[203]. Jang, D. & Greer, J.R., Transition from a strong-yet-brittle to a stronger-and-ductile state by size reduction of metallic glasses. *Nat Mater* 9 (3), 215-219 (2010).

[204]. Volkert, C.A., Donohue, A., & Spaepen, F., Effect of sample size on deformation in amorphous metals. *Journal of Applied Physics* 103 (8), 083539-083536 (2008).

[205]. Johnson, W.L. & Samwer, K., A Universal Criterion for Plastic Yielding of Metallic Glasses with a (T/Tg)2/3 Temperature Dependence. *Physical Review Letters* 95 (19), 195501 (2005).

[206]. He, Y., Poon, S.J., & Shiflet, G.J., Synthesis and Properties of Metallic Glasses that Contain Aluminum. *Science* 241 (4873), 1640-1642 (1988).

[207]. Dunlap, R.A. *et al.*, Physical properties of amorphous Al 90 Fe 5 Ce 5. *Journal of Physics: Condensed Matter* 2 (19), 4315 (1990).

[208]. Hays, C.C., Kim, C.P., & Johnson, W.L., Microstructure Controlled Shear Band Pattern Formation and Enhanced Plasticity of Bulk Metallic Glasses Containing in situ Formed Ductile Phase Dendrite Dispersions. *Physical Review Letters* 84 (13), 2901 (2000).

[209]. Moore, N.W., Luo, J., Huang, J.Y., Mao, S.X., & Houston, J.E., Superplastic Nanowires Pulled from the Surface of Common Salt. *Nano Letters* 9 (6), 2295-2299 (2009).

[210]. Wakai, F. *et al.*, A superplastic covalent crystal composite. *Nature* 344 (6265), 421-423 (1990).

[211]. Untiedt, C., Rubio, G., Vieira, S., & Agra 飓, N., Fabrication and characterization of metallic nanowires. *Physical Review B* 56 (4), 2154 (1997).

[212]. Kuipers, L. & Frenken, J.W.M., Jump to contact, neck formation, and surface melting in the scanning tunneling microscope. *Physical Review Letters* 70 (25), 3907 (1993).

[213]. Yanson, A.I., Yanson, I.K., & van Ruitenbeek, J.M., Observation of shell structure in sodium nanowires. *Nature* 400 (6740), 144-146 (1999).

[214]. Wu, Y., Xiang, J., Yang, C., Lu, W., & Lieber, C.M., Erratum: Single-crystal metallic nanowires and metal/semiconductor nanowire heterostructures. *Nature* 430 (7000), 704-704 (2004).

[215]. Wu, Y., Xiang, J., Yang, C., Lu, W., & Lieber, C.M., Single-crystal metallic nanowires and metal/semiconductor nanowire heterostructures. *Nature* 430 (6995), 61-65 (2004).

[216]. Barnes, R.B., The Plasticity of Rocksalt and Its Dependence upon Water. *Physical Review* 44 (11), 898 (1933).

[217]. Carter, N.L., Horseman, S.T., Russell, J.E., & Handin, J., Rheology of rocksalt. *Journal of Structural Geology* 15 (9-10), 1257-1271 (1993).

[218]. Weis, D.D. & Ewing, G.E., Water content and morphology of sodium chloride aerosol particles. *J. Geophys. Res.* 104 (D17), 21275-21285 (1999).

[219]. Finlayson-Pitts, B.J., The Tropospheric Chemistry of Sea Salt: A Molecular-Level View of the Chemistry of NaCl and NaBr. *Chemical Reviews* 103 (12), 4801-4822 (2003).

[220]. Shindo, H., Ohashi, M., Baba, K., & Seo, A., AFM observation of monatomic step movements on NaCl(001) with the help of adsorbed water. *Surface Science* 357-358, 111-114 (1996).

[221]. Sheehan, P.E., The wear kinetics of NaCl under dry nitrogen and at low humidities. *Chemical Physics Letters* 410 (1-3), 151-155 (2005).

[222]. Westwood, A.R.C., SURFACE-SENSITIVE MECHANICAL PROPERTIES. *Industrial & Engineering Chemistry* 56 (9), 14-25 (2002).

[223]. Gorum, A.E., Parker, E.R., & Pask, J.A., Effect of Surface Conditions on Room-Temperature Ductility of Ionic Crystals. *Journal of the American Ceramic Society* 41 (5), 161-164 (1958).

[224]. Suresh, S. & Li, J., Materials science: Deformation of the ultra-strong. *Nature* 456 (7223), 716-717 (2008).

[225]. Roberts, M.W. & Thomas, J.M., Surface and Defect Properties of Solids (The Chemical Society, London, 1975), Vol. 4.

[226]. Allen, H.C., Mecartney, M.L., & Hemminger, J.C., Minimizing transmission electron microscopy beam damage during the study of surface reactions on sodium chloride. *Microscopy and Microanalysis* 4 (1), 23-33 (1998).

[227]. Ahn, C.C. & Krivanek, O.L., *EELS Atlas*. (Gatan, Inc., Warrendale, PA, 1983).

[228]. Muray, A., Scheinfein, M., Isaacson, M., & Adesida, I., Radiolysis and resolution limits of inorganic halide resists. *Journal of Vacuum Science & Technology B: Microelectronics and Nanometer Structures* 3 (1), 367-372 (1985).

[229]. Herrmann, F., Pinard, P., & Farge, Y., About the displacement of the lithium ion in lithium fluoride by accelerated electrons. *Journal of Physics C: Solid State Physics* (11), L199 (1974).

[230]. Karch, J., Birringer, R., & Gleiter, H., Ceramics ductile at low temperature. *Nature* 330 (6148), 556-558 (1987).

[231]. Joffé, A., Kirpitschewa, M.W., & Lewitzky, M.A., Deformation und Festigkeit der Kristalle. *Zeitschrift für Physik A Hadrons and Nuclei* 22 (1), 286-302 (1924).

[232]. Gilbert, B., Huang, F., Zhang, H., Waychunas, G.A., & Banfield, J.F., Nanoparticles: Strained and Stiff. *Science* 305 (5684), 651-654 (2004).

[233]. Vashishta, P., Kalia, R.K., Rino, J.P., & Ebbsj, I., Interaction potential for SiO2: A molecular-dynamics study of structural correlations. *Physical Review B* 41 (17), 12197 (1990).

[234]. Vashishta, P., Kalia, R.K., Nakano, A., Li, W., & Ebbsjo, I., Molecular dynamics methods and large-scale simulations of amorphous materials in *Proceeding of the NATO advanced study institute on amorphous insulators and semiconductors*, edited by M. F. Thorpe & M. I. Mitkova (Kluwer Academic Publishers, Sozopol, Bulgaria, 1996), pp. 151-214.

[235]. van Beest, B.W.H., Kramer, G.J., & van Santen, R.A., Force fields for silicas and aluminophosphates based on ab initio calculations. *Physical Review Letters* 64 (16), 1955 (1990).

[236]. Nakano, A., Kalia, R.K., & Vashishta, P., First sharp diffraction peak and intermediate-range order in amorphous silica: finite-size effects in molecular dynamics simulations. *Journal of Non-Crystalline Solids* 171 (2), 157-163 (1994).

[237]. Shackelford, J.F. & Alexander, W., *CRC Materials science and engineering handbook*. (CRC Press, New York, 2001).

[238]. Smith, W. & Forester, T.R., DL_POLY_2.0: A general-purpose parallel molecular dynamics simulation package. *Journal of Molecular Graphics* 14 (3), 136-141 (1996).

[239]. Chen, Y.-C. *et al.*, Interaction of Voids and Nanoductility in Silica Glass. *Physical Review Letters* 99 (15), 155506-155504 (2007).

[240]. Celarie, F. *et al.*, Glass Breaks like Metal, but at the Nanometer Scale. *Physical Review Letters* 90 (7), 075504 (2003).

[241]. Bonamy, D. *et al.*, Nanoscale damage during fracture in silica glass. *International Journal of Fracture* 140 (1), 3-14 (2006).

[242]. Guin, J.-P. & Wiederhorn, S.M., Fracture of Silicate Glasses: Ductile or Brittle? *Physical Review Letters* 92 (21), 215502 (2004).